

Photoemission Spectroscopy of Low-Dimensional Charge-Density-Wave and Superconducting Materials

THÈSE N° 4791 (2010)

PRÉSENTÉE LE 23 AOÛT 2010

À LA FACULTÉ SCIENCES DE BASE

LABORATOIRE DE SPECTROSCOPIE ÉLECTRONIQUE

PROGRAMME DOCTORAL EN PHYSIQUE

ÉCOLE POLYTECHNIQUE FÉDÉRALE DE LAUSANNE

POUR L'OBTENTION DU GRADE DE DOCTEUR ÈS SCIENCES

PAR

Peng XU

acceptée sur proposition du jury:

Prof. N. Baluc, présidente du jury

Prof. M. Grioni, directeur de thèse

Prof. L. Forro, rapporteur

Prof. D. Malterre, rapporteur

Dr M. Shi, rapporteur



ÉCOLE POLYTECHNIQUE
FÉDÉRALE DE LAUSANNE

Suisse
2010

Acknowledgement

I am indebted to my thesis supervisor, Professor Marco Grioni, who gave me a precious opportunity to the beautiful city - Laussane - to join his research group. He introduced me into the wonderful and full of challenge physics world and taught me many scientific skills with much patient. I am very lucky and with great pleasure to work with this expert of strong correlated electron systems. To complete his high-standard task is really a challenge for me, inducing me from a greener in physics to a higher level. Thank you Marco!

Here I would thank to the members of the jury, Prof. D. Malterre, Dr. M. Shi and Prof. L. Forró, and to the president, Prof. N. Baluc, for accepting to go through all the following pages of this thesis and for precious suggestions in view of the future work.

I am very grateful to Dr. Ming Shi, who taught me a lot in the synchrotron business. I am appreciated very much his knowledge and support for the tough work in Swiss light source.

I would like to give my thanks to Prof. László Forró, Dr. Balazs Sipos and Mr. Stevan Arsenijevic for all the resistivity measurements. I sincerely appreciate their competence and their availability.

Great thanks to Prof. Henrik M. Rønnow and Mr. Julian Piatek , who provide me the important magnetic susceptibility measurements and precious discussion with us.

Special thanks is given to Mr. Helmuth Berger, who always can provide me high quality and interesting single crystals that studied in this thesis.

I am pleased to have the chance to work with Dr. Azzedine Bendoinan, who taught me a lot of impressive experimental skills.

I would like to express my thanks to the help and collaborations with all my colleagues in EPFL. Luca Moreschini, who taught me many experimental skills and how to write IGOR procedures with his humor. I dream one day I could see you play tennis in the US open. Joy, who I gave a lot of help on the sample orientation and offers much delicious food. Stéphane Pons, who can always answer my questions on physics. Miguel A. Valbuena, we worked a lot together and we all like to talk football. And then Emmanouil Frantzeskakis, Xiaoqiang Wang, Marco Guarise, Alberto Crepaldi, Roberto Mastrangelo, Mihaela Falub and Claudia Cancellieri. And all the workshop team in IPMC, and the secretaries of the institute and of the doctoral school are deserved to be acknowledged.

I would also like to thank the support from all the staff in SIS and ADRESS beamlines in Swiss light source.

I am grateful to the personnel of ANTARES beamline in the Synchrotron Soleil, especially Madame Maria-Carmen Asensio and Dr. José Avila, for their technical support and friendly attitude.

I acknowledge all my Chinese friends, Li Jin, Hua Zhang, Yan Yan, Hui Yang, Fengda Sun, Zhanbing He, Hongyan Bi, Liang Qiao, Shenqi Xie, Zhaolu Diao, Yu Lu, Cheng Yu, Peiyu Ge, Ji Cao and so on, in EPFL for their patience and friendly encouragement, for not letting me feel lonely in a foreign country.

The support and love of my family have been the endless fuel for all my life in the PhD study. Great thanks to my parents and parents in law. Especially, I express a kiss for my wife, Meng Shen, with whom I shared all the happiness and tears during the four years life in Lausanne. I also wish her the best with her PhD programme.

Abstract

The discovery in 1986 of the high-Tc superconducting cuprates has ushered in a new era of research in condensed matter physics. There is still a great interest for these materials, which stems not only from the lack of a clear theoretical picture, but also from the perspective of practical applications which could have an enormous impact on everyday's life. The complexity of the cuprates has stimulated a critical reassessment of many theoretical concepts and the development of new ideas, and fueled an unprecedented experimental activity to characterize their electronic structure. Besides the obvious occurrence of superconductivity, the two-dimensional character and the proximity to other ordered states, appear as prominent characteristics of these materials. The interplay of these properties is the subject of intense theoretical activity, since it is believed that it could play an important role in the emergence of the unconventional superconducting state. At the same time, it has been realized that similar situations may also arise in other classes of materials, where they lead to complex phase diagrams and to the emergence of new, unusual properties. These materials therefore offer interesting opportunities for related research.

This thesis presents an investigation of the electronic structure of selected quasi-2D materials, and of their electronic instabilities – charge-density-wave (CDW), Mott metal-insulator transition, superconductivity – by means of angle resolved photoemission spectroscopy (ARPES). ARPES is a very powerful probe of solids which, thanks to its unique energy and momentum selectivity, provides a clear and direct view of the electronic states and of their interactions. Most of this work is concentrated on the low-energy excitations near the Fermi surface, the *quasiparticles*. These states play a crucial role in the thermodynamic, magnetic and transport of solids. Together with the shape of the Fermi surface, they determine the possible occurrence of electronic instabilities like charge- or spin-density waves, or again superconductivity (SC). A *leitmotiv* of this work is the study of how the nature of the quasiparticles, reflected in the ARPES spectral function, and the Fermi surface are influenced by an underlying instability, or by the competition between several instabilities. I have performed high-resolution ARPES experiments at the LSE-ICMP, and at two synchrotron radiation laboratories: the Swiss Light Source (PSI-Villigen) and SOLEIL (Paris).

A large part of this work is concerned with the electronic properties of compounds which

belong to the class of transition metal dichalcogenides (TMDs). TMDs are layered materials with rather strongly two-dimensional (2D) electronic properties. They often exhibit charge-density-wave (CDW) instabilities, and in selected cases superconductivity, but also peculiar metal-insulator (Mott) transitions. Among the TMDs, the $1T$ and $2H$ polytypes of TaS_2 are representative of CDW materials which do not naturally exhibit SC, where SC can nonetheless be induced e.g. by applying external pressure. For $1T\text{-TaS}_2$ I show that a small amount of disorder entirely removes a Mott transition to a low-temperature insulating phase, opening the way to a non-homogeneous SC phase below $\sim 2K$. ARPES here shows that SC emerges from a ‘bad-metal’ normal state. I have performed a detailed study of Sn-doped $2H\text{-TaS}_2$, where doping suppresses the CDW, but seems to enhance SC. I namely examine the partial gapping of the Fermi surface, as well as the spectral signatures of the interaction with the lattice. The spectral consequences of disorder induced by doping are also captured by ARPES in the degenerate semiconductor $1T\text{-Nb}_x\text{Ti}_{1-x}\text{S}_2$.

The second part of the thesis is devoted to two members of the high- T_c cuprate BSCCO family. The two-layer Bi2212 member of this family has been the object of countless spectroscopic studies. I present here results for two considerably less-studied members of this family: the three-layer Bi2223 , which has the highest T_c , and the single-layer Bi2201 . In Bi2223 I found circumstantial evidence for the elusive threefold splitting of the Fermi surface expected from interlayer coupling. The momentum- and temperature dependence of the d -wave SC gap are illustrated by the ARPES data. The data also contain interesting information on the normal state low-energy kink (~ 70 meV) – the fingerprint of the coupling of the electrons to a bosonic mode – and the high-energy anomaly in this compound. The originality of the results for Bi2201 lies in the nature of the samples, thin films prepared *in situ* by pulsed-laser-deposition (PLD), in the framework of a collaboration with the CREAM-ICMP laboratory. The ARPES results clearly demonstrated the feasibility of such studies, but also evidenced some difficulties related to the twinned nature of the films, which will have to be addressed in future studies. The ARPES data on the cuprates are complemented by the results of high-resolution resonant inelastic x-ray scattering (RIXS) experiments performed at the new SAXES end-station of the SLS. At variance with ARPES, which probes electron-removal states, RIXS probes neutral excitations, and therefore provides a complementary view of the electronic structure, similar to optics, but not limited to zero-momentum transitions. The resolution of RIXS is at present insufficient to address the low-energy gap scale, but it opens an entirely new window on the *magnetic* excitations, namely in the insulating parent compounds.

Keywords:

electronic structure, angle-resolved photoemission (ARPES), low-dimensional solids, charge-density-wave, Mott-insulator, high- T_c superconductivity

Résumé

La découverte en 1986 des supraconducteurs à haute température critique a conduit à une nouvelle ère de recherche en physique de la matière condensée. Il y a aujourd'hui encore un intérêt important pour ces matériaux non seulement à cause du manque de compréhension théoriques des mécanismes mis en jeu mais aussi parce que les applications pratiques naissantes sont majeures et pourraient avoir un énorme impact sur la vie de tous les jours. La complexité des cuprates a provoqué un réexamen critique de nombreux concepts théoriques, stimulé le développement de nouvelles idées et alimenté une activité expérimentale sans précédent pour caractériser leurs propriétés électroniques. En plus de leurs propriétés supraconductrices, leur caractère bidimensionnel et la proximité de différents états ordonnés semblent être une caractéristique remarquable de ces matériaux. Les interactions entre ces différentes propriétés sont le sujet d'intenses activités théoriques puisqu'elles pourraient avoir un rôle sur l'apparition de la supraconductivité non-conventionnelle. Par ailleurs, la communauté scientifique a remarqué qu'une situation similaire pourrait exister dans d'autres classes de matériaux ce qui les doterait de diagrammes de phases complexes associés à des propriétés physiques inhabituelles ou nouvelles. Ces matériaux offrent donc une opportunité intéressante pour effectuer des recherches complémentaires ou alternatives à celles sur les cuprates.

Cette thèse présente l'étude de la structure électronique de matériaux quasi-2D choisis pour leur instabilités électroniques (onde de densité de charge (CDW), transition métal-isolant de Mott, supraconductivité) par spectroscopie de photoémission résolue en angle (ARPES). Grâce à sa sélectivité en vecteur d'onde et en énergie, l'ARPES est une sonde puissante qui permet d'obtenir une vue directe et précise des états électroniques et de leurs interactions. La plus grande partie de ce travail est focalisée sur les excitations de basse énergie proches de la surface de Fermi : les quasiparticules. Ces états jouent un rôle crucial dans les propriétés thermodynamiques, magnétiques et de transport. Avec la forme de la surface de Fermi, elles déterminent la possibilité d'instabilités électroniques comme les ondes de densité de charge ou de spin ou encore la supraconductivité. Dans ce travail nous cherchons constamment à faire le lien entre la nature des quasiparticules, reflétée dans la fonction spectral mesurée par ARPES et la topologie de la surface de Fermi, et la compétition entre les différentes instabilités. Pendant ma thèse, j'ai effectué des mesures d'ARPES au LSE-ICMP à l'EPFL et à deux différents

synchrotrons Swiss Light Source (SLS, PSI-Villigen) et SOLEIL (Orsay).

Une grande partie de ce travail concerne les propriétés électroniques de composés de la famille des dichalcogénures de métaux de transition (TMDs). Les TMDs sont des matériaux lamellaires présentant des propriétés électroniques fortement bidimensionnelles (2D). Ils présentent souvent des instabilités conduisant à des ondes de densité de charge et dans certains cas à la supraconductivité ou à une transition métal isolant de Mott inhabituelle. Parmi les TMDs, les polytypes 1T et 2H de TaS₂ présentent des phases CDW mais pas de supraconductivité de façon naturelle. La supraconductivité peut cependant être induite dans ces matériaux par exemple en appliquant une pression extérieure. Pour 1T-TaS₂, je montre qu'un petit peu de désordre détruit entièrement la transition de Mott et induit une phase supraconductrice inhomogène à basse température ($T_C \approx 2K$). Les mesures de photoémission montrent ici que la supraconductivité émerge d'un état normal de type " mauvais métal ". J'ai effectué une étude détaillée de l'échantillon 2H-TaS₂ dopé par des atomes de Sn où le dopage supprime la phase CDW mais semble amplifier la supraconductivité. J'analyse pour ce matériau l'ouverture directionnelle de la bande d'énergie interdite (*gap*) dans la surface de Fermi ainsi que la signature spectrale de l'interaction avec le réseau.

La seconde partie de la thèse est consacrée à deux supraconducteurs à haute température critique membres de la famille des BSCCO. Le matériau " biplan " (deux plans CuO par maille) Bi2212 a donné lieu à d'innombrables études spectroscopiques. Je présente ici les résultats que j'ai obtenu sur deux composés considérablement peu étudiés, le matériau triplan Bi2223 qui possède la plus haute T_C et le matériau monoplan Bi2201. Dans Bi2223, je mets en évidence l'effet du couplage entre les plans de cuivre-oxygène en montrant que la surface de Fermi est composée de trois jeux séparés de bandes. La dépendance en moment et en température du *gap* supraconducteur de symétrie d est illustré par des données d'ARPES. Les données présentent aussi des informations intéressantes obtenues dans la phase normale sur une rupture (*kink*) dans la dispersion électronique (à environ 70 meV) et sur une anomalie à plus haute énergie. La rupture à basse énergie est supposé être la signature du couplage des électrons avec un mode bosonique. L'originalité des résultats obtenus pour Bi2201 viennent de la nature de l'échantillon qui a été élaboré *in situ* en déposant les matériaux par ablation laser (PLD) dans le cadre d'une collaboration avec le laboratoire CREAM-ICMP de l'EPFL. La photoémission démontre clairement la faisabilité d'une telle étude mais met en évidence les difficultés liées à la nature fragmentée du film. Les données d'ARPES sont complétées par des mesures diffusion inélastique de rayons X à haute résolution (RIXS) réalisées à la nouvelle plateforme SAXES de SLS. Alors que la photoémission sonde les états finals lors du retrait d'un électron, le RIXS sonde les excitations neutres et donc offre une vue complémentaire de la structure électronique similaire à la spectroscopie optique mais sensible au moment. La résolution actuelle du RIXS n'est pas suffisante pour étudier les phénomènes de faible énergie

comme ceux liés au *gap* supraconducteur mais le RIX ouvre une nouvelle fenêtre sur les excitations magnétiques, c'est-à-dire pour les composés parents de nature isolante.

Mots clés:

structure électronique, spectroscopie de photoémission résolue en angle, systèmes de basse dimensionnalité, onde de densité de charge, isolant de Mott, superconductivité à haute température critique

Contents

Acknowledgement	i
Abstract	iii
Résumé	vii
1 Introduction	1
2 Electronic properties of quasi 2D conductors	3
2.1 Peierls instability and charge density wave	3
2.2 Metal-insulator Mott transition	8
2.3 Superconductivity	12
2.3.1 Phenomenological theories of superconductivity	12
2.3.2 BCS theory	13
2.3.3 High- T_c superconductors	15
3 Description of the experiment	21
3.1 Experimental technique of ARPES	22
3.1.1 The electron analyzer	22
3.1.2 EPFL and SLS set-ups	24
3.1.3 Sample preparation	25
3.2 Basic theory of photoemission	26
3.2.1 The photoelectric effect	26
3.2.2 Basic principle of ARPES	29
3.2.3 Sudden approximation	32
3.2.4 One-particle spectral function	33
3.2.5 Extracting the real and imaginary parts of the self-energy	34
4 Transition metal dichalcogenides	37
4.1 Introduction to transition metal dichalcogenides	37
4.1.1 Crystallographic and electronic structure	37

4.2	1T-TaS ₂	40
4.2.1	Superconductivity coexists and competes with CDW in 1T-TMDs	44
4.2.2	Occurrence of superconductivity when the metal-insulator transition is inhibited in 1T-TaS ₂ (Phys. Rev. B 81 172503 (2010))	45
4.3	1T-TiS ₂	53
4.3.1	The semimetal to semiconductor transition in 1T-TiS ₂ induced by Nb doping studied by angle resolved photoemission spectroscopy (to be submitted to Phys. Rev. B)	53
4.4	2H-TaS ₂	63
4.4.1	The coexistence of superconductivity and charge-density-wave in 2H-Sn _x TaS ₂ (to be submitted to Phys. Rev. B)	65
5	Electronic structure and properties of Bi-family (BSCCO) cuprates	73
5.1	Crystal structure of the layered Bi-based cuprates	74
5.1.1	Basic BSCCO structure	74
5.1.2	The phase diagram of Bi family cuprates	75
5.2	Structure and physical properties of Bi2223	76
5.2.1	AC magnetic susceptibility and scanning tunneling spectroscopy (STS) of Bi2223	76
5.3	Electronic properties of Bi2223	76
5.3.1	Electronic band structure of Bi2223	76
5.4	The superconducting energy gap	83
5.4.1	Two kinds of wave symmetries	83
5.4.2	Superconducting gap from ARPES data in Bi2223	84
5.4.3	Band renormalization effects from ARPES data in Bi2223	89
5.5	ARPES on thin film Bi ₂ Sr _{2-x} La _x CuO ₆	96
6	RIXS experiment on insulating and superconducting cuprates	101
6.1	General information on RIXS	101
6.2	RIXS on Sr ₂ CuO ₂ Cl ₂	105
6.3	RIXS on optimally doped Bi2212 and Bi2223	109
7	Conclusions and outlook	119
	Bibliography	123
	Curriculum Vitae	141

Chapter 1

Introduction

In the past several decades, low-dimensional systems have attracted considerable interest both from the experimental and from the theoretical point of view. The interest arises not only from the richness of the physical phenomena encountered in such systems, but also from many potential future applications. The world we live in is of course three dimensional (3D), but materials characterized by a large anisotropy of their physical properties may effectively behave as low-dimensional electronic systems. Therefore, low dimensional systems are not just idealized toy-systems for the theorist. In the past few decades many *quasi* one- and two-dimensional materials have been discovered. For example, the fullerene molecule (C_{60}) is essentially a zero dimensional system, carbon nanotubes are one-dimensional, and graphite as well as the transition metal dichalcogenides (TMDs) considered in the present work, are quasi-two-dimensional systems. In my thesis I mainly focus on the electronic properties of low dimensional TMDs and on selected high- T_c cuprate superconductors (HTSCs). These materials have been extensively studied in the past, but several aspects of their electronic properties are still only partially understood.

The reduction from 3D to low dimension (2D or 1D) has several important consequences. Electronic correlations, the electron-phonon interaction, and fluctuations have a larger effect in reduced dimensions. On the one hand, the electronic states near the Fermi level, which form the Fermi surface (FS), are subject to characteristic instabilities. In 1955 Peierls [1] predicted an electronic instability for the 1D electron gas, which results from the peculiar FS topology as we will discuss later in **Chapter 2** and **4**. A periodic modulation of the electron density – a charge-density-wave (CDW) – accompanied by a lattice distortion, then develops. Later, superconductivity (SC) and CDW were found to coexist in specific systems, and in 1954 Frohlich [2] even proposed a model for superconductivity based on the sliding motion of the CDWs. The properties of electrons in low dimension system, even in the normal state, are strongly affected by these instabilities. Low-dimensional systems are also intrinsically more sensitive to fluctuations. In the extreme case of 1D these fluctuations destroy long range order

at any finite temperature, and only short range order can develop. The 2D systems considered here are less ‘pathological’, and ordered phases are indeed experimentally observed, albeit with reduced ordering temperatures.

The HTSCs discovered by G. Bednorz and K. A. Muller in 1986 represent an even more complex and intriguing class of low dimensional materials. For more than two decades scientists have struggled to build an accepted model for the exotic properties of these materials. The normal state of the cuprates exhibits unusual features, which cannot be interpreted in the framework of Fermi liquid (FL) theory, the generic scenario for metals. As to the SC phase, the unusually high T_c , and the d -wave gap symmetry clearly distinguish them from more common SCs. Perhaps not surprisingly, there is no consensus at present on the mechanism of high- T_c SC. It has been proposed that electron spectroscopies, and especially angle-resolved photoelectron spectroscopy (ARPES) with high energy and momentum resolution, can play a crucial role in unveiling the complex electronic properties, and possibly the pairing mechanism, of HTSC. This is a constant stimulus for numerous, increasingly sophisticated ARPES studies by many leading groups worldwide.

The original motivation of my work was to obtain new high-quality spectroscopic data on specific TMDs and HTSCs which could reveal new phenomena, and help address the outstanding questions on the electronic properties of these material. The thesis is organized as follows. In **Chapter 2** I will give the background for the present study on CDWs and high- T_c systems. Experimental and theoretical aspects of ARPES are briefly reviewed in **Chapter 3**. **Chapter 4** presents original results on selected 1T and 2H polytype CDW TMDs. The first part of the chapter illustrates the occurrence of disorder-induced superconductivity in the presence of a strong CDW in 1T-TaS₂. Then the evolution from semi-metal to semiconductor in Nb-doped 1T-TiS₂ is discussed. The last part of the chapter deals with the coexistence of CDW and SC in Sn-doped 2H-TaS₂. **Chapter 5** presents synchrotron radiation ARPES data on the three-layer Bi-cuprate Bi2223. The momentum and temperature dependence of the SC gap, the evidence for a trilayer splitting, and the observation of several band renormalization effects (kinks) are discussed. The last part of the chapter illustrates preliminary ARPES results of in-situ grown Bi2201 thin films. Finally, **Chapter 6** introduces a different spectroscopic technique – resonant inelastic x-ray spectroscopy (RIXS) – and presents very recent data on the antiferromagnetic insulating parent compound Sr₂CuO₂Cl₂ and on two SC cuprates.

Chapter 2

Electronic properties of quasi 2D conductors

In this chapter I will address some relevant aspects, in a very schematic way, for the low dimensional systems which are the theoretical background for the understanding of the following chapters 4 and 5. Although all these theories have been mentioned a lot in many of the solid state physics books, the discussion is still hot on many topics. Indeed the phase diagram of low dimensional systems is complex mainly due to the subtle balance of phenomena triggered by doping, pressure, carrier density, structure modifications, etc.. In the following I will attempt to give a brief introduction to some of the electronic instabilities encountered in these systems: Charge density waves (CDW), Mott transitions and superconductivity (SC).

2.1 Peierls instability and charge density wave

The Peierls instability was proposed by Peierls and discussed in detail in his book of Quantum theory of solids [1], where he considered a system of free electrons in one dimension and concluded that there cannot be any metallic state at $T=0$ K. A similar argument was also proposed by Frölich [2].

The simplest picture of a 1D system can easily illustrate the Peierls instability (I will neglect here the effect of order parameter fluctuations which are very strong and actually completely strictly suppress the translation symmetry in 1D system). The normal state consists of a half filled band with a Fermi wavevector (k_F) at half of the Brillouin zone (BZ) (Figure 2.1). The ions are equally spaced and the electronic density is uniform if the electrons are not coupled to phonons (Fig. 2.2 up part). If we take into account the electron phonon coupling, when the temperature drops below T_{CDW} , a periodic lattice distortion (PLD) takes place which induces a periodic modulation of the electron density. Figure 2.2 (low part) schematically shows the CDW resulting from a Peierls transition. The single particle band evolution due to the CDW

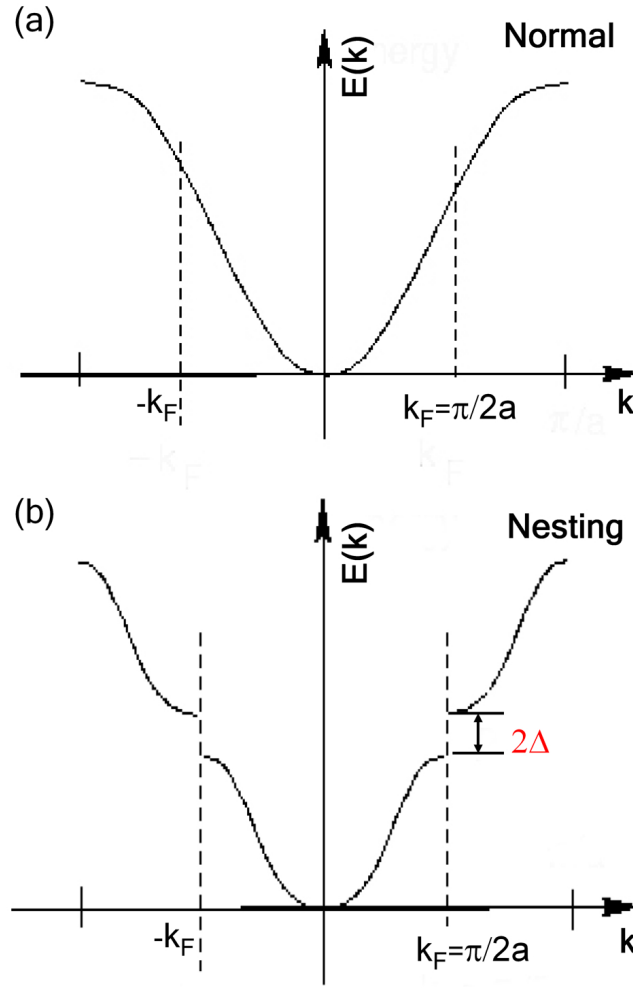


Figure 2.1: Energy vs wavevector for the 1D case with single band (From [3]).

occurrence is presented in Figure 2.1 (b). The CDW wavevector \vec{q} ($q = 2k_F$) connects the Fermi level crossing at $+k_F$ and $-k_F$. This mechanism, namely that distortion vector \vec{q} is spanned across the Fermi surface (FS), is referred to as "nesting". For example, for a half-filled band, such nesting implies a reduction of the BZ to half its size, which in real space corresponds to a period doubling (Fig. 2.2 low part). The formation of CDW usually causes a metal-insulator transition because the periodicity of the static 1D deformation defines new Bragg planes at $k_F = \pm \frac{\pi}{2a}$ and eventually, a gap Δ opens at the FS.

The CDW mechanism results in a reduction of the total energy of the system and involves the competition between two energies. One energy corresponds to the cost of elastic energy for making the PLD. The other one is given by the gap opening and is associated to the lowering of the energy of the occupied states right at k_F . The density of states of a gapped 1D system diverges as $D(E) \propto E^{-1/2}$, thus an instability of the FS is strongly favored even for small

excitations. Though the electronic energy of the system decreases, the lattice distortion is limited due to the cost in elastic energy.

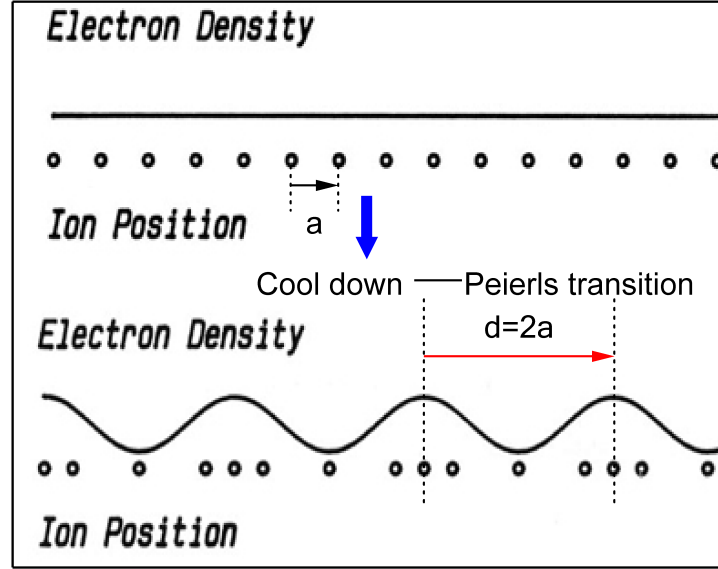


Figure 2.2: The electronic charge density is modulated when the system enters into a CDW state. (Reproduced From [4])

The CDW instability dominates whenever correlations are driven by the electron-phonon (*el-ph*) coupling, which could be further understood as following. On the one hand, in order to stabilize a CDW the *el-ph* coupling must be considered. And the CDW is also linked to a PLD which is truly a related transition with CDW. On the other hand, the occurrence of a PLD and the effect of *el-ph* coupling can be observed in the phonon dispersion. The particular case is the observation of Kohn anomaly, where the phonon dispersion is modified with a soft phonon mode and exhibits a dip at $2k_F$ [5] (shown in Fig. 2.3).

The heart of the CDW phenomenon is the Lindhard electric susceptibility $\chi(q)$ which provides the response function of the electron system behaving under the influence of an external potential $V(q)$. Therefore, we can write

$$\delta\rho(q) = \chi(q)V(q), \quad (2.1)$$

where $\delta\rho(q)$ is the electron density modulation. And the susceptibility $\chi(q)$ can be written as

$$\chi(q) = \sum_k \frac{f_k - f_{k+q}}{\varepsilon_{k+q} - \varepsilon_k} \quad (2.2)$$

where f_k and ε_k are the occupation function at wavevector k and the band energy, respectively. It is quite obvious from the formula 2.2 that only the states near the Fermi level significantly

contribute to the sum, since for low energy excitations, electrons can only scatter near the Fermi level from the occupied to unoccupied states. The formula 2.2 can be explicitly deduced in the 1D case if we approximate the free-electron parable by a linear dispersion near k_F .

$$\chi(q)_{1D} = e^2 n(\varepsilon_F) \ln \left| \frac{q + 2k_F}{q - 2k_F} \right| \quad (2.3)$$

Here $n(\varepsilon_F)$ is the density of states at the Fermi level, and e is the electron charge. Evidently, this function has a logarithmic singularity at $q = 2k_F$, which is the origin of the Peierls instability [1]. As a consequence, a 1D electron gas will be unstable against the formation of a CDW state with wavevector $q_{CDW} = 2k_F$. The dramatic susceptibility dependence on dimensionality is illustrated in Fig 2.4, where clearly demonstrates a singularity in 1D at $q = 2k_F$. In contrast, with increasing dimensionality the peak in the susceptibility at $q = 2k_F$ is weaker, leading to the removal of the singularity at $q = 2k_F$. In 2D or 3D the susceptibility can still have a maximum at $q = 2k_F$ if the FS contains two parallel sections. In general, nesting and the associated instability is favorable to occur in low dimensions.

The key feature of a CDW system is the opening a gap at the Fermi level. The CDW gap magnitude is determined by the *el-ph* coupling strength. In the framework of mean field, the low temperature ground state is destabilized and undergoes a transition to a CDW state at a finite temperature T_{MF} . By analogy with the BCS theory of superconductivity, one finds a gap $2\Delta(T = 0) = 3.53k_B T_{MF}$.

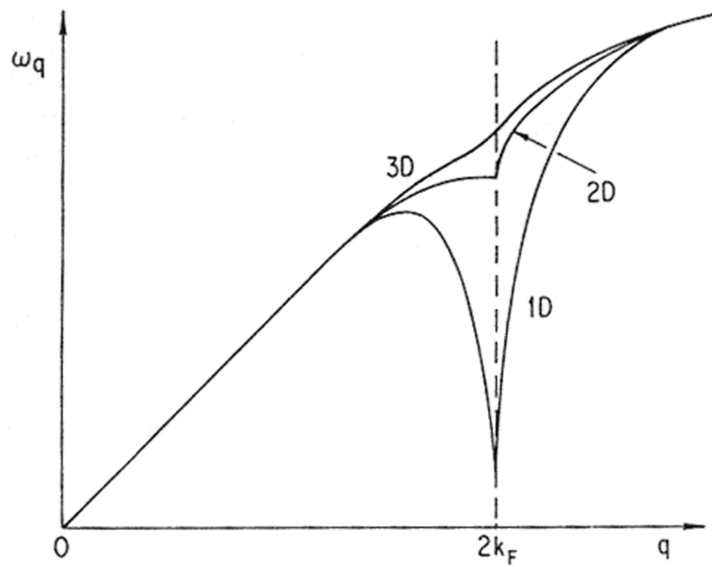


Figure 2.3: The kohn anomaly. (From [3])

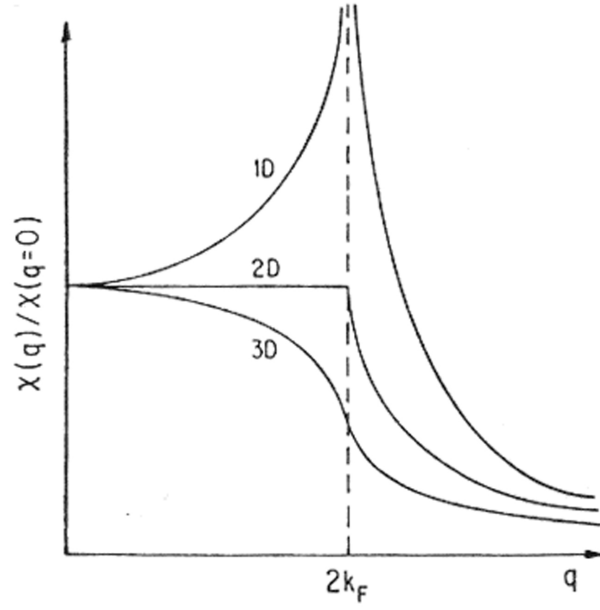


Figure 2.4: Electronic susceptibility as a function of wave-vector q . Particularly, a singularity occurs at $2k_F$ in 1D the susceptibility, leading to a CDW instability. For 2D, there is no singularity, but $\left. \frac{d\chi}{dq} \right|_{2k_F} = -\infty$. (From [3])

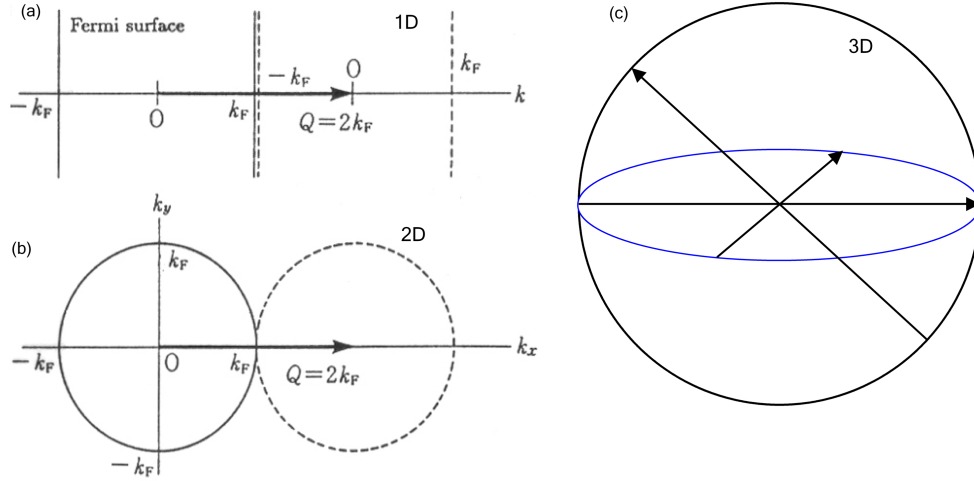


Figure 2.5: FS nesting conditions with different dimensions (a) 1D, (b) 2D and (c) 3D. (Reproduced from [6])

The FS topology determines whether the system matches the CDW instability. Particularly, the density of states near the Fermi level which can be connected via the nesting vector $q = 2k_F$ must be sufficiently high to ensure an energy gain that results from the opening of an energy gap there. Figure 2.5 illustrates the FS nesting for a free-electron band in 1D, 2D and 3D. It is evident that the nesting condition strongly depends on the dimensionality. In the ideal 1D

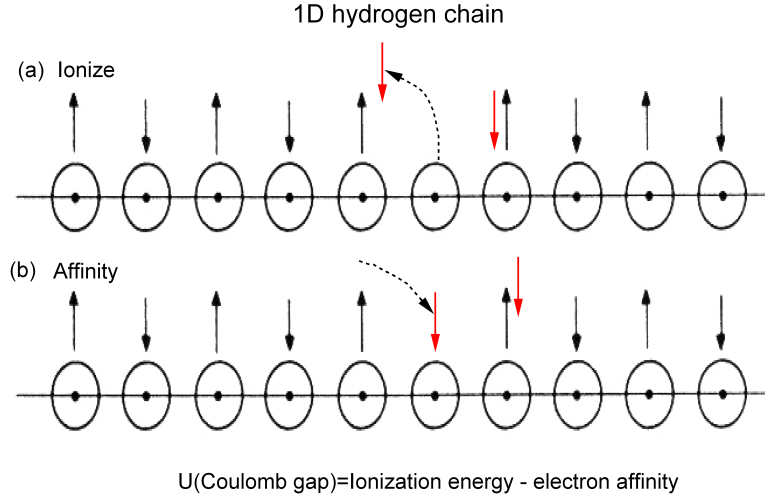


Figure 2.6: Coulomb gap is schematically illustrated in 1D hydrogen chain model. (From [7])

system this requirement is matched by the parallel planes of the FS as shown in Fig. 2.5 (a). They are perfectly nested because the wavevector $2k_F$ matches them identically onto each other. The gap develops in the same way as in 2D and 3D systems if they fulfill the nesting conditions. But in high dimensional system the nesting cannot gap the whole FS. The CDW transition is normally not accompanied by a metal-insulator transition. We will see this in 2H-TaS₂ and an exception in 1T-TaS₂ in Chapter 4.

2.2 Metal-insulator Mott transition

We consider the arrangement of hydrogen atoms (N electrons) with Bohr radius a_B in a one dimensional chain with lattice constant a (see Fig. 2.6). Here we make a rather drastic assumption that the effective electron-electron interaction will be local. Without structural deformation, such idealized half-filled 1D system would be a metal according to band theory. The elementary charge-fluctuation can be broken down into two separate processes. Figure 2.6 schematically shows the ionization and affinity process of removing and adding one electron, respectively, from the 1D hydrogen chain. The intra-atomic energy, ionization energy minus electron affinity, is called Coulomb gap or "Hubbard" U ,

$$U = E(H \rightarrow H^+) - |E(H \rightarrow H^-)| = E(H^-) + E(H^+) - 2E(H). \quad (2.4)$$

We further assume that electrons may hop between neighboring atoms. The dispersion of independent electrons (tunneling between nearest neighbors) can be modeled by a simple

tight-binding (TB) approximation,

$$\varepsilon(k) = -2t \sum_{l=1}^d \cos(k_l a) \quad (2.5)$$

with a bandwidth $W = 2Zt$, where $Z = 2d$ (d is the dimension, here $d=1$) is the number of nearest neighbors and $t > 0$ is the hopping amplitude which depends on a/a_B . The positive sign of t guarantees the proper low-density limit.

If $W < U$ the gain in kinetic energy is smaller than the cost in Coulomb energy, and electrons are localized in their sites. We can see this by considering the addition or removal of one electron. Here in 1D hydrogen chain we have this relation $W \ll U$ because the lattice constant a is much larger than a_B that the overlap between the atomic wave function is small. And every site is strongly occupied in the ground state due to the half filling band. This picture is schematically illustrated in Fig. 2.7. On the one hand, when adding an electron the system needs an energy $\mu^+(N) = E_0(N+1) - E_0(N)$, which is given by $\mu^+(N) = U - W_{up}/2$. Here W_{up} is the bandwidth of "upper Hubbard band". Actually, it forms due to the charge excitations with energy U while an extra electron is added into the ground state of the half-filled electron system (Fig. 2.7 (a)). On the other hand, when removing an electron the system costs energy $\mu^-(N) = E_0(N) - E_0(N-1)$, which is given by $\mu^-(N) = W_{low}/2$. Similarly, W_{low} is the bandwidth of the "lower Hubbard band" which is constituted thanks to the removal of a charge from the half-filled ground state (Fig. 2.7 (b)). Due to the half-band filling and $(W_{up} + W_{low})/2 \ll U$, we would expect a gap opening for charge excitations, that is $\Delta\mu(N) = \mu^+ - \mu^- = U - (W_{up} + W_{low})/2 > 0$. Therefore, we find that expression $(W_{up} + W_{low})/2 \approx W \ll U$ is satisfied and a gap occurs in this half band filling, thus the system is an *insulator*.

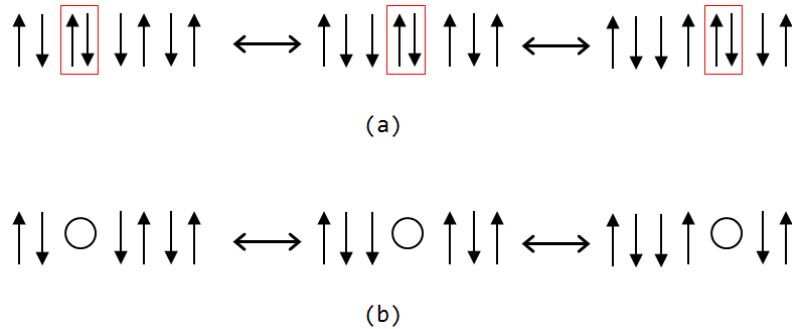


Figure 2.7: Cartoons for a upper and lower Hubbard band [8].

Now, if we could reduce the distance between hydrogen atoms, reducing the lattice constant a closer to a_B , the overlap between the atomic wave function will increase. As a consequence the sum bandwidth of the upper and lower Hubbard band will increase until $W \gg U$,

leading to a closing of the gap for charge excitations. Low energy excitations hardly change the charge distribution and thus are gapless. In this circumstance, $W \gg U$, the system is a paramagnetic *metal*.

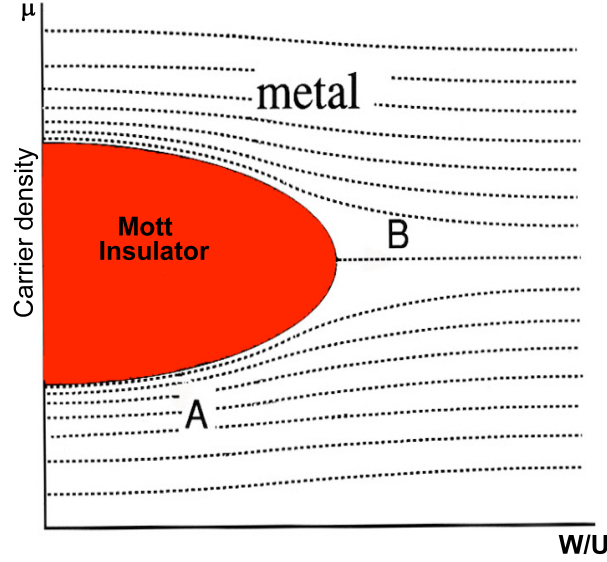


Figure 2.8: Schematic phase diagram of Metal-insulator Mott transition. (From [7])

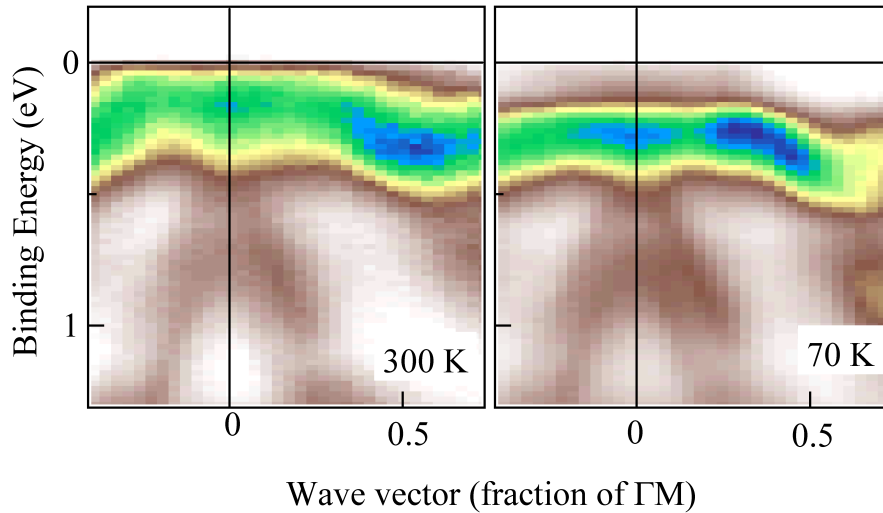


Figure 2.9: Metal-insulator Mott transition occurs in 1T-TaSe₂. Reproduced from [9].

We still leave one situation unconsidered, around $W \approx U$, where there is the balance point between metal and insulator. Controlling one parameter, W or U , would break the equilibrium of the system, leading to a metal-insulator transition (MIT) since the upper and lower Hubbard

band tend to overlap. The generic phase diagram (Fig. 2.8) vividly illustrates that the MIT is determined by the correlation strength (U/W) and the carrier density μ . Among 2D TMDCs, the 1T polytype CDW TaS₂ and TaSe₂ are such systems, which would undergo a MIT with decreasing temperature. Figure 2.9 shows such a MIT in a quasi-2D CDW 1T-TaSe₂ [9] which exhibits a narrow Ta d band crossing the Fermi level at $T=300$ K, indicating metallic behavior. However, at $T=70$ K the Ta d spectral weight is narrower and clearly removed from the Fermi level, eventually a gap has appeared. This MIT could be interpreted in the framework of metal-insulator Mott transition, which is schematically illustrated in the Fig. 2.10. At high temperature, above MIT temperature, the ratio U/W is apparently smaller than the critical value for the MIT, and the metallic band is stable (Fig. 2.10 middle). But this is not necessarily true at all temperatures, because the CDW amplitude which dominates the hybridization and therefore the width of the Ta d subbands is not a constant. Below the MIT temperature, due to the narrowing of the topmost Ta d subband, the U/W ratio is larger than the critical limit, triggering a sudden removal electron density near the Fermi level, and a correlation gap finally occurs (Fig. 2.10 bottom). A more detail discussion will be presented in Chapter 4 about another similar CDW system - 1T-TaS₂.

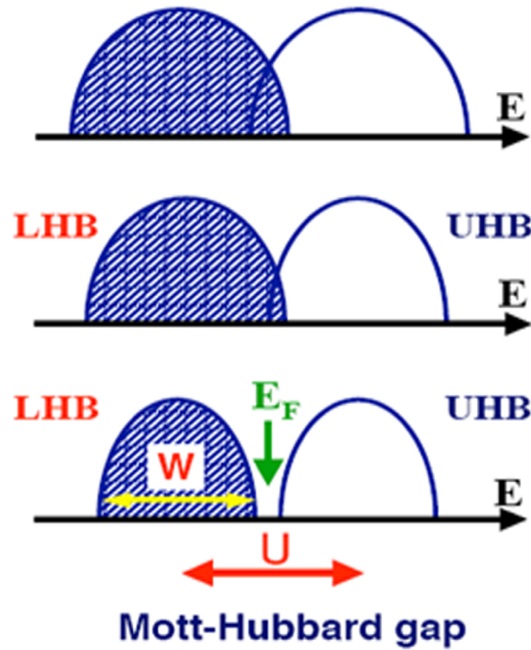


Figure 2.10: Metal-insulator Mott transition controlled by correlation strength U/W . (From [7])

2.3 Superconductivity

The high temperature superconductivity is intimately linked to the 2D nature of cuprates. A review of the theory of SC is of course well beyond the scope of this thesis. Nevertheless, it is useful here to recall a few fundamental ideas.

The main characteristics of SC are the following:

- (1) Zero resistivity,
- (2) Perfect diamagnetism (Meissner effect) for conventional superconductors: no magnetic field inside a superconductor in its superconducting state - the magnetic flux is totally expelled from a superconductor,
- (3) flux quantization,
- (4) Josephson effects,
- (5) gaps in the elementary excitation energy spectra.

2.3.1 Phenomenological theories of superconductivity

London equation

The first phenomenological theory of SC was built by F. London and H. London in 1935 [10]. It is based on empirical facts and not deduced from any microscopic mechanism within the material. The two London equations were derived by taking both zero resistance and the Meissner effect into account. They assumed that only a fraction n_s of the total number of conduction electrons can give rise to a super-current. Here n_s is the number density of the superconducting electrons. When $T > T_c$, $n_s = 0$, and $T \ll T_c$, n_s approaches the whole electron density n . The two London equations are:

$$\frac{\partial \vec{j}}{\partial t} = \frac{n_s q^2}{m} \vec{E}, \nabla \times \vec{j} = -\frac{n_s q^2}{m} \vec{B}, \quad (2.6)$$

where q and m are the carrier charge and mass, \vec{E} and \vec{B} are the electric and magnetic fields vectors, \vec{j} is the current density. These two equations describe the behavior of a superconductor in an electromagnetic field. The first one reflects perfect conductivity, while the second one is a mathematical formulation of the Meissner effect. This equation can be easily transformed as:

$$\nabla^2 \vec{B} = \vec{B} / \lambda_L^2, \quad (2.7)$$

where $\lambda_L = \sqrt{\frac{m}{\mu_0 n_s q^2}}$ is called the London penetration depth (μ_0 is the magnetic permeability of vacuum). λ_L defines the length-scale for the penetration of the magnetic field into a superconductor. Typical values of λ_L are of the order of 100 Å (~ 1000 Å in high- T_c cuprates; notice that this quantity is directly related with the density of superconducting electrons).

Ginzberg-Landau theory

Another phenomenological theory was established in 1950 by Ginzberg and Landau. This theory is known as the Ginzberg-Landau (GL) theory. It describes the superconducting state by introducing the concept of a complex position-dependent order parameter – the wavefunction $\Psi(r)$ of the superconducting electrons. $\Psi(r)$ can be expressed as:

$$\Psi(r) = |\Psi(r)| e^{i\varphi(r)}, \quad (2.8)$$

where $\varphi(r)$ is spatially varying phase. $\Psi(r) \neq 0$ in the superconducting state, while $\Psi(r) = 0$ above T_c . The superconducting electron density n_s is related to $\Psi(r)$ as follows:

$$n_s(r) = |\Psi(r)^* \Psi(r)|. \quad (2.9)$$

The velocity operator of an electron in the magnetic field is

$$\vec{\nu} = -(i\hbar\nabla + q\vec{A})/m, \quad (2.10)$$

where \vec{A} is the vector potential of the electromagnetic field. And the current density is

$$\vec{j} = q\Psi * \vec{\nu}\Psi = \frac{n_s q}{m} (\hbar\nabla\varphi - q\vec{A}). \quad (2.11)$$

Taking the curl of both sides of Eq. 2.11, I get the second London equation (Eq. 2.6). The basic postulate of the GL theory is that when Ψ is small and varies slowly in space, the total free energy can be expanded in a series of even powers of $\Psi(r)$ and its spatial gradients. The coefficients of its quadratic and fourth power terms are α and β , respectively. By minimizing the free energy with respect to fluctuations in the order parameters and the vector potential, one gets the two GL equations:

$$\frac{1}{2m} (i\hbar\nabla + q\vec{A})^2 \Psi + \alpha\Psi + \beta |\Psi|^2 \Psi = 0 \quad (2.12)$$

$$\vec{j}_s = -\frac{i\hbar q}{2m} (\Psi^* \nabla \Psi - \Psi \nabla \Psi^*) - \frac{q^2}{m} |\Psi|^2 \vec{A}. \quad (2.13)$$

The above two equations are known as GL first and second equations, respectively. With appropriate boundary conditions, various properties of the superconducting state can be calculated.

2.3.2 BCS theory

The London equations and GL theory are phenomenological theories based on some assumptions. Scientists were seeking for a microscopic theory for superconductivity based on quantum

mechanics. The successful theory was achieved by Bardeen-Cooper-Schrieffer (BCS) [11]. The BCS theory revealed that the electrons in certain circumstances can attract each other through electron-phonon interaction. The theory shows that only the electron pairs near the Fermi surface can effectively attract each other. Because the Pauli exclusion principle leads to an effective repulsion, the electrons must be paired with opposite spins. Therefore, one needs just only to consider the electron pairs near the Fermi surface with opposite momenta and spins interacting with phonons. At sufficient low temperature this attraction dominates over the Coulomb repulsion, leading to a formation of bound electron pairs (Cooper pairs).

The BCS theory is a typical mean-field theory, *i.e.* no fluctuation effects are taken into account. Cooper pairs that are formed between electrons of opposite momenta and opposite spins above the Fermi sea form a bound state and each of them has lower energy than twice the Fermi energy E_F , as long as a weak attractive interaction between them. Cooper pairs do exist in the superconducting state, paring up and moving together, not bumping into each other, and not scattering off the imperfections in the superconductors. When there is attraction between electrons, the Fermi surface is no longer stable and the superconducting ground state should be formed by Cooper pairs.

Only electrons within $\sim k_B T_c$ (k_B is the Boltzmann's constant) of the Fermi energy can be involved into the superconducting pairing. Their momentum range is $\Delta p \approx k_B T_c / \nu_F$, where ν_F is the Fermi velocity. According to the uncertainty principle, if the size of the Cooper pair in space is ξ , an electron confined in this space has a corresponding uncertainty in momentum $\Delta p = \hbar / \xi$ and then an uncertainty in kinetic energy is

$$\Delta\left(\frac{p^2}{2m}\right) = \frac{p\Delta p}{m} = \frac{\hbar p_F}{m\xi}, \quad (2.14)$$

where p_F is the momentum at the Fermi energy. The Heisenberg exclusion principle then yields:

$$\xi \geq \frac{\hbar}{\Delta p} \approx \frac{\hbar \nu_F}{k_B T_c} = \xi_0, \quad (2.15)$$

where ξ_0 is called the coherence length. The coherence length characterizes spatial correlations in a superconductor and roughly represents the size of a Cooper pair. The magnitude of ξ_0 for traditional superconductors is the order of $\sim 10^4$ Å, however, it is only ~ 10 Å for high- T_c superconductors.

Another important result of the BCS theory is the energy gap which is an order parameter. The wave functions of the Cooper pairs form a phase-coherent condensed state – the superconducting state which is lower in energy than the ground state of the non-interacting electron gas. There is a minimum energy E_g (or 2Δ) at the Fermi level necessary to break a Cooper pair, which leads to an energy gap in the excitation spectrum in the superconducting state. The BCS theory predicts that the energy gap at zero temperature $\Delta(0)$ is related to the

coherent length by

$$\xi_0 = \hbar v_F / \pi \Delta(0). \quad (2.16)$$

The theory also deduced the gap value with T_c as:

$$E_g = 2\Delta(0) = 3.52 k_B T_c. \quad (2.17)$$

Experiments have confirmed that such a scaling is fulfilled for a large number of superconducting materials in the weak coupling limit, as illustrated in Fig. 2.11 (a). In BCS theory the energy gap represents the strength of the pairing. The larger the gap, the more energy is required to break the pair and the higher the critical temperature. The gap is also temperature dependent and it decreases to zero near T_c following the relation:

$$\frac{\Delta(T)}{\Delta(0)} \approx 1.74(1 - T/T_c)^{0.5}. \quad (2.18)$$

The experimental gap value vs temperature and the BCS calculated $\Delta(T)$ - T matches quite well, as shown in Fig. 2.11 (b).

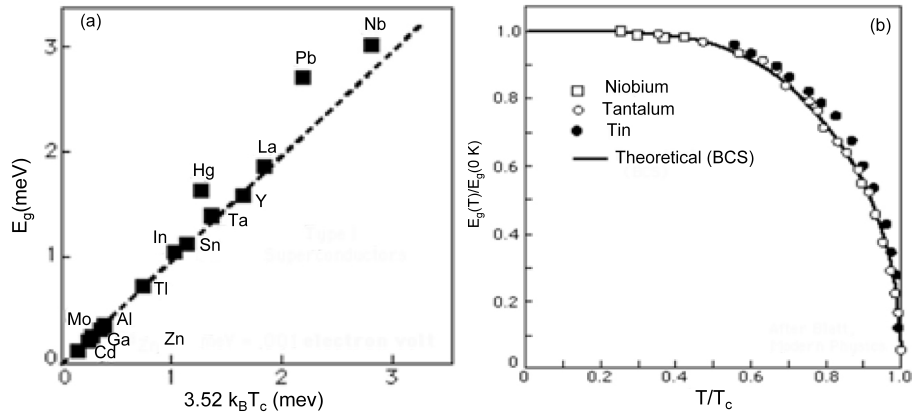


Figure 2.11: (a) Zero temperature energy gap vs T_c (from [12]), and (b) energy gap vs temperature for traditional superconductors (From [13]).

2.3.3 High- T_c superconductors

In the past two decades, following the discovery of superconductivity in $\text{La}_{2-x}\text{Ba}_x\text{CuO}_4$ by Bednorz and Müller [14], a large number of related compounds with high superconducting transition temperatures have been found. For example, when La is replaced by Y, superconductivity for the first time exceeds liquid N_2 temperature (~ 77 K) in $\text{YBa}_2\text{Cu}_3\text{O}_{6+x}$ ($T_c = 92$ K) [15]. The highest-temperature superconductor (at ambient pressure) is $\text{HgBa}_2\text{Ca}_2\text{Cu}_3\text{O}_{8+\delta}$, at 135 K, and possibly 164 K under high pressure [16]. The large increase of T_c was the

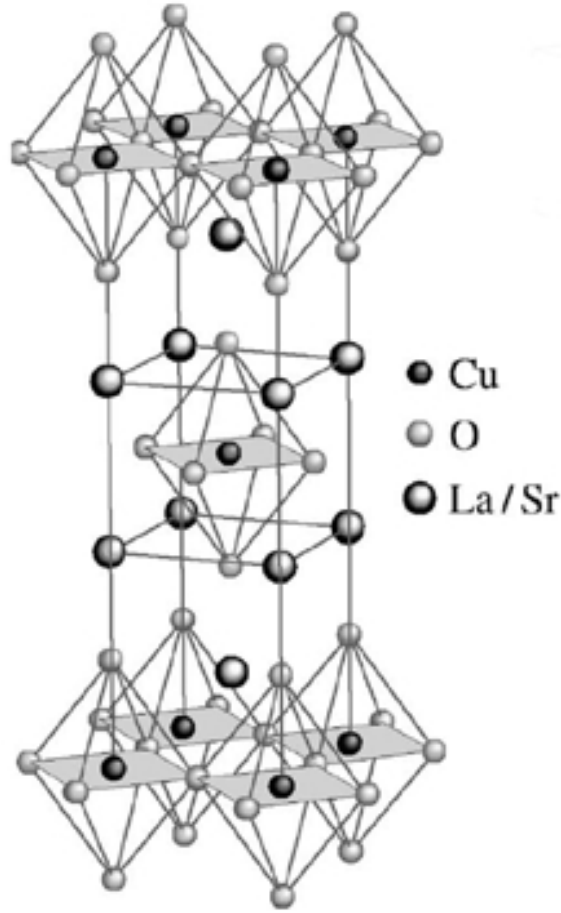


Figure 2.12: An example of the layered perovskite structure in $La_{2-x}Sr_xCuO_4$ (from [17]).

most spectacular achievement related to the high- T_c superconductors. But the more important challenge is to reveal the origin of high T_c in these compounds.

Common features in all high- T_c cuprates

The most common feature of these HTSC is a layered perovskite crystal structure containing CuO_2 planes separated by block layers or the so-called *charge reservoir layers* (Fig. 2.12). The layered structure of cuprates is highly anisotropic, making their properties quite different from those of conventional superconductors. The conductivity in the normal state along the c axis is about 2 to 4 orders of magnitude smaller than that along directions parallel to the layer. Furthermore, the extremely small and anisotropic coherence length ($\xi_{ab} \sim 10 \text{ \AA}$, $\xi_c \sim 1 \text{ \AA}$) indicates strong 2D character [18]. Usually the block layers are insulating and have almost no contributions to the low-energy electronic states. By substituting different elements in the reservoir layers or by varying their oxygen content one can dope charge carriers into the CuO_2 planes which possess the energy states near the Fermi level and thus dominate the low-

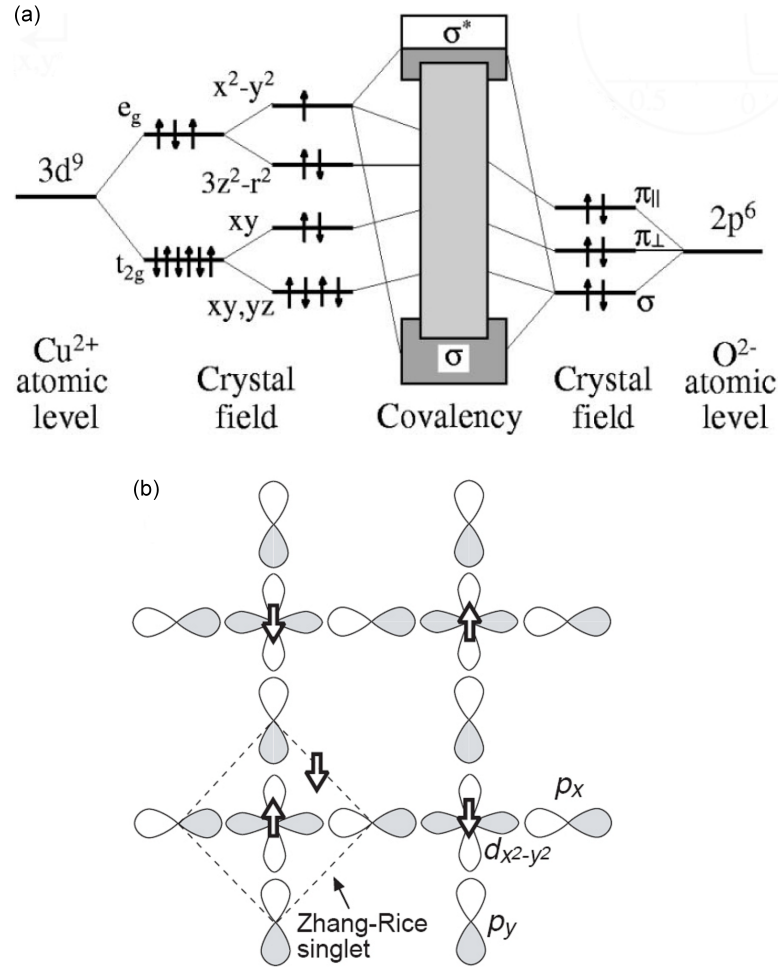


Figure 2.13: (a) An example of the layered perovskite structure in $La_{2-x}Sr_xCuO_4$ (from [17]). (b) Schematic diagram for the Cu 3d and O 2p orbitals in the cuprates (from [19]).

energy physics. Therefore, the CuO₂ planes are essential to the electronic and superconducting properties.

Figure 2.13 schematically illustrates the Cu-O bonding in the cuprates. The octahedral crystal field splits the Cu 3d orbitals into e_g and t_{2g} manifolds, which are further split in the actual tetragonal symmetry and divided in four sublevels. Similar splitting into π and σ levels occurs at the O 2p orbitals. In the CuO₂ plane, the d_{x²-y² band originated from Cu has the highest energy among the five d bands, because the Cu d_{x²-y² orbital well hybridizes with oxygen p orbitals through the in-plane Cu-O bonds which have shorter length than the out-of-plane Cu-O bonds. Therefore, in the parent compound with nine d electrons (or one d hole), the d_{x²-y² band is half-filled and each Cu atom has spin 1/2. Fig 2.13 (b) illustrates the CuO₂ plane with the copper d_{x²-y² orbitals together with oxygen 2p_x and 2p_y orbitals. In a system}}}}

where electron-electron correlations are negligible, the Cu $d_{x^2-y^2}$ orbitals and O $2p_x$ and $2p_y$ orbitals form bonding, non-bonding and antibonding bands, as illustrated in Fig. 2.14. The antibonding band is half filled, thus the band theory would predict a non magnetic metallic ground state, while a gap of 1.5 eV is found experimentally and actually the system is an antiferromagnetic (AFM) insulator [20]. This failure of the traditional band theory is due to the Coulomb repulsion U which causes the electrons to localize on the ions and form an AFM lattice. When the Coulomb repulsion U is larger than the bandwidth W of the conduction band, the conduction band splits into a fully occupied lower Hubbard band (LHB) and a completely empty unoccupied upper Hubbard band (UHB) as discussed in Section 2.2. Then the system is a Mott insulator. In another extreme situation, when the Coulomb repulsion U is larger than the copper oxygen charge transfer energy, *i.e.* the energy required to transfer the hole from the Cu^{2+} ion to the O ligands, Δ ($U > \Delta$), the system turns into a charge transfer insulator, as illustrated in Fig. 2.14 (c). The finite hybridization between the correlated Cu and the O orbitals forms a singlet, a nonbonding, and a triplet state, where the singlet state is the so-called Zhang-Rice singlet (ZRS) [21]. These states are very important because the SC state is achieved by doping the insulating parent compound with holes, and therefore populating these states. The large energy separation between the singlet and the triplet is 3.5 eV which has been calculated by Eskes and Sawatzky [22], indicating that the triplet state can be excluded out from the low-energy physics. It was suggested by Anderson [23] that the single band Hubbard model can describe the physics of cuprates:

$$H = -t \sum_{\langle i,j \rangle, \sigma} (c_{i,\sigma}^\dagger c_{j,\sigma} + H.c.) + U \sum_i n_{i,\uparrow} n_{i,\downarrow} \quad (2.19)$$

The first part of this Hamiltonian is a kinetic-energy term proportional to the nearest-neighbor (NN) hopping amplitude t , and the second part contains the Hubbard U term that favors electron localization. Here $c_{i,\sigma}^\dagger$ ($c_{j,\sigma}$) creates (annihilates) an electron or hole on site i with spin σ , $\langle i, j \rangle$ identifies NN pairs. In the strong-coupling limit ($U \gg t$) this Hamiltonian can be reduced to the t - J model, which is more commonly considered to represent the low-energy excitations of the cuprates:

$$H = -t \sum_{\langle i,j \rangle, \sigma} (b_{i,\sigma}^\dagger b_{j,\sigma} + H.c.) + J \sum_{\langle i,j \rangle} (\vec{S}_i \vec{S}_j - \frac{n_i n_j}{4}), \quad (2.20)$$

where the operator $b_{i,\sigma} = c_{i,\sigma}(1 - n_{i,-\sigma})$ excludes double occupancy, $J = 4t^2/U$ is the antiferromagnetic exchange coupling constant, and \vec{S}_i is the spin operator. At half filling, as charge excitations are gapped, we find at low energy only spin excitations are governed by the antiferromagnetic Heisenberg Hamiltonian $H = J \sum \vec{S}_i \vec{S}_j$ (the constant term $-n_i n_j/4$ is usually neglected).

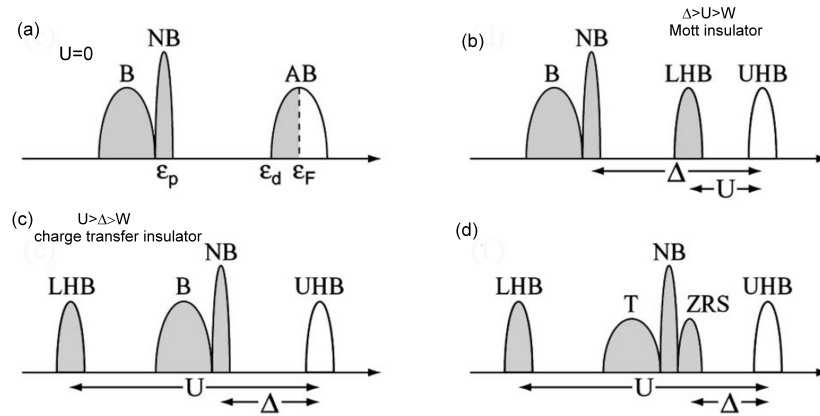


Figure 2.14: Zaanen-Sawatzky-Allen scheme taken from [17].

Chapter 3

Description of the experiment

In this chapter I will describe some relevant aspects of the experimental set-up, including preparation, characterization and measurement on the samples studied in the thesis. And I will also introduce the ARPES technique which I have exploited during the whole process of this work at EPFL and at Swiss Light Source.

During an ARPES experiment, electrons are extracted from the sample with a monochromatic light. The angle and the energy of the photoelectrons are then analyzed. Simple conservation rules lead directly to the band diagram ($E_B(\vec{k})$) for simple materials. A more complex analysis of the data allows us to extract precious information on the electron correlations and the dressing of the quasiparticles by the low energy excitations in the material. ARPES is a very powerful technique because experimental data are in principle comparable to the single-particle spectral function (see below) which contains most of the physics and can be calculated by theoreticians for a given model. We will see also that ARPES allows us to follow the evolution of the Fermi surface with respect to temperature. Nevertheless, an experiment is subject to some drastic restrictions.

- The sample must be a conductor.
- The momentum can only be relevant for crystalline structures. Thus the crystallographic structure must be well ordered.
- The energy of the incoming light is linked to the momentum resolution and to the momentum detection limit. Therefore, UV photons (from a few eV to 100 – 200 eV) are commonly used for ARPES. The short mean free path of UV photoemitted electrons in the crystals restrains the probing depth of the technique to the surface atomic planes. Thus, the samples must be clean and well ordered at the surface. The physics of the surface electrons must also be relevant.

- The photoelectrons are collected by a detector with distance around 1 m from the sample, so - for practical reason - the ARPES experiments are performed under vacuum.

Two-dimensional materials are perfectly suited for ARPES experiments. In Lausanne and in SLS, experiments were performed under ultrahigh vacuum (UHV) and the samples were cleaved *in-situ* to obtain clean surface. Both of these two set-ups are adapted to state of the art photoemission experiments.

3.1 Experimental technique of ARPES

3.1.1 The electron analyzer

The analyzer of photoelectrons is the heart of the ARPES experimental technique. The data used in the present work were acquired using modern Scienta SES20002 electron analyzer and SPECS PHOIBOS 150 Hemispherical analyzer (Fig. 3.1). Both analyzers are electrostatic analyzers, optimized for high transmission and maximum energy resolution. These electron analyzers collect the photoemitted electrons as a function of their kinetic energy and emission angle. The hemispherical energy analyzer and the lens system are constructed entirely from non-magnetic materials inside the μ -metal shielding. The electric grounding and the magnetic shielding provide a perfect control of the electrons trajectory in the analyzer.

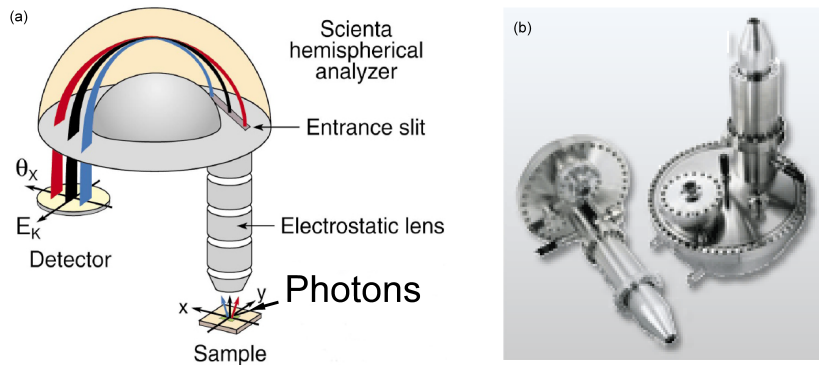


Figure 3.1: (a) Schematic view of a hemisphere electron analyzer. (b) Photo of SPECS PHOIBOS 150 Hemispherical analyzer.

During the photoemission process, the electrons are emitted from the sample into a cone and collected by the electronic lens system. Then they are focused by the lens and reach to the exit plane of the analyzer at different positions depending on the direction of their initial momentum. At the same time the analyzer accepts only the electrons whose energy correspond

to the user defined pass energy ¹. Other electrons with energies substantially different from the pass energy cannot reach the detector (Fig. 3.1 (a)). The accepted photoelectrons are accelerated towards a 2D phosphorescent screen. The intensity map is recorded with a high sensitivity CCD camera and quantitatively represents the number of photoelectrons versus their angle of emission and their kinetic energy (E_{kin}). The images can be processed by a computer. The processed images link the the binding energy (E_B) of the quasiparticles (QP) in the crystal to their momentum (\vec{k}). A set of intensity images can be collected when moving the normal and azimuthal angle of the sample with respect to the entrance slit. One can scan the electronic properties in the reciprocal space along k_x and k_y by varying the normal and azimuthal angles. For example, a complete scan of the electronic properties near the Fermi level allows the experimentalist to plot the Fermi surface of the studied material.

The energy resolution ΔE of the analyzer is determined by the mean slit width S ($S = (S_1 + S_2)/2$, S_1 and S_2 are the width of entrance and exit slit, respectively), the pass energy E_p , the mean diameter of the analyzer D ($D = (D_{in} + D_{out})/2$, D_{in} and D_{out} are the radius of inner and outer hemisphere, respectively), and the analyzer acceptance half angle α in the dispersion direction. That is

$$\Delta E = E_p * (S/2D + \alpha^2/4). \quad (3.1)$$

On the one hand, clearly, smaller slit and pass energy lead to better resolution. The energy resolution ΔE can be obtained by measuring the Fermi edge of metallic samples, for example polycrystal Ag or Au. The limited resolution is $\Delta E < 2$ meV in our system. The energy resolution is also influenced by the spot size of the UV source - the smaller spot size the better resolution. On the other hand, the intensity of the electrons reaching the detector is inversely proportional to the UV light spot size, E_p and S , which results in a trade off between the intensity and resolution. In reality, in order to get more intensity and to record data related to large parts of the BZ during the lifetime of the sample, we usually use relatively large pass energy and big slit. Low pass energy and small slits are only used for ultimate resolution data recording for the study of the electronic properties at the Fermi level and for some precise angles.

For standard measurements, the resolution is better than 10 meV and 12 meV for SPECS PHOIBOS 150 and Scienta SES2002, respectively. The solid angle of the emitted electrons entering into the analyzer is determined by the width of the entrance slit. It determines the angular resolution in the dispersive direction of the detector. The angular resolution is estimated experimentally better than 0.2° and 0.15° for SPECS PHOIBOS 150 and Scienta

¹For a fixed electrical field gradient, only particles with kinetic energies in a particular energy, which is called pass energy (E_p), are able to pass through the full deflection angle from the entrance slit S_1 to the exit plane S_2 . Particles with higher passe energy approach the outer hemisphere, whereas particles with lower kinetic energy are deflected toward the inner hemisphere.

SES20002, respectively.

The analyzer can be operated in two different modes ²:

(i) Fixed retarding ratio mode

In this mode all electrons are decelerated with the same fixed factor $R = E_{kin}/E_P$. Thus the pass energy is proportional to the kinetic energy. The intensity increases with the kinetic energy $I \sim E_{kin}$, while the energy resolution is decreasing.

(ii) Fixed analyzer transmission mode

In this mode, E_P and ΔE in Eq. 3.1 are adjustable constants. The signal of all electrons, independent of the kinetic energy, are measured with the same resolution and the intensity decreases with kinetic energy: $I \sim 1/E_{kin}$.

3.1.2 EPFL and SLS set-ups

Both the equipments at Lausanne and SLS are under ultrahigh vacuum (UHV). The samples can be introduced in the UHV chamber with a fast pumping loadlock in a few hours. Once the samples are under UHV they can be transferred to the analyzer chamber with a set of manipulators and wobble sticks. The manipulator of the photoemission chamber has 4 purposes:

- it keeps the surface of the sample exactly at the focus plane of the analyzer
- it fixes the sample normal and azimuthal angle with respect to the entrance slit of the analyzer (so k_x , k_y)
- it allows the experimentalist to move the light on the sample surface and to choose which part of the sample is more promising
- the manipulator - thus the sample - is cooled by He cryostat. The ultimate temperature for the sample is 10 K and around 20 K at SLS and Lausanne, respectively. Variable temperature experiments can be performed up to room temperature.

The photons are provided by a synchrotron source at SLS and a helium plasma lamp at Lausanne. Synchrotron sources allow the user to choose the photons energy and the polarization of the monochromatized beam. Our monochromatized plasma lamp has a strongest photon flux at 21.2 eV but the intensity drops drastically for photons lines of higher energy. During operation the vacuum in the analyzer chamber is at the order of 5×10^{-11} mbar at SLS and fixed at 5×10^{-9} mbar at EPFL. Indeed, the lamp is connected to the analyzer chamber at Lausanne and maintaining the plasma requires a high pressure (around 3×10^{-4} mbar) for ultrapure He. For this reason, the lifetime of the samples will considerably be longer at the synchrotron than for an experiment at EPFL.

²See details in the manual of PHOIBOS hemispherical energy analyzer series

The the Specs analyzer was delivered at the beginning of my thesis and the complete set-up was mounted during this period. Our first work was to calibrate and optimize the analyzer with test samples (polycrystalline gold and single crystal Au(111)). Constant efforts were invested in keeping the optimal resolution and efficiency of the apparatus during my thesis.

3.1.3 Sample preparation

Most of the samples discussed in this thesis are single crystals which were grown by chemical-vapor transport by Mr. Helmut Berger (EPFL). These single crystals were characterized by X-ray diffraction, transport measurement or magnetic susceptibility measurement. The *ex situ* preparation usually included mounting the sample on a home-made sample holder with Epoxy silver glue and heat it to prevent charging effect. The samples are azimuthally oriented by means of Laue diffraction (Fig. 3.2 (b)) or oriented *in situ* by low electron energy diffraction (LEED). For the samples related in this work, the samples holders (Fig. 3.2 (a)) were made of Al (Lausanne) and Cu (Swiss Light Source) in order to provide good electrical and thermal contacts with the cryo-manipulator of the analyzer chamber.

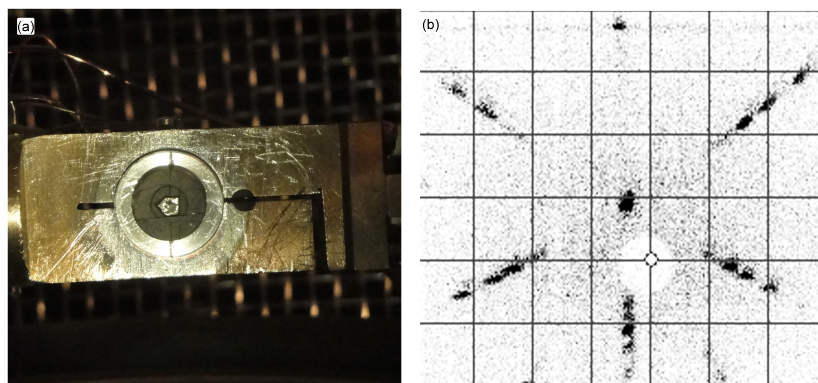


Figure 3.2: (a) Sample on Al sample holder. (b) Laue diffraction pattern of sample for the orientation.

Sample cleavage

Because ARPES is a surface sensitive technique, our samples have to be cleaved *in situ* in UHV just before the ARPES measurement. For example, the transition metal dichalcogenides (TMDs) samples are made of 2D slabs linked by weak Van-der-Waals forces. Thus, it is quite easy to cleave their layered structure with a scotch tape or a slim Al pin as illustrated in Fig. 3.3. We often use a scotch tape for 2D samples at Lausanne whereas glued pins are favored at SLS. The scotch tape is attached to an "O-ring" on one side and stick to the sample on the other side. Pins and scotch tape can be removed *in situ* with a wobble-stick. Both methods lead to

clean and mirror like surfaces with atomic corrugations. Our samples can usually survive in UHV for about 24 hours after cleavage at SLS (6 hours at Lausanne) without any significant alteration of the surface electronic properties.

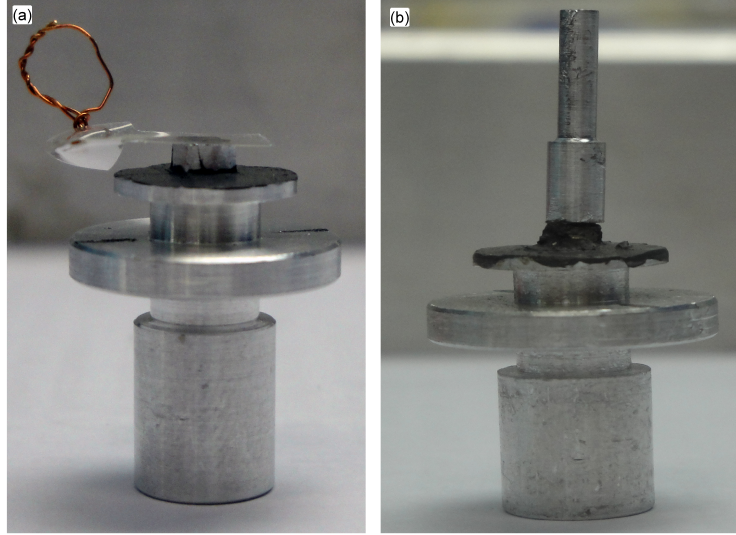


Figure 3.3: Sample assembled with an "O-ring" stripe of a sticky scotch tape (a) and a slim Al pin (b).

3.2 Basic theory of photoemission

3.2.1 The photoelectric effect

The photoelectric effect was first discovered by Hertz in 1887 [24] and was first explained by Einstein [25] 19 years later when the quantum nature of light was developed. This effect was applied by several spectroscopy methods combined under a general name of photoelectron spectroscopy (PES) [26]. PES is now a mature experimental technique, with the ramifications ranging from fundamental to applied physics, and even broad application in industry research and development.

Photoemission is a photon in–electron out experiment, as it is shown in the sketch of Fig. 3.4. The monochromatic photon beam (either from a synchrotron source or a gas lamp) in the UV or X-ray range incidents on a sample, inducing the emission of photoelectrons that can escape from the sample and are detected by the analyzer. The sample could be a solid, a liquid or gas, but in this thesis I only concentrate on solid. The photoelectrons are characterized by their momentum \mathbf{p} , or equivalently by their parallel component along the sample's plane p_{\parallel} and the total kinetic energy.

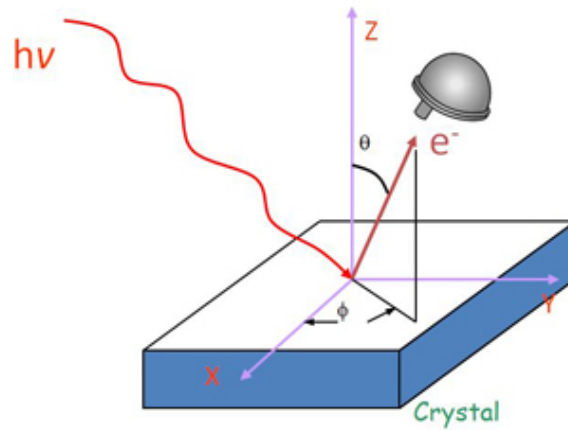


Figure 3.4: Schematic showing the angle-resolved photoemission geometry. The directions of the light and of the photoelectron define the scattering plane. θ is the polar emission angle. (Figure is taken from [27])

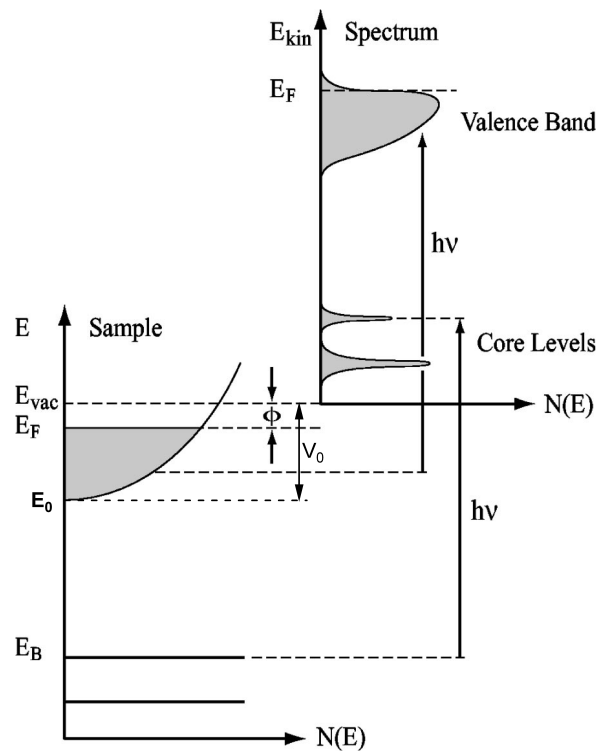


Figure 3.5: Electron transitions in a PES process. Electrons are excited from the solid by incoming photons $h\nu$. When the electrons are emitted into the vacuum level of the sample, they obey the energy conservation law $E_{kin} = h\nu - E_B - \Phi$. [26]

On the one hand, E_{kin} of an excited photoelectron is determined by Einstein's relation, as

the following total energy conservation law

$$E_{kin} = h\nu - E_B - \Phi. \quad (3.2)$$

Here $h\nu$ is the energy of the impinging photons, E_B is the electron binding energy (referenced to the Fermi energy), and Φ is the work function (the energy difference between the Fermi and vacuum levels). Figure 3.5 illustrates schematically the energetics of the photoemission process. Because of the energy conservation function, we can expect the distribution of the excited photoelectrons to reproduce the structures of the distribution of the valence bands and even the core levels.

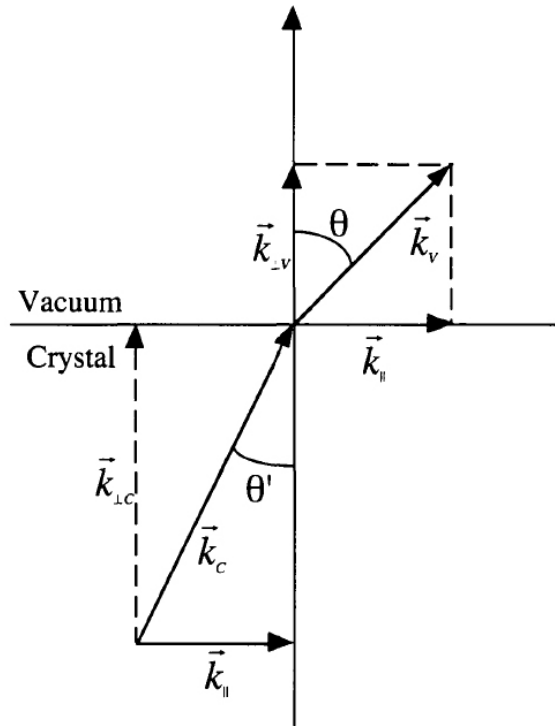


Figure 3.6: Momentum relationship in PES process. Note that only parallel component of the momentum is conserved, k_{\perp} is not conserved across the sample surface due to the lack of translational symmetry along the surface normal.

On the other hand, the parallel photoelectron momentum p_{\parallel} is conserved (Fig. 3.6) if the photon energy is small (if smaller than ~ 100 eV, we can neglect the photon momentum). The momentum conservation law is:

$$p_{\parallel} = \hbar k_{\parallel} = \sqrt{2mE_{kin}} \cdot \sin \vartheta. \quad (3.3)$$

Therefore, the photoemission probes the real information about the electron momentum inside the solid. This conservation law is really useful, in particular to determine the electron properties in low dimension system (CDWs and HTSCs). Upon measuring larger θ angles, the

electrons states in the higher order Brillouin zones can even actually be probed. Note that the perpendicular momentum wave vector k_{\perp} is not conserved across the sample surface due to the surface potential barrier.

3.2.2 Basic principle of ARPES

From the point view of quantum mechanics, the process of photoemission is a very complex phenomenon. However, when a crucial approximation is employed (sudden approximation, details will be discussed below), the photoemission process can be simply described by the Fermi's golden rule. The key point of photoemission is the interaction of a photon with a many-electron system. The initial ground state is assumed as Ψ_i^N and one possible final state is Ψ_f^N . Now we will calculate the transition probability w_{fi} for an optical excitation between these two states. This could be approximately given, as mentioned before, by the Fermi's golden rule:

$$w_{fi} = \frac{2\pi}{\hbar} |\langle \Psi_f^N | H_{\text{int}} | \Psi_i^N \rangle|^2 \delta(E_f^N - E_i^N - h\nu) \quad (3.4)$$

Here $E_i^N = E_i^{N-1} - E_B^k$ and $E_f^N = E_f^{N-1} + E_{kin}$ are the total energy of the system before and after the excitation (E_B^k is the binding energy of photoelectron with kinetic energy E_{kin} and momentum k) and $h\nu$ is the photon energy. For the (limited) intensities encountered even at synchrotrons, only one-photon processes are important. We can therefore retain in the interaction Hamiltonian only terms linear in the vector potential A :

$$H_{\text{int}} \approx -\frac{e}{2mc} (\vec{A} \cdot \vec{p} + \vec{p} \cdot \vec{A}) = -\frac{e}{mc} \vec{A} \cdot \vec{p} \quad (3.5)$$

Here $\vec{p} = -i\hbar\nabla$ is the electronic momentum operator and \vec{A} is the electromagnetic vector potential. In a homogeneous medium, and at least in the UV range, where photon wavelengths are considerably larger than characteristic interatomic distances, \vec{A} can be considered constant (dipole approximation) and therefore $\nabla \cdot \vec{A} = 0$. Notice that in some cases $\nabla \cdot \vec{A}$ might become important at the surface where the electromagnetic fields may have a strong spatial dependence.

One and three step models

In a first approximation, I neglect many-body effects and describe ARPES in a single-particle picture. There are two main approaches to treat this problem: the so called one and three step models [26]. The *one-step model* describe the propagation of the plane wave from outside the solid into the crystal. One can start from Eq. 3.4 to calculate transition probabilities from an initial state inside the solid (a Bloch state) to a final state (reverse LEED state) [26], as

illustrated in Fig. 3.7 (a). In one-step model, photon absorption, electron removal, and electron detection are treated as a single coherent process [17]. However, in this case a complex Hamiltonian including the information from bulk, surface and vacuum has to be applied to describe to bulk, surface and evanescent state, as well as surface resonances. Therefore, in many cases a simpler three step model, although purely phenomenological, can be used (Fig. 3.7 (b)). Within this approach, the photoemission process is subdivided into three independent and sequential steps [26, 28]:

- (1) Optical excitation of the electron in the bulk.
- (2) Travel of the excited electron to the surface.
- (3) Escape of the photoelectron into vacuum.

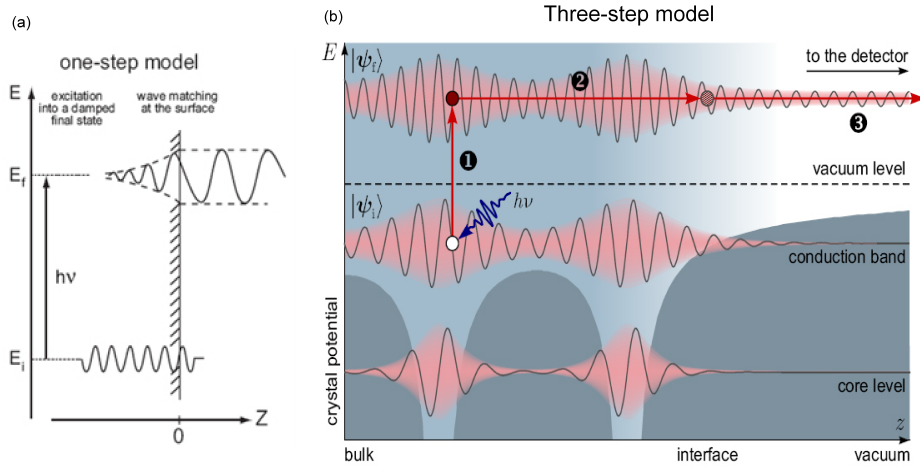


Figure 3.7: Cartoons of one (a) and three (b) steps model of photoemission. (from [26, 29])

The total photoemission intensity is then determined by the product of three independent factors: the total probability for the optical transition between the initial and final states within the bulk, the scattering probability of the traveling electrons by the mean free path, and the transmission probability through the surface potential barrier, depending on the energy of the excited electron and the material work function Φ [17]. In the following we will discuss these three factors, respectively.

In reality, the spectral function can be simplified within the *sudden approximation*, which is extensively used in many-body calculations of photoemission spectra from the interaction electron systems. In evaluating the process of optical excitation (step 1), the energy and momentum conservation can be written as

$$E_f - E_i - h\nu = 0 \quad (3.6)$$

and

$$\hbar k_f - \hbar k_i - \hbar k_\gamma = 0 \quad (3.7)$$

where E_f , E_i and k_f , k_i are the energy and momentum of initial and final state, respectively. k_γ is the wavevector of incident photon. Here the final state describes the "hot" electrons generated in the optical transition step inside the solid. By working at low photon energies (less than 100 eV), one can disregard the photon momentum $\kappa = 2\pi/\lambda$, as for 21.2 eV photons (the HeI α line typically used on ARPES systems equipped with a gas discharge lamp) the momentum is only 0.5% (0.008 \AA^{-1}) of the typical Brillouin-zone (BZ) size of the cuprates ($2\pi/a \simeq 1.6 \text{ \AA}^{-1}$). Thus as illustrated in Fig. 3.7 (b), in the reduced BZ the optical excitation process is a "vertical" initial to final state transition ($k_f = k_i$).

To simplify the problem, in the second step – transporting electrons to the surface – we only consider those electrons reacting to the surface without inelastic scattering. A classical treatment to the transport can be described by an effective mean free path of the photoelectrons [26]. Those inelastic scattering electron will be treated as a continuous background in the spectra. In the further analysis, these background will be subtracted or skipped.

Now let us consider the third step of the photoemission, namely the transit of the electron through the solid-vacuum interface, which can be described by a transmission function which, generally, is related to the work function Φ . From the energetics of the photoemission process (Fig. 3.5), we obtain Eq. 3.2 and 3.3. And due to the broken translational symmetry along the vertical direction, k_\perp is not conserved, which gives more difficulty to get a complete determination of k_\perp unless the dispersion for the final state electrons inside the solid is known. In fact we can apply the free-electron final state model to solve this problem. In this model, we have

$$E_f(k) = \frac{\hbar^2 k^2}{2m} - |E_0| = \frac{\hbar^2 (k_\parallel^2 + k_\perp^2)}{2m} - |E_0| \quad (3.8)$$

As shown in Fig. 3.5, E_0 is the energy of band bottom (Both E_0 and E_f are relative to the Fermi energy E_F , and E_{kin} is relative to E_{vac}). Besides,

$$E_f = E_{kin} + \Phi. \quad (3.9)$$

Then combined with Eqs. 3.3 and 3.8, we get

$$k_\perp = \frac{\sqrt{2m(E_{kin} \cos^2 \theta + V_0)}}{\hbar} \quad (3.10)$$

Here $V_0 = |E_0| + \Phi$ is the so called inner potential, describing the energy relative to the E_{vac} . Therefore, when the measured kinetic energy E_{kin} , the emitted angle θ and the inner potential V_0 are available, we can use Eq. 3.10 to calculate k_\perp . Band mapping is easier in two-dimensional (2D) system, e.g. at surfaces and in layered materials, where only k_\parallel is a good quantum number and the rather difficult to determine k_\perp can be neglected. Full 3D

band mapping requires collecting ARPES data from different crystal surfaces, and the initial states are identified by a triangular procedure. Many of the rather specialized techniques are discussed in Ref. [26].

3.2.3 Sudden approximation

In the previous section we only consider non-interaction electrons. Now it is certainly valuable to think about how the spectral properties are modified when the interactions among electrons, or between the electrons and other excitations are large. New structures, containing much useful information on the interacting system, will appear. In order to understand and exploit the spectral features in the interacting electron system we have to reconsider Eq. 3.4. In the following we will separate the wave function in Eq. 3.4 into the product of two wave functions: photoelectron wave function ϕ_f^k and the final state wave function of the $(N-1)$ electron system left behind – Ψ_f^{N-1} . In this assumption we use the so called *sudden approximation* to describe the photoemission process with no post-collisional interaction between the photoelectron and system left behind (in other words, the photoelectron is instantaneously decoupled from the remaining $(N-1)$ -electron system). The N -particle final state Ψ_f^N can be written as

$$\Psi_f^N = \mathbf{A} \phi_f^k \Psi_f^{N-1} \quad (3.11)$$

where \mathbf{A} is an operator that properly antisymmetrizes the N -electron wave function so that the Pauli principle is satisfied³. However, experiments have shown that this \mathbf{A} is well satisfied even very close to the excited photoemission threshold. The initial state can be written as a product of a one-electron orbital ϕ_i^k and an $(N-1)$ -particle term:

$$\Psi_i^N = \mathbf{A} \phi_i^k \Psi_i^{N-1} \quad (3.12)$$

Here Ψ_i^{N-1} can be expressed as $\Psi_i^{N-1} = c_k \Psi_i^N$, where c_k is the annihilation operator for an electron with momentum k . Notice that Ψ_i^{N-1} is not an eigenstate of $(N-1)$ particle Hamiltonian, but is just what remains of the N -particle wave function after having pulled out one electron. At this point, we can rewrite the Eq. 3.4 as

$$w_{fi} = \frac{2\pi}{\hbar} \left| \left\langle \phi_f^k | H_{\text{int}} | \phi_i^k \right\rangle \left\langle \Psi_m^{N-1} | \Psi_i^{N-1} \right\rangle \right|^2 \delta(E_f^N - E_i^N - h\nu) \quad (3.13)$$

Here Ψ_m^{N-1} is the eigenfunction of the $(N-1)$ -electron Hamiltonian with energy E_m^{N-1} , and $\left\langle \phi_f^k | H_{\text{int}} | \phi_i^k \right\rangle \equiv M_{f,i}^k$ is the one-electron dipole matrix element, and $\left\langle \Psi_m^{N-1} | \Psi_i^{N-1} \right\rangle$ is the

³Notice that when the photoelectrons with low kinetic energy, the emitted photoelectrons may need longer than the system response time to escape into vacuum. In this case the *sudden approximation* is not suitable and one should use the so-called *adiabatic limit*. In this situation, the $(N-1)$ -electron system can adiabatically reach its ground state before the photoelectron is detected, and all the spectral intensity goes into the ground state peak.

$(N-1)$ -electron overlap integral. The total photoemission intensity, $I(k, E_{kin}) = \sum_{f,i} w_{f,i}$ is proportional to

$$\sum_{f,i} |M_{f,i}^k|^2 \sum_m |c_{m,i}|^2 \delta(E_{kin} + E_m^{N-1} - E_i^N - h\nu) \quad (3.14)$$

where $|c_{m,i}|^2 = \left| \langle \Psi_m^{N-1} | \Psi_i^{N-1} \rangle \right|^2$ is the probability that the removal of an electron from the initial state i will leave the $(N-1)$ -particle system in the excited state m . For one particular state $m = m_0$, if $\Psi_i^{N-1} = \Psi_{m_0}^{N-1}$, the corresponding $|c_{m,i}|^2 = 1$, and all the other $|c_{m,i}|^2 = 0$; in this case, if $M_{f,i}^k \neq 0$, the ARPES spectra of the non-interacting systems can be expressed as a delta function with only one peak at $E_B^k = -\varepsilon_k$ (Fig. 3.8 (a)). This is the simple case of non-interacting electrons. In this case, Eq. 3.4 can be simplified as $w_{fi} \approx \frac{2\pi}{\hbar} \left| \langle \phi_f^k | H_{int} | \phi_i^k \rangle \right|^2$, which is the one-electron dipole matrix element. However, in strongly correlated systems many $|c_{m,i}|^2 \neq 0$ because the removal of the photoelectron results in a strong change of the systems effective potential and, in turn, Ψ_i^{N-1} will overlap with many of the eigenstates Ψ_m^{N-1} . Thus the ARPES spectra are not single delta functions any more but show a main line and several satellites according to the number of excited states m created in the process (Fig. 3.8 (c)).

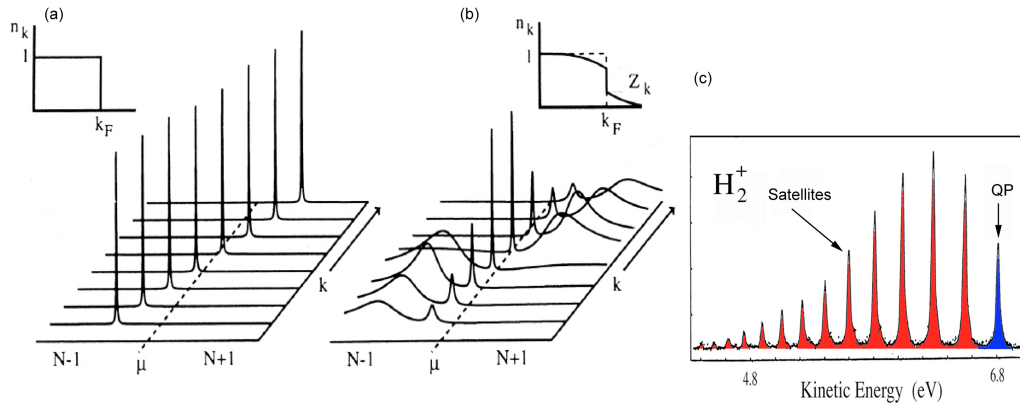


Figure 3.8: (a) Momentum resolved one-electron removal and addition spectra for a non-interacting electron system with a single energy band dispersing across Fermi edge. (b) The same spectra for an interacting electron system. (from Ref. [17]). (c) Photoelectron spectrum of gaseous hydrogen [30].

3.2.4 One-particle spectral function

The photocurrent $I(k, E)$ can be written, often an approximate manipulation of Eq. 3.13, as

$$I(\mathbf{k}, \omega) = I_0(\mathbf{k}, \nu, \omega) f(\omega) A(\mathbf{k}, \omega) \quad , \quad (3.15)$$

where $\mathbf{k} = \mathbf{k}_{\parallel}$ is the in plane electron momentum, ω is the electron energy with respect to the Fermi level, and $I_0(\mathbf{k}, \nu, \omega)$ is proportional to the square of the dipole transition matrix elements $|M_{f,i}^k|^2$, and it is energy, momentum, and light polarization dependent. $f(\omega)$ is the Fermi function, which accounts for the fact that direct photoemission probes only occupied

electronic states, and $A(\mathbf{k}, \omega)$ is the single particle spectral function, which embodies all the interactions of the electron in the solid [31]. In principle, an ARPES measurement gives access to the single particle spectral function $A(\mathbf{k}, E)$, although in practice the issue is complicated by several factors [17, 26, 32, 33]. In the non-interacting electron system, the spectral function $A(\mathbf{k}, \omega)$ is a simple Dirac's delta function at momentum k and corresponding energy ε_k . Many-body effects modify the properties of a real system, and produce changes in the one-particle spectral function. In an interacting electron system, it is customary to consider the effects of interactions in the self-energy $\Sigma(\mathbf{k}, \omega)$. Its real and imaginary parts contain all the information on the energy renormalization and lifetime, respectively, of an electron with band energy ε_k and momentum k propagating in a many-body system. Thus the self-energy leads to a more complex spectral function as

$$A(\mathbf{k}, \omega) = -\frac{1}{\pi} \frac{\text{Im} \Sigma(\mathbf{k}, \omega)}{[\omega - \varepsilon_{\mathbf{k}} - \text{Re} \Sigma(\mathbf{k}, \omega)]^2 + [\text{Im} \Sigma(\mathbf{k}, \omega)]^2}. \quad (3.16)$$

3.2.5 Extracting the real and imaginary parts of the self-energy

Figure 3.9 shows the ARPES intensity map from optimally doped Bi2223 along (0,0) to (π, π) . The dark color represents the spectrum at nodal region near the Fermi level. The quasiparticle dispersion can be clearly followed up to the Fermi crossing. One can see a break in the dispersion at around $E_B = 70$ meV which is related to a sudden change of effective mass. The kink is usually attributed to the effect of the dressing of the QP by low energy excitations. Quantitative analysis is done by using energy distribution curves (EDC) and momentum distribution curve (MDC), as marked in Fig. 3.9. Energy scans at constant momentum defines EDC and momentum scans at constant energy determines MDC. Figure 3.9 also illustrates the procedure for extracting the real and imaginary parts of the electron self-energy (for details see Ref.[34]). The red curve is the MDC at certain energy ω , and the blue open circles represent the band dispersion or the positions of MDC maxima taken at different constant energy ω . The black dashed line shows the interpolated bare band dispersion ε_k (without dressing). \mathbf{k}_1 and \mathbf{k}_2 are the momenta where the MDC reaches its half maximum. Then, as illustrated in the figure, the real part of the self-energy is $\text{Re} \Sigma(\omega) = \omega - \varepsilon_{\mathbf{k}_m}$ is the difference between the experimental band dispersion and the bare band dispersion. The imaginary part is given by [34]

$$\left| \text{Im} \Sigma(\omega) \right| = \varepsilon_{\mathbf{k}_2} - \varepsilon_{\mathbf{k}_m} = \varepsilon_{\mathbf{k}_m} - \varepsilon_{\mathbf{k}_1} = \frac{\varepsilon_{\mathbf{k}_2} - \varepsilon_{\mathbf{k}_1}}{2} \quad (3.17)$$

The real part of the self-energy gives the information of the renormalization of the bare band, that is the strength of the kink. The Lorentzian broadening of the spectral function is cause

by the imaginary part of the self-energy which presents the lifetime of the quasiparticles, or the scattering rate. Here the interactions other than the electron-phonon coupling have been neglected. But in other cases, it is remarkable to consider all kinds of interactions, such as electron-electron, electron-magnon, electron-plasmon and electron-impurity scattering into the self-energy. In the following chapters I will discuss the kink behavior in CDWs and HTSCs systems in detail.

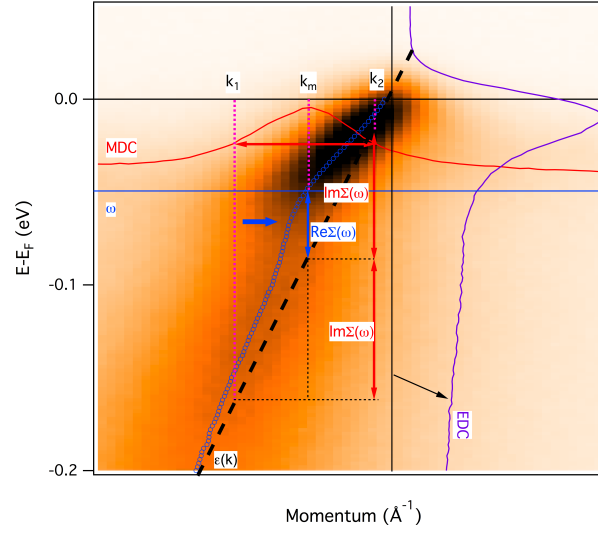


Figure 3.9: Real and imaginary parts of the self-energy (shown in blue and red double headed arrows, respectively) on the ARPES intensity map near the nodal region. The blue open circle line is the maxima of MCD at each constant energy position, and the black dashed line is the bare band dispersion. Red solid line is the MDC at a certain binding energy. The figure is referred to Ref.[34].

Chapter 4

Transition metal dichalcogenides

4.1 Introduction to transition metal dichalcogenides

4.1.1 Crystallographic and electronic structure

In the past several decades the layered transition metal dichalcogenides (TMDs) have raised much attention because of their unique crystal structure and complex electronic properties [35]. The general formula of TMDs is TX_2 , where T stands for a transition metal (usually Ta, Ti or Nb) and X for a chalcogen (S, Se and Te). These layered materials have a sandwich structure with one sheet of transition metal atoms in a hexagonal pattern surrounded on adjacent sides by two similar chalcogen sheets. The bonds within the sandwich are covalent, while bonding between the adjacent sandwiches is due to weak van der Waals forces. There are different possible arrangements for the relative position of the TX_2 sandwiches in the lattice along the c axis. The two most common types of TX_2 sandwiches, with the transition metal in either octahedral or trigonal prismatic coordination by the chalcogens (Fig. 4.1), correspond to the 1T and 2H polytypes. There are several other possibilities for stacking the sandwiches, depending on the relative placement of the layers, referred as 1T, 2H, 3R, 4H_a , 4H_b . The first number in this notation refers the number of sandwiches in the unit cell, while T, H and R distinguish the trigonal, hexagonal and rhombohedral symmetry of the structure. Sometimes a subscript is required to further distinguish similar polytypes.

Since the interaction between adjacent sandwiches is weak, the electronic properties of these layered compounds are mainly determined by the structure inside the sandwich. Another very important aspect is the symmetry of the structure. For example, the simplest polytype is 1T-TaS₂ (Fig.4.1 (a)), with Ta atoms in octahedral coordination, exhibits metallic behavior at room temperature (RT), but an increasing resistivity at low temperature. On the other hand, the 2H polytype with the Ta atom in a trigonal prismatic coordination (Fig.4.1 (b)), is a metal both at RT and at low temperature, and even shows superconductivity at very low temperature

(below 10 K).

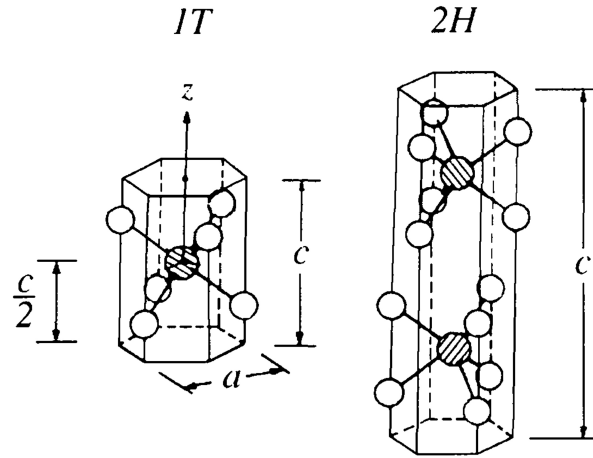


Figure 4.1: Schematic showing the unit cell of the 1T and 2H polytype TMDs [6].

The TMDs present a nature cleavage plane at the van der Waals gap due to the weak interactions. Therefore, it is rather easy to cleave the crystal in UHV to expose a clean mirrorlike high quality surface. The cleaved TMDs show very large atomically flat surfaces and are relatively stable, and therefore likely to remain clean for long time under UHV conditions, which is quite suitable for photoemission study. The Brillouin zone (BZ) of the 1T and 2H polytypes are hexagonal prisms (Fig. 4.2).

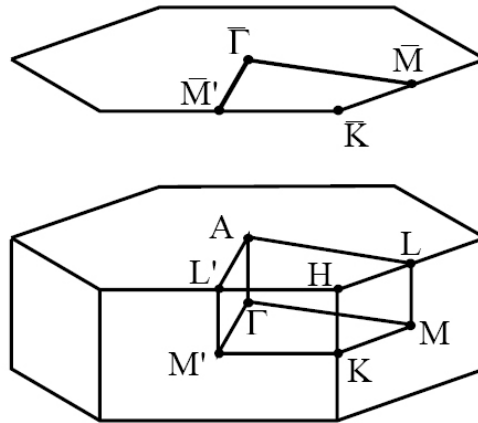


Figure 4.2: BZ and surface Brillouin zone (SBZ) with symmetry points.

Both 1T-TaS₂ and 2H-TaS₂, which are considered in this chapter, are typical charge-density-wave (CDW) systems. In the past several decades, both of them have been well studied, but the driving force for the CDW modulation and the competition with other broken symmetry states (for example, superconductivity and Mott insulating states) are still not fully understood. 1T-

TaS₂ exhibits a strong CDW modulation but with no superconductivity. By contrast, the CDW in 2H-TaS₂ is weak and can be interpreted in terms of weak-coupling scenarios, such as the Fermi surface nesting, saddle point, or Fermi patch scenarios. In the following I will try to address these issues.

4.2 1T-TaS₂

1T-TaS₂ is an exception among the TMDs, because it shows drastic deviations from the one electron band picture. The origin of that behavior may be the particularly large CDW amplitude compared to other TMDs, as well as the presence of electron correlation effects of the Mott-Hubbard type. The compound shows a succession of CDW phases, and the electrical resistivity bears the signatures of the transitions between the various phases (shown in Fig. 4.3): a metallic phase at high temperature, an incommensurate (IC) CDW phase below 550 K, a nearly commensurate (NC) CDW below 350 K, and an insulating commensurate (C) CDW phase below 180 K.

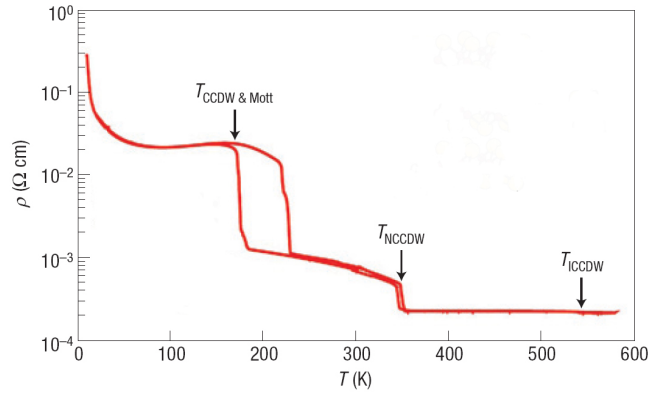


Figure 4.3: Temperature dependence of the electric resistivity of 1T-TaS₂. Taken from [36].

Incommensurate charge-density-wave phase

The first change of the electric resistivity occurs below 550 K (Fig. 4.3). In this phase the ratio between IC-CDW wavelength and the lattice parameter is $a_{IC-CDW}/a_0 \sim 3.35$, incommensurate. The IC-CDW is a homogenous long-range ordered CDW state, with metallic behavior. Figure 4.4 shows momentum integrated valence band photoemission spectra above and below the IC-NC CDW transition. Across this critical transition temperature a clear decrease of the photoemission intensity at the Fermi level indicates a reduction of the electronic DOS, which is in good agreement with the stepwise increase of the electrical resistivity and with the expected partial gapping of the Fermi surface by the CDW (Fig. 4.3).

Nearly-commensurate and commensurate charge-density-wave phases

Below 350 K the electron density of 1T-TaS₂ undergoes the second modulation. The IC-CDW phase is replaced by a new phase characterized by a hexagonal array of commensurate domains [37, 38]. Furthermore, the domain size which is characterized by the number of C CDW maxima per domain increases when the temperature decreases in the NC-CDW phase [38], as shown in Fig. 4.5. This corresponds to an increasing electrical resistivity.

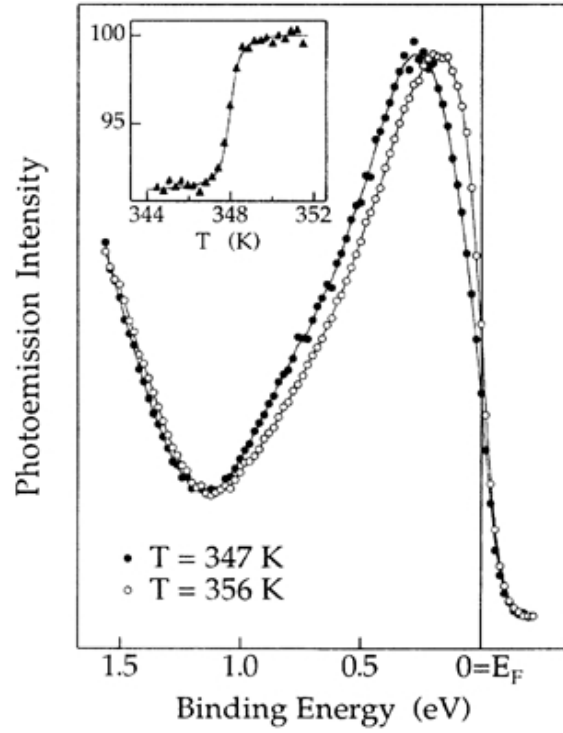


Figure 4.4: Momentum-integrated photoemission spectra just above and just below T_{IC-NC} . A clear Fermi edge, with finite electron density at the Fermi level, can be seen. The inset shows the photoemission intensity as a function of temperature in arbitrary units at 180 meV. Data is taken from [39].

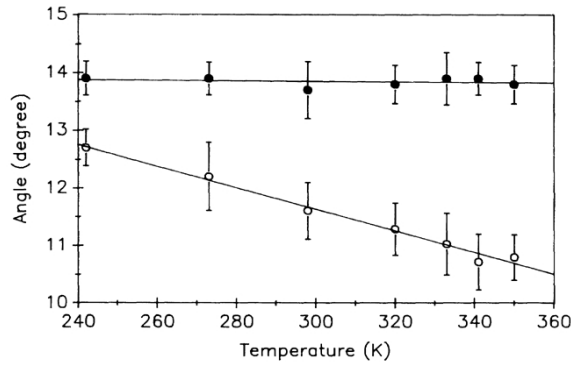


Figure 4.5: The CDW domain size vs. temperature in the NC-CDW state of 1T-TaS₂. Data taken from [38].

At lower temperature ~ 180 K, long range C-CDW order is suddenly achieved, and the resistivity exhibits a tenfold jump. Figure 4.6 (data from [40]) shows ARPES spectra at the Fermi surface of 1T-TaS₂ around the NC to C-CDW phase transition. The 191 K spectrum is typical of the NC-CDW phase, while the 186 K one is the characteristic of the low temperature C-CDW phase. Clearly, at the NC-C transition, spectral weight is removed from the Fermi energy, and piled-up at finite binding energy, reflecting a metal to non-metal transition.

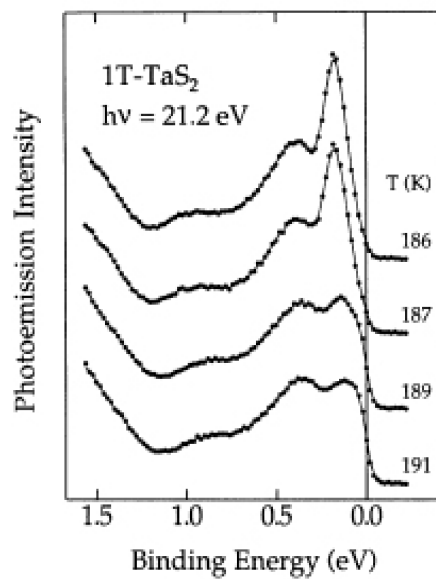


Figure 4.6: ARPES spectra of 1T-TaS₂ at the NC-C phase transition. Data is taken from [40].

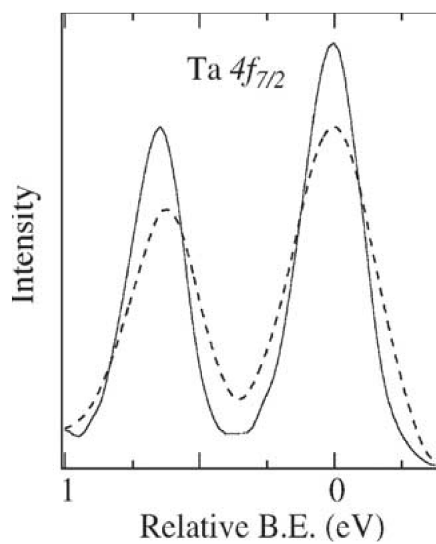


Figure 4.7: Ta 4f_{7/2} core levels of 1T-TaSe₂ in the C (solid line) and NC-CDW (dashed) phases. Data is taken from [41].

Another way to evaluate the temperature dependence of the CDW is through the line shape

of Ta $4f$ core levels, which act as local probes of the electron density at the inequivalent Ta sites [42]. In the similar compound 1T-TaSe₂, the splitting of the Ta $4f_{7/2}$ spin-orbit component into two peaks (Fig. 4.7) is larger and better defined in the C-CDW than in the NC-CDW phase.

The C-CDW phase is the simplest among the different CDW phases in 1T-TaS₂. As mentioned in Chap. 2, the CDW is always accompanied by a periodic lattice distortion (PLD) and leads to a superstructure. In the C-CDW phase, 1T-TaS₂ develops a $\sqrt{13} \times \sqrt{13}R13.89^\circ$ superstructure. Its building blocks in the Ta plane are 13-atoms “star of David” clusters, as illustrated in Fig. 4.8. In the real space a star array around a fixed Ta site A is evident. The nearest neighbor (NN) atoms B and the next nearest neighbor (NNN) Ta atoms C move towards the star center. However, this deformation does not fully gap the FS, with only the outer NN and NNN twelve electrons occupying the electronic states below the gap. The “thirteenth” electron occupies a half filled d band which straddles the Fermi level as illustrated in Fig. 4.9 (a), which is the situation in NC phase. It is important to notice here the synergy of CDW and Coulomb interaction. To yield a Mott transition, the on-site Coulomb repulsion U should be larger than the band width W . In the NC-CDW phase U is smaller than the Ta bandwidth W , and no Mott transitions occurs. In the C-CDW phase, the Ta d band splits into three subbands (Fig. 4.9 (b)). These subbands are clearly resolved in the C-CDW phase, while they overlap in the NC phase as a consequence of the limited size of the C domains. Since $U > W$, at the NC-C transition a metal-insulator Mott transition (See Chap. 2) takes place and the half filled band splits into upper and lower Hubbard subbands, separated by the Coulomb interaction energy U . This Mott-Hubbard gap will be further confirmed by photoemission data in the following section.

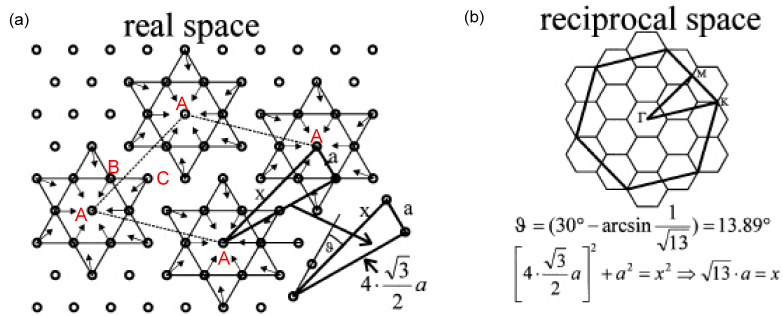


Figure 4.8: (a) $\sqrt{13} \times \sqrt{13}$ superstructure of 1T-TaS₂ from the “star of David” mode in real space. The open circles are Ta atoms. (b) The same but in reciprocal space. Notice that the $\sqrt{13} \times \sqrt{13}$ cell is rotated by 13.89° with respect to the undistorted unit cell [43].

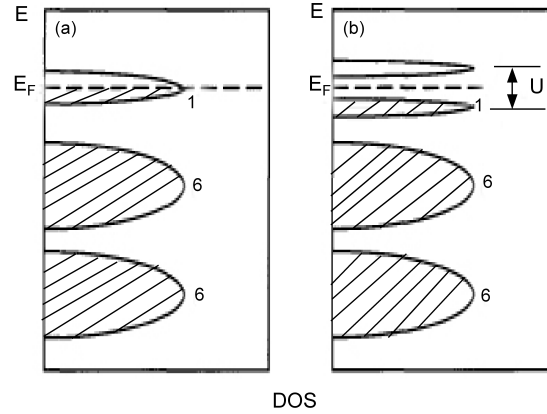


Figure 4.9: Schematic density of states for the Ta d band in the (a) nearly-commensurate and (b) commensurate CDW phases. The splitting into three subbands of the d band is due to superlattice potential associated with the CDW/PLD. A metal-insulator Mott transition occurs in the C CDW phase, and a correlation gap opens near the Fermi edge. The numbers refer to the number of electrons per subband.

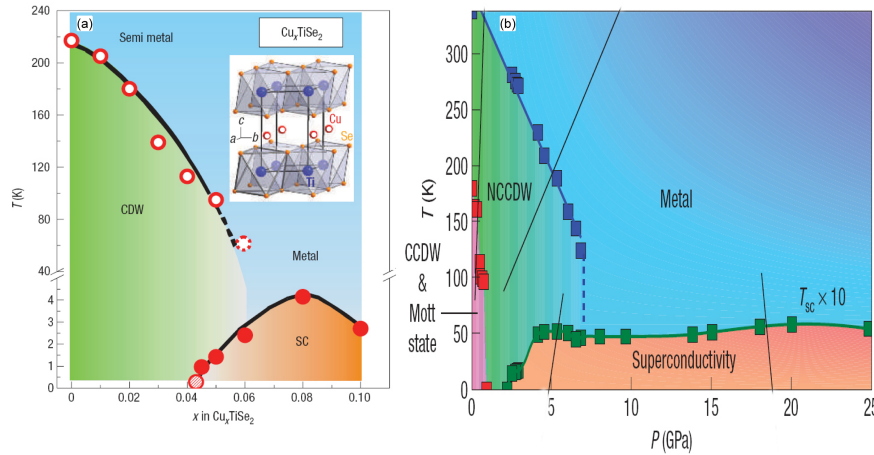


Figure 4.10: The coexistence and competition of CDW and SC in 1T polytype TMDs. (a) Temperature-composition phase diagram of 1T- Cu_xTiSe_2 . (b) Temperature-pressure phase diagram of 1T- TaS_2 .

4.2.1 Superconductivity coexists and competes with CDW in 1T-TMDs

Superconductivity (SC) and the CDW state are two very different cooperative electronic states. At low temperature, it is a widely held belief that the two broken symmetry states compete. Both states are the result of strong electron-phonon coupling acting – in general – on the electronic states of the same Fermi surface. The competition of various instabilities often encountered in interesting materials is an important topic of condensed-matter physics. SC

usually is found in the 2H polytype TMDs (which I will discuss in detail in section 4.4). However, recently Morosan *et al.* [44] have reported the coexistence and competition of CDW and SC in Cu-intercalated 1T-TiSe₂, as shown in the temperature-intercalation phase diagram in Fig. 4.10 (a). SC also emerges under pressure in 1T-TaS₂, while the CDW phase is suppressed and eventually disappears, as illustrated in the temperature-pressure phase diagram of Fig. 4.10 (b) [36]. In the present work, I also found a similar coexistence of CDW and SC in the presence of a strong CDW in 1T-TaS₂ when a small amount of disorder is added to the system. In the following I will discuss and explore the electronic properties of that system.

4.2.2 Occurrence of superconductivity when the metal-insulator transition is inhibited in 1T-TaS₂ (Phys. Rev. B 81 172503 (2010))

When a Mott metal-insulator transition is inhibited by a small amount of disorder in the layered dichalcogenide 1T-TaS₂, an inhomogeneous superconducting state arises below $T=2.1$ K, and coexists with a nearly-commensurate charge-density-wave. By angle-resolved photoelectron spectroscopy (ARPES) we show that it emerges from a bad metal state with strongly damped quasiparticles. Superconductivity is almost entirely suppressed by an external magnetic field of 0.1 T.

One of the most intriguing phenomena in the solid state is the occurrence of electronic instabilities towards broken symmetry states, like superconductivity (SC), density-waves, charge and orbital order, or the Mott insulating state. When two or more instabilities are simultaneously at work, complex phase diagrams and unusual physical properties are found. Understanding such a coexistence or competition is therefore important. A related open issue is the emergence of SC from a normal state where the nature of the quasiparticles (QPs) is strongly modified by the interactions. Spectroscopic probes of the electronic states with momentum selectivity, namely angle-resolved photoelectron spectroscopy (ARPES) can address these issues.

Broken-symmetry phases are especially prominent in low-dimensional – quasi one-dimensional (1D) and quasi-two-dimensional (2D) – materials [3]. The 2D transition metal dichalcogenides (TMDs) in particular, exhibit a variety of charge-density-waves (CDW) transitions [35]. In their trigonal prismatic (2H) polytypes some of them also support SC, with critical temperatures as high as 7.2 K for NbSe₂. ARPES has been used to identify in the band structure the favorable conditions for electronic instabilities [45, 46, 47, 48]. According to the simplest Peierls scenario, the CDW is the result of a moderately strong electron-phonon ($e-ph$) interaction connecting electron and hole states across the well-nested Fermi surface (FS). SC is also a consequence of $e-ph$ coupling, leading to the formation of Cooper pairs at the FS. Even if alternative scenarios been proposed which do not rely on nesting [49, 50], both CDW and SC tend to gap parts of the same FS, and are generally considered to be competing.

SC is usually not found in TMDs of the 1T polytype, with TM ions in octahedral coordination, but it can be induced by doping or by external pressure. Recently, much interest has been raised by the observation that the balance between CDW and SC can be continuously tuned in the TMD TiSe_2 by a controlled intercalation of Cu atoms [44]. Here we consider the occurrence of SC in the isostructural TMD $1T\text{-TaS}_2$, which exhibits a unique sequence of CDW and Mott phases, as a result of the interplay of $e\text{-}ph$ and Coulomb interactions [35]. At room temperature (RT) the CDW is nearly-commensurate (NC). It consists of an hexagonal array of domains separated by domain walls (discommensurations) where the CDW phase changes rapidly. The domain size and the CDW amplitude grow as temperature is reduced, down to $T_{MI} \sim 180$ K, where an insulating commensurate (C) $(\sqrt{13} \times \sqrt{13})R$ 13.9° CDW phase is suddenly established. In real space the Mott metal-insulator (MI) transition corresponds to the localization of one Ta $5d$ electron at the center of the 13-atom ‘star of David’ cluster unit of the CDW. In reciprocal space, it is due to the opening of a correlation gap in a narrow half-filled band straddling the Fermi level [51]. Sipos *et al.* [36] have shown that the application of external pressure suppresses the Mott transition, and that SC appears above 2.5 GPa. Here we show that, in the presence of a very small amount of disorder which also suppresses the Mott transition, SC arises at ambient pressure below $T = 2.1$ K. We have probed the electronic structure by ARPES, and found that SC emerges from a normal state where strongly damped quasiparticles bear the spectral signatures of the underlying CDW and of the incipient Mott transition.

It is known that tiny amounts of disorder – induced e.g. by irradiation or non-stoichiometry – suppress the MI transition in $1T\text{-TaS}_2$ [52, 53, 54]. We have taken the systematic approach of producing samples with variable amounts of Cu intercalated between the TaS_2 planes, by adding CuCl_2 during the crystal growth by chemical-vapor transport. Here we report data for samples with a Cu content at the detection limit ($< 0.1\%$), for which the particular growth conditions yielded a small Ta deficiency and possibly a small amount of structural disorder. The stoichiometry was $\text{Ta}_{1-x}\text{S}_2$ with $x = 0.015$, as determined by fluorescence microanalysis. X-ray diffraction yielded a c -axis lattice parameter (5.90 \AA) identical to that of pure TaS_2 . In the following, we will refer to these samples as $d\text{-TaS}_2$. The in-plane electrical resistivity was measured by the four-probe method between 0.35 K and RT. The magnetic susceptibility was measured along the c -axis in a 0.29 Oe field oscillating at 546 Hz. To achieve a signal from the $< 100 \mu\text{m}$ thin sample, five 1.6 mm^2 pieces were stacked 1.5 mm apart, fixed with GE varnish into shelves cut in a carbon fibre rod, thus allowing an expelled field volume from the Meissner effect in excess of the sample volume itself. For ARPES and low-energy electron diffraction (LEED) the crystals were post-cleaved *in situ* to obtain mirror-like surfaces. We performed ARPES and core-level photoemission measurements with a SPECS PHOIBOS 150 hemispherical analyzer and a high-brightness monochromatized GAMMADATA He lamp

($h\nu=21.2$ eV, 48.4 eV). The energy and momentum resolution were respectively 10 meV and $\pm 0.01 \text{ \AA}^{-1}$. The Fermi level position was determined with an accuracy of ± 1 meV by measuring the metallic cutoff of a polycrystalline Ag film.

The in-plane electrical resistivity of d -TaS₂, shown in Fig. 4.11a, increases with decreasing temperature between 300 K and ~ 20 K. The sharp jump at T_{MI} and the large hysteresis present in the pristine material (TaS₂ in short) are completely suppressed in d -TaS₂. However, above T_{MI} the two curves are indistinguishable, indicating a minimally perturbed sample. In this temperature range LEED measurements show the coexistence of two equivalent domains corresponding to the NC CDW, rotated in opposite directions. In our experience, cleaved surfaces of pristine 1T-TaS₂ generally yield single-domain patterns. The overall temperature dependence is similar to that of other doped or disordered TaS₂ crystals [52, 53, 54]. Rather unexpectedly, the resistivity turns over below ~ 15 K and presents a sharp drop at 2.1 K (Fig. 4.11b), suggesting the onset of superconductivity. The finite residual resistance at 350 mK indicates that superconductivity occurs in spatially separated minority regions, which do not percolate through the material.

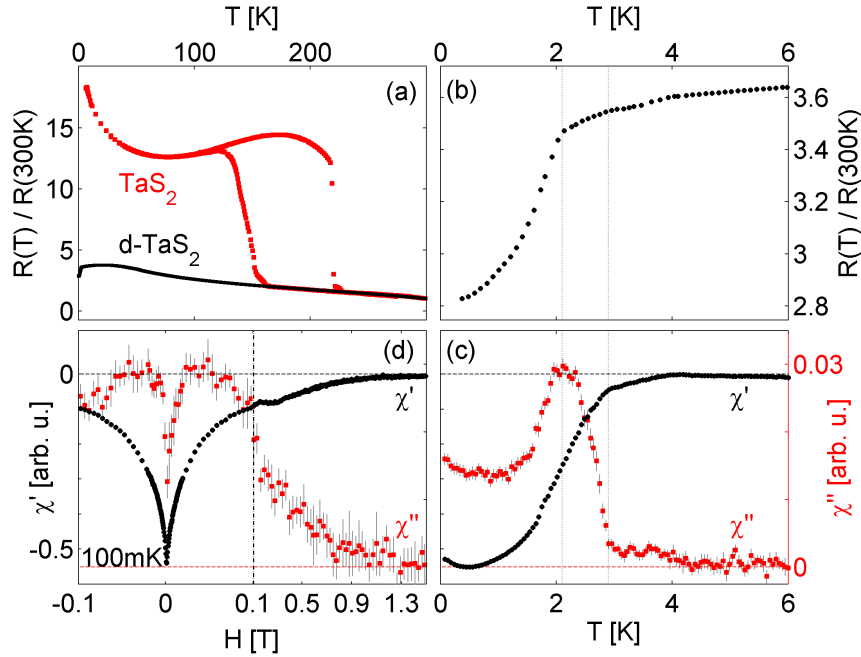


Figure 4.11: (color online) In-plane electrical resistivity and c -axis magnetic susceptibility of d -TaS₂. (a) The resistivity is indistinguishable down to the MI transition at 180-220 K, which is seen in pure TaS₂ (red squares) but completely absent in d -TaS₂ (black circles). (b) The low-temperature part shows a sudden drop in resistivity below 2.1 K, suggesting onset of superconductivity. (c) Temperature dependence of real χ' (black circles) and imaginary χ'' (red squares) components of the AC-susceptibility measured in zero field. (d) Field dependence of χ at 100 mK.

Indeed, the occurrence of superconductivity is confirmed by the magnetic susceptibility

(Fig. 4.11c). The real part χ' becomes negative due to the Meissner effect. The imaginary (dissipative) part χ'' displays a broad peak similar to the behavior observed in granular superconductors. In granular superconductors, the dissipation is linked to junctions between superconducting grains. We speculate that the dissipation in our samples stem from the junctions between superconducting droplets. Such droplets could likely be nucleated by the CDW domain structure. The onset of changes in both χ' and χ'' is at 2.9 K, with the peak in the imaginary part coinciding with the drop in resistivity at 2.1 K. Susceptibility shows that separate superconducting regions form below 2.9 K, and phase coherence between them begins at 2.1 K, but does not lead to percolation. This picture is supported by the weakness of the Meissner effect testifying a reduced superconducting volume fraction $v = (V_{sc}/V)$, and is consistent with the field dependence, where an external field of < 0.1 T suppresses most the Meissner effect, but a portion corresponding to the 2.1-2.9 K signal persist up to 1 T (Fig. 4.11d). Our non-standard set-up prevents a direct, quantitative determination of v from χ' , but an estimate is possible from the resistivity jump at the transition. A simple 2D model based on an effective medium approximation, which neglects the smaller conductivity along the c axis, yields $v/v_c = (\Delta R/R)$, where $v_c = 0.676$ is the critical value for percolation. In our case we obtain $v = 0.15$, well below the percolation limit.

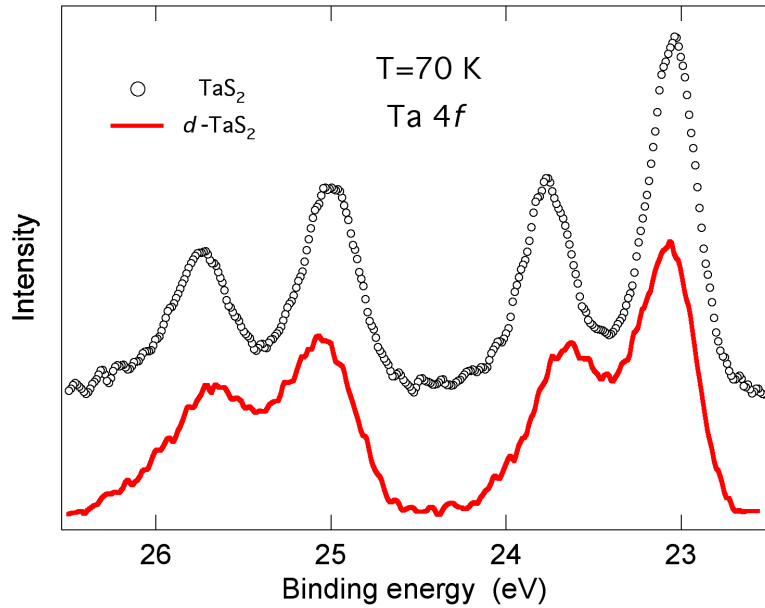


Figure 4.12: (color online) Ta 4*f* core level spectra ($h\nu=48.4$ eV, HeII β line) measured at $T=70$ K. The broadening and splitting of the line shapes reflects inequivalent Ta sites in the CDW state.

Photoemission core level spectra provide an independent local probe of the CDW state [55, 56]. In the presence of a spatial charge modulation, inequivalent Ta atoms experience different local potentials – corresponding to charge accumulation or depletion – which translates into

differences in the kinetic energies of the photoelectrons. The intrinsic energy width of the shallow Ta 4*f* core levels is small enough that the resulting spectral broadening or splitting can be easily determined. Figure 4.12 illustrates the Ta 4*f* spin-orbit doublet of TaS₂ and of *d*-TaS₂, measured at the same temperature $T=70$ K. The spectrum of TaS₂ is consistent with literature data for the C phase. Both spin-orbit partners are clearly split, according to the 6:6:1 distribution of inequivalent sites within the 13-atom cluster. For *d*-TaS₂ the splitting is smaller, and the individual components cannot be resolved. This is characteristic of the NC phase at $T > T_{MI}$, reflecting a CDW amplitude and charge inhomogeneity smaller than in the C phase, and the contribution from domain boundaries. The core level data confirm microscopically that the electronic charge distribution of *d*-TaS₂ is different from that of the pristine sample at the same temperature even if, within the domains, the two configurations are quite similar.

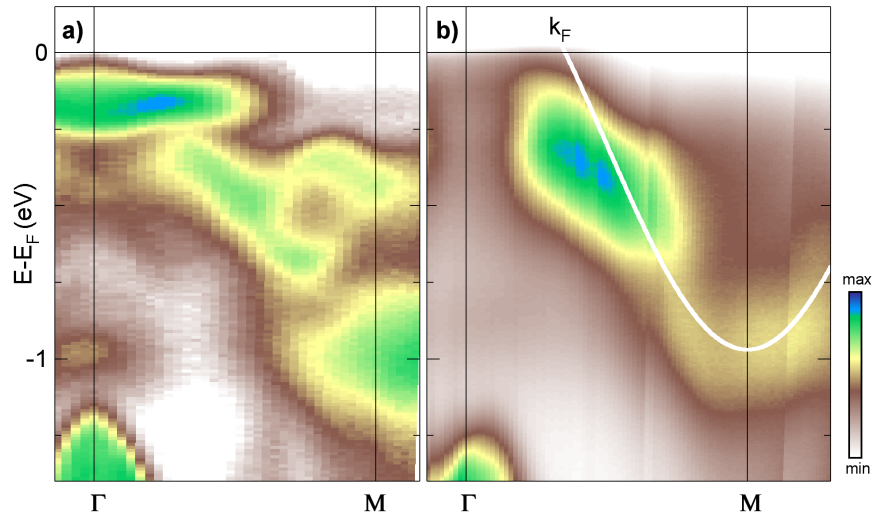


Figure 4.13: (color online) HeI ($h\nu=21.2$ eV) ARPES intensity maps of (a) TaS₂ and (b) *d*-TaS₂ measured at 70 K along the high symmetry ΓM direction. The continuous line reproduces a tight-binding band for the unreconstructed structure from Ref. [57], and is a guide to the eye.

Figure 4.13 (a) and (b) shows energy-wave vector ARPES intensity maps of TaS₂ and *d*-TaS₂ measured at 70 K along the high symmetry ΓM direction ($\overline{\Gamma M}=1.08 \text{ \AA}^{-1}$) of the hexagonal Brillouin zone (BZ). The top of the S 3*p* band is visible at -1.3 eV around Γ . The Ta 5*d* conduction band disperses upwards from the M point. It is rather diffuse in *d*-TaS₂, and the map shows no clear Fermi level crossing, but a constant-energy cut – a momentum distribution curve – at $E=E_F$ (not shown) yields a Fermi wave vector $k_F=0.27 \overline{\Gamma M}$. Overlaid on the map as a guide to the eye is the result of a tight-binding (TB) calculation for the undistorted structure [57]. The superlattice potential splits this band into three separate manifolds. Two of them, centered at -1 eV and -0.6 eV, are fully occupied. A third half-filled band straddling E_F is further split at T_{MI} with the opening of a correlation gap between an occupied lower

Hubbard band (LHB) at -0.2 eV and an unoccupied upper band above E_F [58, 59, 60, 61]. Clearly the three CDW subbands are not well defined for d -TaS₂ but the incipient CDW-induced splitting is revealed by strong deviations from the TB dispersion. This is again typical of the NC phase, where free electrons from the discommensurations can provide enough screening to prevent the Mott transition within the locally commensurate CDW islands. The finite size of the domains, and the superposition of two distinct orientations shown by LEED, contribute to the broad spectral weight distribution.

The effect of disorder on the electronic states is further illustrated in Fig. 4.14(a) by a comparison of ARPES data measured at $k=k_F$ and $T=70$ K. The spectra have been normalized to the same integrated intensity over the whole Ta 5d bandwidth, within 1.2 eV of E_F . The line shape of TaS₂, typical of the insulating C-CDW phase, is dominated by a sharp LHB feature at -0.18 eV and has vanishing intensity at E_F . The shoulder at -0.4 eV is due to the CDW subband. By contrast, the LHB structure is absent in d -TaS₂. The line shape is not gapped, and exhibits a metallic edge at E_F .

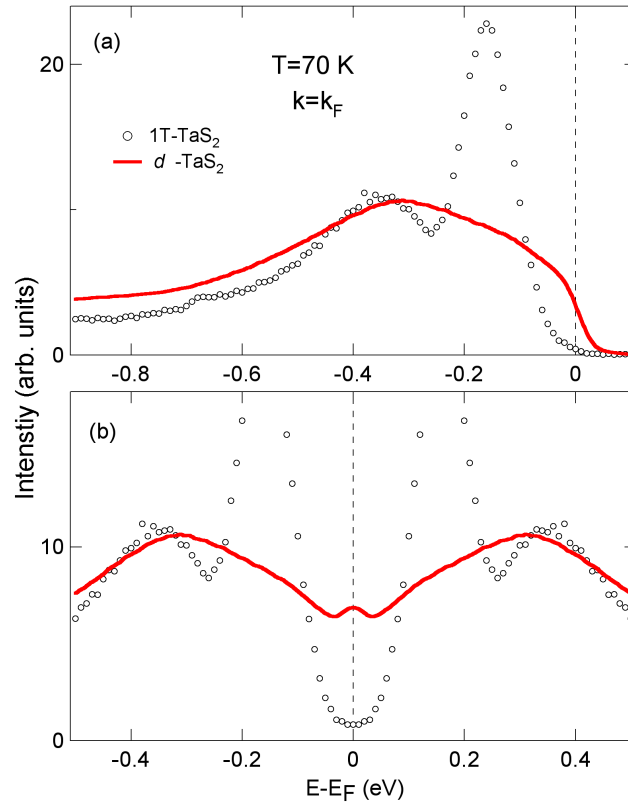


Figure 4.14: (color online) (a) Energy distribution curves measured at $k=k_F$ and 70 K from pristine 1T-TaS₂ and d -TaS₂. The same spectra are shown in (b), after a symmetrization around E_F .

The Fermi cut-off hampers a detailed analysis of the spectral function underlying the ARPES data of Fig. 4.14 (a). It can be removed by a symmetrization of the spectra around E_F :

$I^*(k_F, E) = I(k_F, E) + I(k_F, -E)$. Sufficiently close to E_F the symmetrized spectra shown in Fig. 4.14 (b) are proportional to the spectral function $A(k_F, E)$, since for the Fermi function $f(E, T) = (1 - f(-E, T))$, and electron-hole symmetry requires $A(k_F, E) = A(k_F, -E)$. The line shape of TaS₂ is that expected for a Mott insulator. Spectral weight is piled up in the Hubbard subbands, separated by a correlation gap, or possibly by a deep pseudogap [62]. Further away from E_F the loss of electron-hole symmetry may influence the line shape of the upper Hubbard band, but this is irrelevant for the following discussion. The picture of *d*-TaS₂ which emerges from Fig. 4.14 (b) is qualitatively different. $A(k_F, E)$ exhibits a weak coherent QP peak at E_F . Spectral weight is removed from E_F and placed in the broad incoherent sidebands. Elsewhere we have presented ARPES data showing the temperature-dependent spectral changes across a Mott transition in the isostructural TMD TaSe₂ [9]. The spectrum of *d*-TaS₂ closely resembles that of TaSe₂ in the metallic side just above the transition. Clearly *d*-TaS₂ is on the verge of opening a gap. The broad, intense, sidebands show that the QPs are strongly renormalized both by *e-ph* and Coulomb interactions.

The electronic properties of TaS₂ are complex, due to coexisting interactions and comparable energy scales. The dominant instability is the CDW. At first sight, the Coulomb interaction should be unimportant, since the ratio $\alpha = (U/W)$ between the Coulomb correlation energy (~ 0.4 eV from Fig. 4.14 (b)) and the conduction bandwidth (~ 1 eV) is small. In the CDW state, however, the relevant bandwidth is that of the narrower, partly occupied subband at E_F . W decreases with temperature as the CDW amplitude increases, and the critical value α_c for the bandwidth-controlled Mott transition is eventually attained. This balance depends on material-specific parameters. In the case of TaSe₂ the bulk of the material remains metallic, but a subtle change of parameters yields $\alpha > \alpha_c$ and a MI transition at the surface. Disorder pins the CDW and prevents the formation of a coherent C phase in *d*-TaS₂. In the NC phase, $\alpha < \alpha_c$: the Coulomb interaction becomes irrelevant and the MI transition is suppressed.

Favored by the large *e-ph* coupling, a SC state can eventually develop in *d*-TaS₂. But what is the nature of the normal state? In the pristine material the sudden disappearance of the Fermi surface at T_{MI} explains the order-of-magnitude increase of the resistivity. *d*-TaS₂ retains a small but finite coherent spectral weight at E_F which seems to contradict the insulating-like resistivity. However, the electrical conduction is clearly limited by scattering by the NC domains, and the increasing resistivity most likely reflects the growing amplitude of the CDW.

A second question concerns the electronic states which pair and give rise to SC. Are these states also involved in the CDW, and eventually in the Mott instabilities? When SC in 1T-TaS₂ is induced by pressure, there are indications that it develops in regions that are spatially separated from the CDW domains [36]. With increasing pressure the undistorted regions grow at the expense of the commensurate CDW domains, and the critical temperature for SC grows as the CDW is suppressed. A similar scenario may also apply here, but one should

be aware of differences between the two physical situations. Pressure modifies the orbital overlap, and therefore the band structure. Disorder, on the other hand, only affects the long-range coherence, leaving the CDW essentially unchanged within the domains, which represent a majority of the sample volume. We also note that the separation of electronic states within and outside the domains is not so clear-cut. ARPES has shown that, even in the Mott phase, the LHB exhibits a finite (~ 70 meV) dispersion [63]. Therefore, the $5d$ orbital at the star center is not entirely localized, so that states close to the domain boundaries may hybridize with states of appropriate symmetry outside the domain, providing a connection between the two electron systems.

In summary, we have shown that superconductivity can emerge even in the presence of a strong charge-density-wave, when the Mott instability is suppressed in the 2D TMD $1T$ -TaS₂. ARPES measurements of the normal state show that the coherent weight of the quasiparticles is considerably reduced by the interactions, and that the system remains quite close to a metal-insulator instability. Future experiments will aim at establishing a quantitative relation between the superconducting fraction and the amount of disorder. They should namely provide an answer to the interesting question whether the percolation threshold can be reached before disorder-induced localization sets in.

This work has been supported by the Swiss NSF and by the MaNEP NCCR. We gratefully acknowledge D. Ariosa for his assistance with the x-ray diffraction measurements.

4.3 1T-TiS₂

Another 1T polytype compound is 1T-TiS₂. It is a semiconductor with a band gap of ~ 0.6 eV. When a small amount of excess Ti is present, it shows the behavior of a degenerate extrinsic semiconductor due to the additional electrons. The electronic band structure of TiS₂ has been studied experimentally by photoemission, inverse photoemission, optical spectra and other techniques, as well as theoretically. Several calculations of the band structure have been available, which yield different values for the fundamental gap, or even predict a metallic character. In the following, I will discuss the band structure of Nb doped TiS₂ as deduced from photoemission data.

4.3.1 The semimetal to semiconductor transition in 1T-TiS₂ induced by Nb doping studied by angle resolved photoemission spectroscopy (to be submitted to Phys. Rev. B)

Angle resolved photoemission spectroscopy (ARPES) and transport measurements experiments have been carried out to study the electronic properties of the niobium-doped compounds 1T-Nb_xTi_{1-x}S₂ ($x = 0$ to 0.05). The effects of Nb doping on the electronic properties of TiS₂ are analyzed and discussed. The undoped sample is a narrow band gap degenerated semiconductor which shows semi-metallic behavior and weak correlation effects. With Nb doping, the number of carriers increases but defects induced by Nb substitution cause the opening of a pseudogap at the Fermi level, E_F , and an increase in the resistivity, indicating that a semiconducting phase eventually develops in the 1T-TiS₂ doped system.

The layered transition metal dichalcogenides (TMDs), and their related substituted or intercalated compounds have been a subject of intense research during the past decades, namely because they provide an exceptional playground to test and study the different interactions in two dimensional systems. This family of compounds exhibits plenty of interesting phenomena. Namely, the electron-phonon coupling, which is rather strong in some of these materials, is responsible for charge density wave (CDW) instabilities and/or superconductivity (SC). It has been recently shown that upon controlled intercalation of TiSe₂ with copper (Cu_xTiSe₂) the CDW transition can be continuously suppressed and a novel superconducting state arises [44]. In relation to electron-electron interactions, TMDs materials should not be considered as strongly correlated materials, because the Coulomb interaction energy U is usually smaller than electronic bandwidths. However, the periodic lattice distortion in the CDW phases, as in 1T-TaS₂ or 1T-TaSe₂, and the associated super-periodic potential may split the conduction band into narrower subbands where the bandwidth may be comparable to the Coulomb energy. Electronic correlations may then become dominant and even lead to a Mott insulator

ground state [9]. Finally, to fully cover the range of interesting phenomena present in these 2D materials, and opposite to exotic phases, $1T$ - TiTe_2 exhibits a quasi-2D Fermi Liquid (FL) behavior [64], and it has been studied by angle resolved photoemission spectroscopy (ARPES) as a paradigmatic FL 2D-system.

In this context there is a lack of recent studies on $1T$ - TiS_2 and doped related compounds. These systems have received a lot of attention two decades ago mainly because of their significant practical interest in advanced batteries as electrode materials, but also because of their interesting electronic properties [65]. However, recent discoveries in doped TMDs, and the improvements carried out in the last years in techniques as high resolution ARPES offer us a new opportunity to get more insight into the electronic structure and the effects of doping. $1T$ - TiS_2 was the subject of both experimental and theoretical studies [66, 67, 68, 69, 70, 71, 72, 73, 74, 75]. One of the main issues was to determine whether TiS_2 is a semimetal or a semiconductor. Several band structure calculations [72, 73, 76] showed the existence of an indirect gap between the S $3p$ and Ti $3d$ bands. Earlier ARPES measurements confirmed the existence of a gap in the range of 0.2-0.3 eV [66, 67]. Small electron pockets at the Fermi level, around the M points, were also found in different studies, leading to a finite density of states at the Fermi level. It is now commonly agreed that the difficulty of growing single crystals with the exact stoichiometry often results in an excess of Ti intercalated atoms. This leads to a finite density of states at the Fermi Level coming from the partial occupation of the Ti $3d$ conduction band which, confers a metallic, or semi-metallic, behavior for the pure system. This was confirmed by earlier transport measurements [74].

The basic building blocks of $1T$ - TiS_2 , with a CdI_2 -like structure, are S-Ti-S sandwiched slabs, each slab consisting of an hexagonal sheet of transition metal Ti atoms between two similar sheets of chalcogen, S, atoms [77]. The strong bonds within each layer are of covalent character. The bonding between the adjacent slabs is weak and determined by Van der Waals forces. The physical properties of $1T$ - TiS_2 , and by extension, of other TMDs layered materials, can be modified in a controlled way, either by the intercalation of foreign atoms or molecules between the layers of the “host” material, or by the substitution of the transition metal atoms in the plane by foreign atoms. In the first case, foreign atoms are located within the Van der Waals gaps, in a virtually unchanged host lattice. Many of the changes occurring in TMDs may be understood in terms of charge transfer between the dopant and the host, and of the increased spacing between layers, which is necessary to accommodate the intercalated species. Alternatively, the physical properties of $1T$ - TiS_2 and TMD layered materials can be also be tuned by means of substitutional doping, i.e. the replacement by foreign atoms of transition metal atoms in the chalcogenide–transition metal–chalcogenide sheets. The physical properties may be tuned in such a way as to achieve semiconductor-to-metal transitions (or the opposite) or to turn a normal conductor into a superconductor [77, 78, 79].

While the intercalation of alkali metals, or 3d transition metals, into TiS₂ has been widely studied [69, 80, 81], there are only very few studies focused on the substitution of Ti atom by foreign species [82]. Here we report on the first high resolution ARPES and transport measurements study on the influence of Nb doping on 1T-TiS₂. Surprisingly, even if the carrier density increases with the Nb content, both transport and electronic band structure measurements reveal a metal-to-semiconductor transition with increasing Nb doping and decreasing temperature. The results provide a spectroscopic view on the effects of disorder on the electronic structure of a weakly-correlated two dimensional electron gas.

1T-Nb_xTi_{1-x}S₂ single crystals, with doping levels $x = 0, 0.01, 0.05, 0.1, 0.2$ and 0.3 , were prepared by the chemical vapor transport method in the form of plaquettes with the c -axis perpendicular to the surface. The in-plane electrical resistivity was measured by the four-probe method between 1.4 K and RT. Crystals were cleaved *in situ* to obtain mirror-like surfaces, and the quality of the surfaces was checked by low energy electron diffraction (LEED). ARPES measurements were performed with a SPECS PHOIBOS 150 hemispherical analyzer and a high-brightness and monochromatized GAMMADATA He lamp ($h\nu = 21.2$ eV). The energy and momentum resolution were respectively 30 meV and ± 0.01 Å⁻¹.

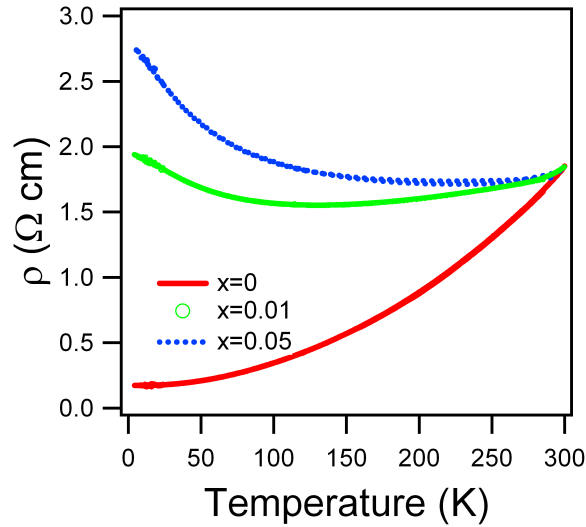


Figure 4.15: (color online) In-plane electrical resistivity of 1T-Nb_xTi_{1-x}S₂ with $x = 0$ (solid line), 0.01 (open circle) and 0.05 (dotted line), respectively.

The in-plane electrical resistivity of 1T-Nb_xTi_{1-x}S₂ ($x=0, 0.01, 0.05$), is shown in Fig. 4.15. The ρ -T curve of pristine TiS₂ ($x=0$) shows a rather unusual metal-like behavior ($d\rho/dT > 0$) in the whole temperature range investigated. By fitting the resistivity data with a power law, $[\rho(T) - \rho_0] \propto T^\gamma$, we obtain $\gamma=2.07$. This exponent is quite different from the low-T $\gamma=5$ exponent of a common metallic system. However it is in good agreement with previous

results from non-stoichiometric $1T$ -TiS₂ crystals. There, the unusual exponent was explained considering that both acoustic and optical phonons contribute to the resistivity [74].

The resistivity is markedly different in the doped compounds ($x = 0.01$ and $x = 0.05$). They exhibit a clear semiconductor-like behavior ($d\rho/dT < 0$) as the temperature decreases below a broad minimum around a characteristic temperature ($T^* = 130$ K and 225 K, for $x = 0.01$ and $x = 0.05$, respectively) even if they still show metallic behavior in the high temperature range. This behavior is quite different from metal-intercalated compounds M_x TiS₂, whose conductivity increases with x [83]. Instead, with increasing doping, the resistivity in $Nb_xTi_{1-x}S_2$ increases, suggesting that Nb atoms mainly substitute Ti atoms in the plane rather than being intercalated between layers. The resulting substitutional disorder in the conduction plane yields an increase in the resistivity.

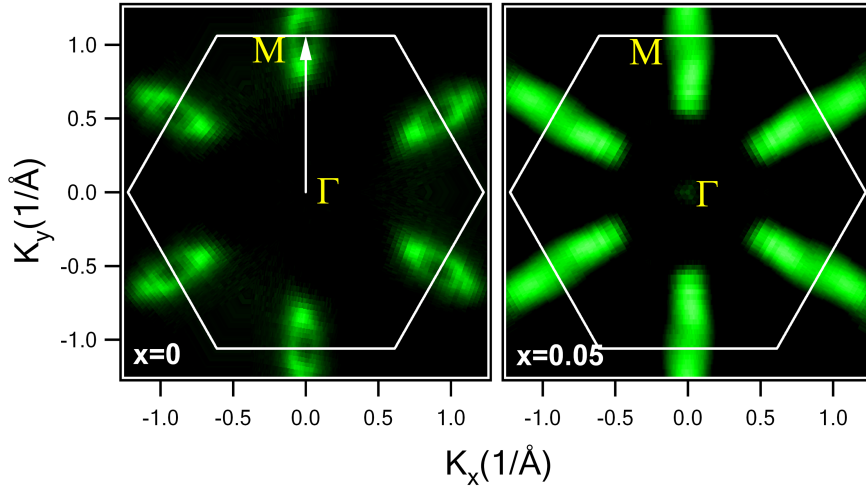


Figure 4.16: (color online) False color ARPES intensity maps integrated over ± 20 meV around the Fermi level for $1T$ - Nb_xTi_{1-x} with (a) $x = 0$ and (b) 0.05, respectively. The measured intensities were normalized to the photon flux. Electrons near the M point form a narrow pocket and generate a six-fold symmetric Fermi surface. The hexagonal SBZ is also shown.

The photoemission intensity maps at the Fermi level of pristine ($x = 0$) TiS₂ and of a Nb doped ($x = 0.05$) sample, measured at 70 K, are shown in Fig. 4.16. The ARPES intensity was integrated over an energy range of ± 20 meV around E_F and measured in the first quadrant, then symmetrized over the entire surface Brillouin Zone (SBZ). Opposite quadrants were also checked and found to be consistent with the symmetrization procedure except from intensity variations due to ARPES matrix elements effects. The FS maps exhibit a clear doping dependence. Strong spectral weight distributed around the M point forms narrow electron pockets, with an ellipsoidal ring shape, and six-fold symmetry. Upon doping, these pockets are expanded systematically towards Γ and the center of the second BZ. The oval ring shape at E_F becomes less defined and blurred, showing no clear E_F crossing points. A similar electron

pockets expansion was found in Cu doped TiSe₂ [79, 84]. In that system the density of states (DOS) at E_F increased with x , which was associated with the development of a superconducting state at low temperature. By contrast, in the present case, as it will be shown below, the DOS is considerably reduced with doping.

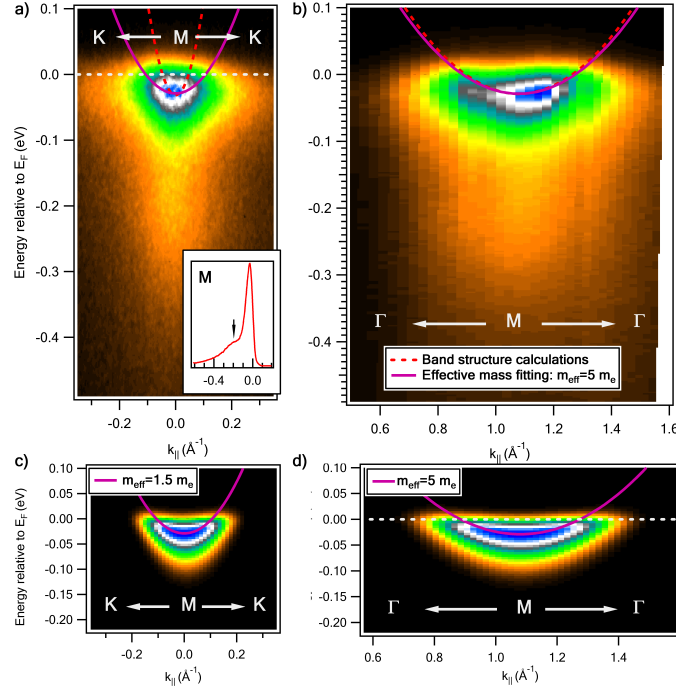


Figure 4.17: (color online) Electronic band structure of the electron pockets surrounding M for $x = 0$, along KMK (a), and Γ M (b). (c) and (d) panels show photoemission intensity simulations (see text for details). Red dashed lines indicate theoretical calculations [83] and purple solid lines the dispersion relation fit for m^* as indicated. The inset shows the photoemission spectrum at the M point, with an arrow indicating a satellite peak at -0.22 eV.

The ARPES intensity of the narrow M electron pockets along the KMK and Γ M high symmetry directions at $T = 70$ K, for $x = 0$, is displayed in Fig. 4.17 (a) and (b), respectively. According to theoretical band calculations [83] the electron pockets result from the population of the bottom of the Ti 3d conduction band. The theoretical band calculations are also shown as red dashed lines for comparison with the photoemission results. The theoretical band has been shifted to reproduce the experimental minimum in binding energy. In order to calculate the effective masses of the electron pockets bands surrounding M points, and to extract accurately the Fermi wave vector k_F values, for the different doping levels, a simulation of the dispersive bands has been performed. Results for $x = 0$ sample are illustrated in Fig. 4.17 (c) and (d). This band simulation has been made by considering a free-electron like parabolic dispersion, where the effective mass is introduced as a parameter to fit the exper-

imental data. Gaussian energy distribution curves (EDCs) are simulated, with the gaussian width coming from both contributions of the experimental energy and momentum resolution ($\Delta E \sim k \Delta k$). Finally, to take into account the effects of the Fermi-Dirac distribution near E_F , the resulting EDCs are multiplied by the Fermi-Dirac distribution for the given temperature. Solid purple lines represent the parabolic dispersion for the obtained effective masses. The Ti 3d band effective mass m^* along the ΓM direction is $5 m_e$ (m_e is the free electron mass), while for perpendicular KMK direction is about of $0.5 m_e$. Very similar values are found for doped samples, so we can claim no variation of effective masses with doping.

The fit values allow us to estimate the number of carriers, n_e , for the undoped and doped systems. k_F values estimated from the fitted bands are $k_{F1} = 0.177 \Gamma M$ and $k_{F2} = 0.181 KMK$ (where $\Gamma M = 1.08 \text{\AA}^{-1}$ and $KM = 0.62 \text{\AA}^{-1}$ are the corresponding BZ dimensions). These values are quite larger than the previous ones reported on literature [74]. Assuming an effective mass in the perpendicular direction to the plane (LM) of 16 (from ref. [74]), no m^* variation with doping, and ignoring the inclination angle from LM direction, we have estimated the number of carriers, for $x = 0$ and $x = 0.05$ samples. For the undoped sample $n_e = 6.1 \times 10^{20}$ while for the $x=0.05$ Nb concentration is $n_e = 2.05 \times 10^{21}$. Finally, the inset in Fig. 4.17 (a) shows the photoemission spectrum at the M point. From both pictures of Fig. 4.17 (a) and (b) there is a transfer of spectral weight to the higher binding energies, to the incoherent part of the spectral function. This will be discussed later in relation with probable weak correlation effects.

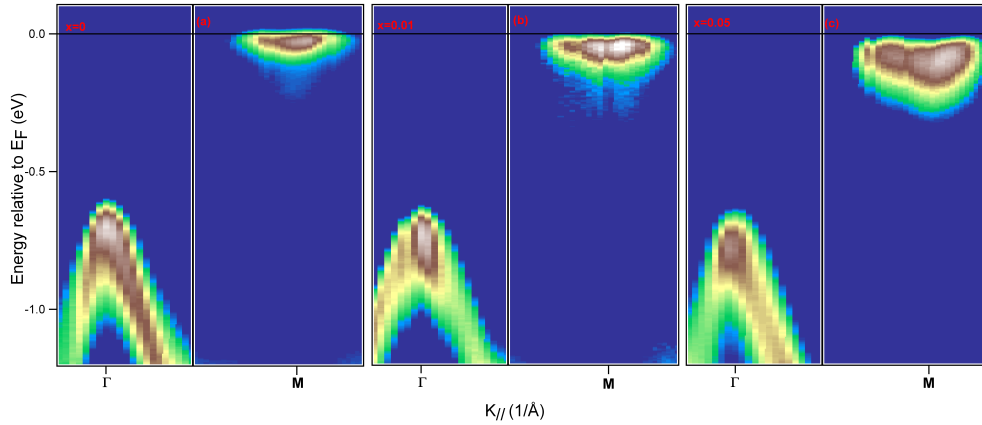


Figure 4.18: (color online) Photoemission intensity map for (a) 1T-TiS₂, (b) 1T-Nb_{0.01}Ti_{0.99}S₂ and (c) 1T-Nb_{0.05}Ti_{0.95}S₂ at 70 K near Γ and M points. The electron pockets around M point emerge, grow and sink with doping.

The photoemission spectra taken at 70 K along the high symmetric direction ΓM show a remarkable dependence with doping. Fig. 4.18 shows ARPES intensity maps for three different doping levels ($x=0, 0.01, 0.05$). The highly dispersive feature around the Γ point is the S

3*p* valence band. The sharp band feature near E_F around the M points, is attributed to the narrow Ti 3*d* conduction band, which dominates the DOS near the Fermi energy (E_F). Clearly, the Ti 3*d* band starts to extend far away from M point towards Γ with more Nb doping. At the same time, with increasing doping a systematic sinking of the *d* band below E_F is observed: the binding energy of the band minimum increases from 29 meV for $x = 0$, to 103 meV for the $x = 0.05$ sample. For larger doping levels – $x=0.1, 0.2$ and 0.3 (not shown here) – mainly the inelastic background of the ARPES spectra is strongly enhanced and the band line-width becomes even broader. Clearly, disorder leads to an enhancement of inelastic scattering, as was previously noticed in strongly Cu doped TiSe₂ [84].

It is interesting to note that with Nb doping both the S 3*p* band, near Γ , and the Ti 3*d* band, at the M point, continuously shift to higher binding energy. The shift is very similar for both Ti 3*d* and S 3*p* bands consistent with an electron doping rigid-band scenario. Moreover, a clear indirect gap as large as ~ 0.6 eV between the S 3*p* and Ti 3*d* bands is observed, whose position is defined by the centroid of the spectra. So, from the conventional definition, the system is a semiconductor.

In order to get more detailed information about the actual behavior of the electronic structure with doping, EDCs at the k_F point at $T=70$ K are compared for different doping levels in Fig. 4.19 (a). For ease of comparison, the three EDCs have been normalized to the same integrated intensity over the whole Ti 3*d* bandwidth. The line shape of pure TiS₂, typical of the metallic phase, is dominated by a sharp Ti 3*d* band at E_F . With increasing doping we observe a progressive shift of the QP peak and of the leading edge to higher binding energy. No Fermi edge in ARPES is visible in the EDCs for the $x=0.01$ and 0.05 samples, and the intensity at E_F significant reduced. The peak and leading edge shift, together with the strong suppression of spectral weight in the vicinity of Fermi level are unambiguous signs of the formation of a "pseudogap" (PG). Nevertheless, despite the energy shift, the gap does not open completely, and the ARPES spectra retain a small but finite spectral weight at E_F .

Temperature-dependent ARPES measurements were performed for the different doping levels. Results for $k = k_F$ are shown in Fig. 4.19 (b), (c) and (d), for doping levels $x = 0, 0.01$ and 0.05 , respectively. With the aim of revealing the spectral function, masked by the Fermi cut-off, underlying the ARPES data of Fig. 4.19 (a), we followed the common practice in ARPES on high temperature superconductors, of symmetrizing the spectra around E_F . This procedure removes the perturbing effect around E_F and symmetrizes according to E_F : $I^*(k_F; E) = I(k_F; E) + I(k_F; -E)$. The symmetrized spectra shown in Fig. 4.19 (b), (c) and (d) are proportional to the spectral function $A(k_F; E)$.

The agreement between ARPES and resistivity data is good. The spectral function of the pure TiS₂ sample exhibits a clear QP line shape. With decreasing T the coherent peak becomes narrower and more intense, consistent with the metallic behavior already illustrated in the

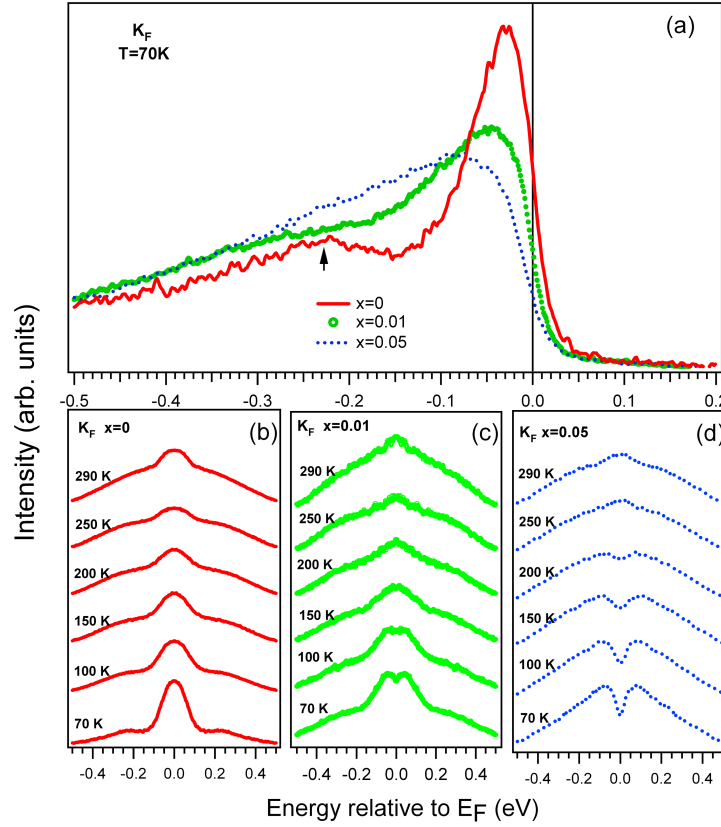


Figure 4.19: (color online) (a) Ti 3d band spectra at k_F for $x = 0$ (red line), $x=0.01$ (green open circle) and $x = 0.05$ (blue dashed line) doping levels. (b)-(d) Selected energy distribution curves symmetrized with respect to $E_F=0$ [$I_{symm}(\omega)=I_{raw}(-\omega)+I_{raw}(\omega)$] at k_F reveal the temperature evolution with doping for $x=0$, 0.01 and 0.05, respectively.

resistivity measurements. The scenario for Nb doped TiS_2 which emerges from Fig. 4.19 (c) and (d) is qualitatively different. Above the characteristic temperatures T^* obtained from the resistivity measurements, the symmetrized EDCs show QP peak features, similar to the undoped sample but weaker and broader. Below T^* , both samples ($x=0.01$ and $x=0.05$) exhibit a partial gap opening at E_F . While the partial gap opening is just incipient for the less doped sample, it seems already rather developed for the most doped one. Upon cooling down, the energy separation between the two symmetrized side peaks is gradually increased, indicating the further opening of the PG, and a decrease of the density of states at the Fermi level. Consequently, ARPES temperature dependent measurements seem in good agreement with the increasing electric resistivity below T^* for doped samples, indicating a transition from a metallic to a semiconducting phase for Nb doped samples. A similar scenario was already found for much higher Nb concentrations, as high as 60% [85]. However we have just shown that a very small Nb atom concentration, as small as 1%, is sufficient to induce this metal-to-semiconductor transition.

Possible scenarios for this PG include a CDW gap, a normal band gap, a correlation gap, and finally, a disorder-induced Coulomb gap. A CDW scenario must be discarded, because: (i) no CDW phases have been described in the parent compound nor did we observe them by LEED in the doped ones; (ii) the absence of the usual back-folding band in the electronic structure. The second and third scenarios may be also rejected mainly because the closest band to Fermi level (Ti 3*d*-Nb 4*d*) is far from being fully occupied, and, as it will be briefly discussed later, electronic correlations are not strong enough to induce this kind of PG. Therefore, the most probable scenario to explain the emergence of a PG with Nb doping is related to defects and disorder effects caused by substitution. This is supported by the fact that with increasing doping the QP peak width at k_F increases considerably, as shown in Fig. 4.19 (a), which emphasizes the important role played by defects after Ti substitution by Nb atoms. Usually, different kinds of disorder can lead to localization. One is the random positions of the atoms, that can lead to a random orientation of *p*- or *d*-like orbitals. If the degree of overlap can be changed by varying the mean distance between atoms, the composition or the coordination number, then a metal-insulator or metal-semiconductor transition may occur. In this case the random potential induced by substitution causes a strong scattering of electrons and at the same time degrades the coherence among electrons near E_F , leading to an opening of a PG at E_F , which induces the metal-to-semiconductor transition [86].

Finally, in Fig. 4.19 (a) and (b), we can also notice a weak satellite shoulder at ~ -0.22 eV, already signaled in the inset of Fig. 4.17. Previous studies on this system tentatively attributed a similar feature to the localized defect states induced by excess Ti atoms rather than band states [68, 87]. However, because of quite large effective mass of the Ti 3*d* band, and by analogy with other TMDs like 1T-TaS₂, we may expect that electronic correlations effects are not negligible in this compound. From Fig. 4.19 (b) one can attempt to roughly estimate the U/W ratio, taking U as the distance between the satellite peaks, and W the full width of the QP peak. This gives a value $U/W \gtrsim 1$. Therefore we can consider the spectral weight transfer to the incoherent part of the spectral function due to electronic correlations as the most probable explanation for the emergence of this satellite peak. In other 1T-TMDs materials (1T-TaS₂, 1T-TaSe₂) these electronic correlations become dominant and lead to an insulating Mott phase [88].

In conclusion, we have reported on a transport and ARPES study on 1T-Nb_{*x*}Ti_{1-*x*}S₂ ($x = 0$ to 0.05), including the FS topology and the electronic band structure. The effects of Nb doping on the electronic properties of TiS₂ have been analyzed and discussed. Without doping, the system is a narrow band gap degenerated semiconductor system that shows metallic behavior and weak correlation effects. Nb atoms mainly substitute the in-plane Ti atoms, and act as electron donors. The number of carriers increases from $n_e = 0.5 \times 10^{22}$ to 5.3×10^{22} , but disorder effects induced by Nb substitution become so dominant that the resistivity increases and a

pseudogap opens at the Fermi level, so the system undergoes through metal-to semiconductor transition.

4.4 2H-TaS₂

The last example of CDW in a TMD system that I have studied is that of 2H-TaS₂. Although the CDW in 2H-TaS₂ is weaker and not as complicated as in 1T-TaS₂, the electronic structure and CDW mechanism are still not completely understood. 2H-TaS₂ undergoes a CDW transition at $T=75$ K from the metallic normal state to a C-CDW state. The three unequal Ta sites, labeled as a , b and c , undergo weak displacements, forming a 3×3 superstructure, as illustrated in Fig. 4.20.

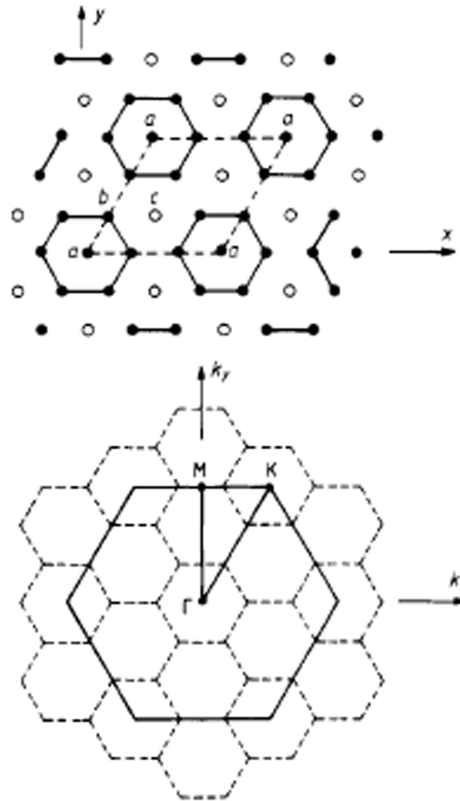


Figure 4.20: 3×3 superstructure of 2H-TaS₂. Real space (up) and reciprocal space (down). Γ , M and K mark the high symmetry points in the undistorted BZ.

A very interesting phenomenon in the 2H-TMDs family is the low temperature coexistence of CDW ordered states and superconductivity (SC). The delicate balance between the two instabilities can be influenced by external factors. In 2H-NbSe₂, as illustrated in Fig. 4.21, the CDW transition temperature T_{CDW} rapidly decreases under pressure, while the SC transition temperature T_c remains almost constant. At ambient pressure, T_c of the three typical CDW systems 2H-NbSe₂, 2H-TaS₂ and 2H-TaSe₂ is 7.2 K, 0.7 K and 0.14 K, respectively, while T_{CDW} monotonically increases from 33 K, to 75 K to 122 K. This strongly suggests that there is indeed a competition between CDW and SC in the 2H-TMDs family.

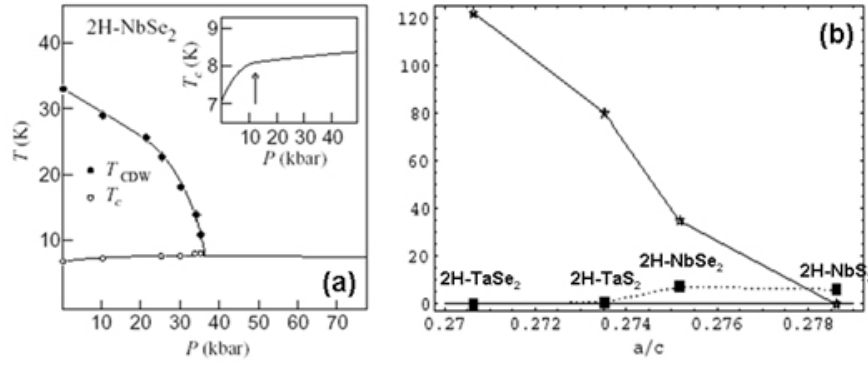


Figure 4.21: Competition and coexistence of CDW and SC in the 2H TMDs. (a) Variations of T_{CDW} and T_c as a function of pressure in 2H-NbSe₂. (b) Phase diagram: Stars, T_{CDW} ; filled squares, T_c . a is the in-plane lattice spacing and c is the interlayer spacing. Taken from [89].

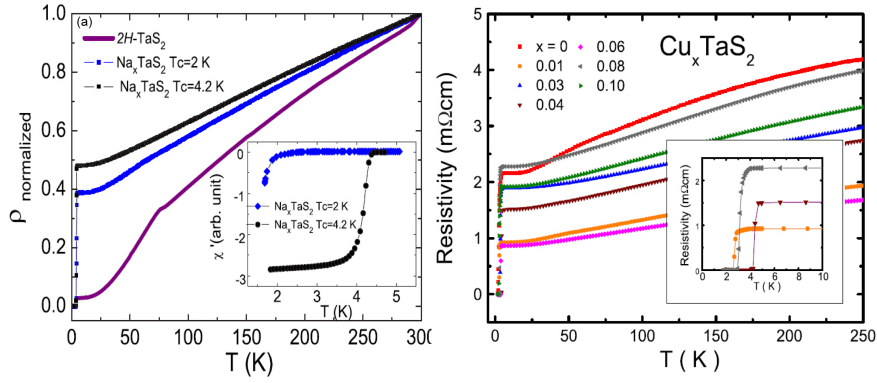


Figure 4.22: Superconductivity and charge-density-wave competition and coexistence in Na (a), and (b) Cu intercalated 2H-TaS₂ [90, 91].

SC is also observed in metal intercalated 2H-TMDs. Different metals yield different T_c s which increase – up to a limit concentration – with larger intercalation content. The intercalation induced change of the electronic properties of the host compounds can be mostly understood in terms of charge transfer, and the overall electronic structure of the host compounds does not undergo a noticeable change. However, the intercalant may induce changes of the DOS near the Fermi level, and eventually enhance T_c . For example, as illustrated in Fig. 4.22, Na or Cu intercalation in 2H-TaS₂ yields higher SC T_c , while at the same time the CDWs are suppressed or even disappear [90, 91]. I have found a similar behavior in the Sn intercalated 2H-TaS₂, which will be fully discussed in the following section.

4.4.1 The coexistence of superconductivity and charge-density-wave in 2H-Sn_xTaS₂ (to be submitted to Phys. Rev. B)

We investigated the electronic band structure and properties of Sn intercalated 2H-TaS₂ by high resolution angle resolved photoelectron spectroscopy (ARPES). A charge-density-wave (CDW) gap opens at the inner Fermi surface (FS) pockets centered around the equivalent K points, while no gap opening is observed on the hole FS sheet centered at the Γ point. The ARPES results further indicate that a weak FS nesting matches the inner K -point pockets and is likely to drive the 3×3 CDW. Besides a low energy kink in the valence band dispersion at ~ 50 meV, a high energy kink is observed at ~ 130 meV. It is interpreted as due to the hybridization between the valence band and the replicas induced by the CDW superlattice potential.

The study of broken symmetry states induced by electronic instabilities, such as superconductivity (SC) and charge-density-wave (CDW) represents one of the most intriguing research areas in strongly correlated electron systems. Broken symmetry phases are especially prominent in low-dimensional – quasi one dimensional (1D) and quasi two dimensional (2D) – materials [3]. The 2D transition metal dichalcogenides (TMDs) in particular, exhibit a variety of CDW transitions [35]. The trigonal prismatic (2H) polytype TMDs are such low dimensional systems where CDW order coexists with SC. Among the CDW-bearing members in this family, the CDW transition temperature decreases while the superconducting critical temperature (T_c) increases from TaSe₂ through TaS₂ to NbSe₂, suggesting that the CDW order and superconductivity indeed compete [35, 50]. Furthermore, upon intercalation of Na or Cu into 2H-TaS₂ [90, 91], the CDW transition temperature is reduced but the SC T_c increases from 0.8 to 4.4 K and 4.7 K, which is further evidence for the competition between these two ordered states. It is generally believed that superconductivity in the dichalcogenides is of the conventional BCS character, i.e. caused by electron-phonon coupling [92]. The Fermi surface (FS) is only partially gapped by the CDW, but the whole system remains metallic even in the CDW state. The 2D character and the existence of an anisotropic gap are quite similar to the situation encountered in the high- T_c cuprates. However, despite many studies of the electronic structure near the Fermi energy (E_F) [93, 94, 95, 96, 97, 98], the driving mechanisms for the CDW transition and the renormalization of the band dispersion [94, 96] are still poorly understood. Some authors [35, 50] argue that it is due to the FS instability (nesting). Others attribute this to the saddle point mechanism [49], or possibly to a novel mechanism – the Fermi patch scenario – which is rooted in the strong coupling nature of the electronic structure [97], but no final consensus has been established.

Angle resolved photoelectron spectroscopy (ARPES) is a momentum-selective probe of the electronic states and provides direct insight into fundamental interactions of a many-body system. ARPES is well adapted to investigate such low-dimensional materials. Previous ARPES

studies on 2H-TaSe₂ [93, 96, 99] and 2H-NbSe₂ [48, 94, 95, 100] did not observe any sharp changes associated with CDW transitions. 2H-TaS₂, which exhibits only one CDW transition at a relatively high temperature $T_{CDW} \sim 75$ K, is an ideal system to study the electronic properties of the CDW phase in the 2H-TMD family, and the competition with SC. However, no systematical ARPES investigations of 2H-TaS₂ have been reported, with the exception of one study on disordered and misoriented crystals [95]. Here we use high resolution ARPES to study the momentum dependent gap opening and the topology of FS of Sn-doped 2H-TaS₂, as well as the renormalization of the band dispersion.

2H-Sn_xTaS₂ single crystals were grown by chemical-vapor transport with the stoichiometry Sn_{0.4}Ta_{0.92}S₂. The in-plane temperature dependent electrical resistivity was measured by the four-probe method between 1.6 K and RT. The crystals were post-cleaved *in situ* to obtain mirror-like surfaces, which were characterized by low-energy electron diffraction (LEED). The data were mainly collected using a SPECS PHOIBOS 150 hemispherical analyzer and a high-brightness monochromatized GAMMADATA He lamp ($h\nu=21.2$ eV). Complementary measurements were carried out at the ANTARES beamline of the SOLEIL Synchrotron. The energy and momentum resolution were respectively 10 meV and ± 0.01 Å⁻¹. The Fermi level position was determined with an accuracy of ± 1 meV by measuring the metallic cutoff of a polycrystalline Ag film.

The top inset of Fig. 4.23 (Ref. [90]) shows the temperature dependence of the electrical resistivity of a pristine 2H-TaS₂. It exhibits a marked change of slope in correspondence of the CDW transition at ~ 75 K [90, 101]. By contrast, the in-plane electrical resistivity of Sn_xTaS₂, shown in Fig. 4.23, exhibits a weak feature around 65 K, and a sharp drop at $T \sim 2.9$ K to zero resistivity (bottom inset), indicating a superconducting transition. From these data, it is tempting to conclude that – similarly to the case of Na intercalation [90] – the CDW is partially suppressed in the Sn-intercalated sample, while SC is enhanced with respect with the pristine material, for which $T_c=0.7$ K.

FS mapping. Figure 4.24 (a) shows ARPES intensity maps of the FS at low temperature ($T=40$ K). Notice that, due to matrix elements effects, the intensity distribution is not uniform through the whole Γ and K FS sheets. In accordance with band theory [96, 102] and with a recent study on Na intercalated 2H-TaS₂ [97], the measured 2H FS consists of double-walled hole-like structures centered at the Γ and K points. The solid lines in Fig. 4.24 are from the tight binding (TB) calculation of Ref. [96]. The model only takes into account the Ta 5d_{z²} orbital: $E_k = t_0 + t_1(2 \cos \xi \cos \eta + \cos 2\xi) + t_2(2 \cos 3\xi \cos \eta + \cos 2\eta) + t_3(2 \cos 2\xi \cos 2\eta + \cos 4\xi)$, where $\xi = k_x a/2$, $\eta = \sqrt{3}k_y a/2$, and a is the lattice constant. The coefficients t_0 , t_1 , t_2 and t_3 are treated as fit parameters. A good simulation of the two Ta 5d-derived bands near E_F is obtained by setting the coefficients as follows: (1) (inner K pocket) $t_0 = -0.0453$, $t_1 = 0.4123$, $t_2 = 0.2825$, $t_3 = -0.015$ and (2) (outer K pocket) $t_0 = -0.0553$, $t_1 = 0.1980$, $t_2 = 0.2498$,

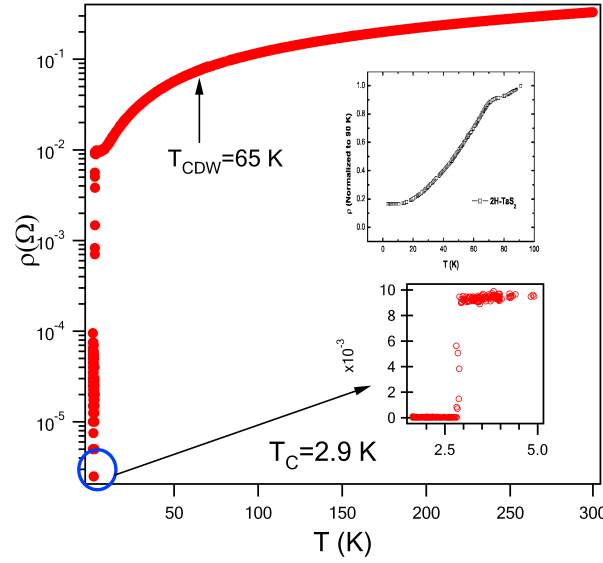


Figure 4.23: (color online) In plane electrical resistivity of 2H-Sn_xTaS₂. The top inset shows a resistivity data of pure 2H-TaS₂. The bottom inset shows a zoom in on the low-temperature region, with the signature of a superconducting transition at T~2.9 K.

$t_3 = -0.005$ (all energies in eV). The TB model from the Ta 5d derived bands near the Fermi energy reproduces quite well the FS structure, except for the splitting of the Γ pocket which is not well distinguishable.

As for all CDW systems, a crucial question is: what are the nesting properties of the FS? Electron diffraction measurements of 2H-TaS₂ and of Cu-intercalated 2H-TaS₂ find a CDW vector $q_{CDW} = 2/3 \Gamma M$ [91], in accordance with recent studies on 2H-TaSe₂ [47, 96]. The open circles contours in Fig. 4.24 are shifted by q_{CDW} . We find that only the inner K pocket shows weak FS nesting. For a more quantitative evaluation of the FS nesting scenario, we have calculated the autocorrelation of the FS. In order to eliminate the influence of ARPES matrix elements, in the following the autocorrelation is calculated from the theoretical TB model FS sheets of Fig. 4.24 (b) and (c), which well reproduce the experiment FS. The resulting autocorrelation maps are illustrated in Fig. 4.24 (d) and (e), and the intensity distributions extracted for the ΓM direction are shown in Fig. 4.24 (f). In correspondence of q_{CDW} we find an enhanced correlation for the inner K pocket, but not for the other FS sheets. This supports the conclusions of previous studies on 2H-TMDs, that only certain regions of the inner K pocket satisfy the CDW nesting condition [96, 102, 103].

Energy gap. The onset of a CDW state in a 2D system is expected to open an energy gap on part of the Fermi surface. Previous ARPES work reported that 2H CDW compounds, such as 2H-TaSe₂ and 2H-NbSe₂, indeed exhibit a partially gapped FS, with a finite energy gap opening around the K points, and no gaps on the FS sheets around the Γ point. Our

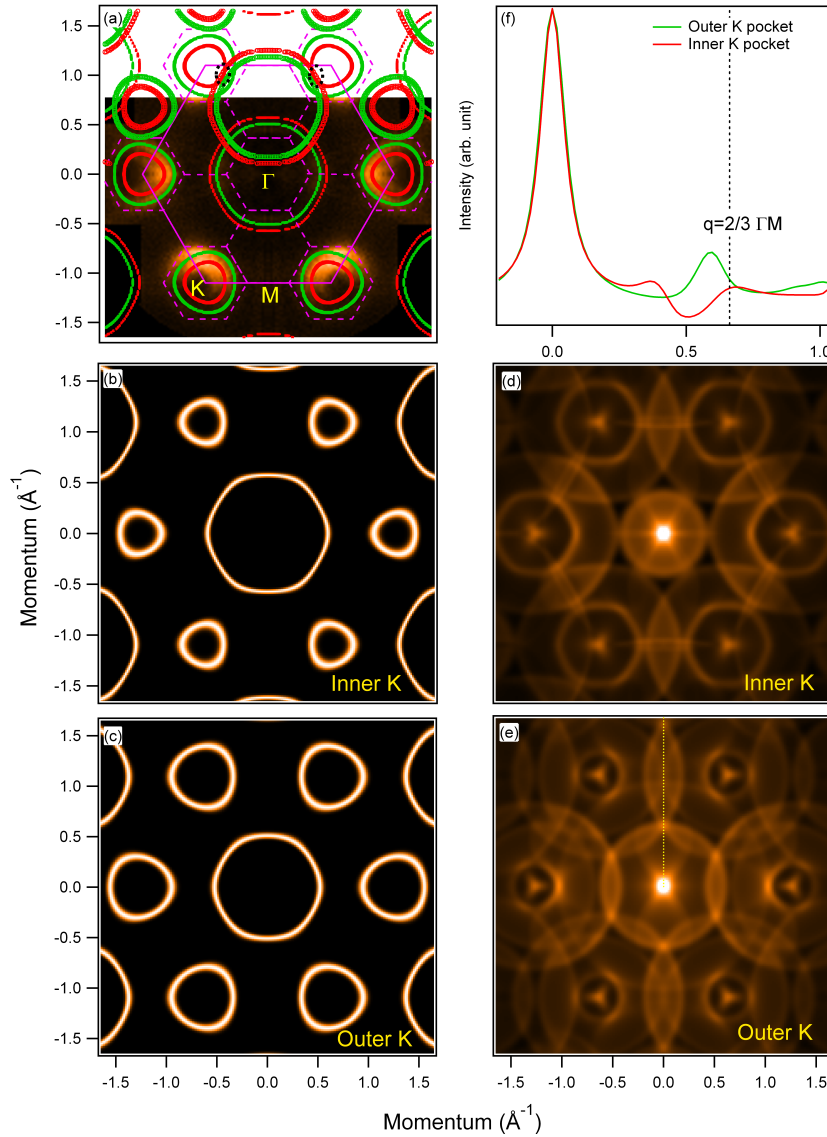


Figure 4.24: (color online) (a) Fermi surface map measured at $T=40$ K ($h\nu=50$ eV). The violet dashed hexagons are the Brillouin zone for the 3×3 superlattice. Solid lines are the simulated Fermi contours of the two Ta 5d-derived bands (red line is the inner K pocket, green line is the outer K pocket). Open circles in the upper part is the Fermi contours shifted by the experimental CDW vector $q_{CDW}=2/3 \Gamma M$. Regions of the FS that are nested – marked by black-dashed ellipses – are only found on the inner K -pocket sheets. (b) and (c) are the two Ta 5d-derived FSs (inner and outer K pockets) calculated by a tight-binding (TB) model. (d) and (e) are the autocorrelation maps of the models in (b) and (c), respectively. A dotted line marks the ΓM direction. (f) Intensity in maps (d) and (e) along the high symmetry direction ΓM , where a peak at the CDW vector indicates the nesting only in the inner K pocket for the TB model, in good agreement with the nesting found in (a).

ARPES data allow us to address this issue in $2H\text{-Sn}_x\text{TaS}_2$. The spectral changes near the Fermi energy across T_{CDW} can be followed in detail either from temperature-dependent energy

distribution curves (EDCs) or momentum distribution curves (MDCs). Figure 4.25 (a) and (b) shows the EDCs measured along the ΓK direction in the CDW ($T=20$ K) and normal ($T=70$ K) states, respectively. The three thick EDCs marked k_{F1} , k_{F2} and k_{F3} , correspond to three Fermi crossings. The first corresponds to the pocket around Γ (k_{F1}); the other two (k_{F2} and k_{F3}) to the K pockets. The EDCs at position k_{F1} and k_{F2} , shown in Fig. 4.25 (c) and (d), show temperature dependent changes. The increasing spectral weight at $T=20$ K near the Fermi energy can be assigned the sharpening of the Fermi-Dirac distribution function [104]. Furthermore, there is no apparent energy shift between the leading edges at the two different temperatures, consistent with a zero energy gap at the Γ and at the outer K FS sheets, in good agreement with previous ARPES data on 2H-TMDs [96, 102, 103]. By contrast, the EDCs at k_{F3} reveals an energy shift of the leading edge across the CDW transition, indicating the opening of a gap. A similar gap and spectral weight reduction at E_F in the temperature dependent spectra has similarly been observed in 2H-NbSe₂ [96] only for the inner K pocket. The MDCs at the Fermi energy of Fig. 4.25 (f) show a rich structure reproducing the Fermi level crossings, and the sharpening and shifts at the lower temperature. Here it is also possible to identify two weaker structures – indicated by arrows – which correspond to the replicas of the Fermi surface induced by the CDW superlattice potential.

What are the implications of these results on the nature of the CDW? The energy shift of the EDCs across T_{CDW} clearly singles out the role of the inner K -point FS barrel in the formation of the CDW. Contrary to theoretical predictions [50] of a gap opening on the Γ -point FS sheet, our data support other ARPES data which show that the K pocket is the only gapped part of the FS [96, 105]. Similar to 2H-NbSe₂, nesting conditions are indeed fulfilled for the inner K -point FS sheet.

Two kinks in the dispersion. Figure 4.26 (a) shows an ARPES intensity map along the Γ - K direction, near the K -pocket double-wall, at low temperature ($T=20$ K). The two bands are essentially parallel, but the details of the dispersion are different. The energy vs. momentum relation has been accurately determined by a two-peak Lorentzian fitting procedure of the MDCs as a function of energy. The experimental dispersions of the two bands extracted from the fit are indicated by red open symbols on the intensity map. The outer band – further from the K point – exhibits a linear dispersion all the way to E_F . By contrast, the inner band deviates from a straight dispersion (black line) and shows two ‘kinks’. The more prominent kink at ~ 50 meV (E_1) binding energy, has been reported before and well characterized in 2H-TaSe₂ and 2H-NbSe₂ [94, 99]. There, electron-phonon coupling – eventually leading to electron-hole pairing across the Fermi surface – was identified as the dominant contribution to the quasiparticle self-energy, which manifests itself as a renormalization of the band dispersion. The second kink at ~ 130 meV (E_2) is more surprising. Kinks in the dispersion – related to the *real* part of the electron self energy – must have a correspondence in the *imaginary* part

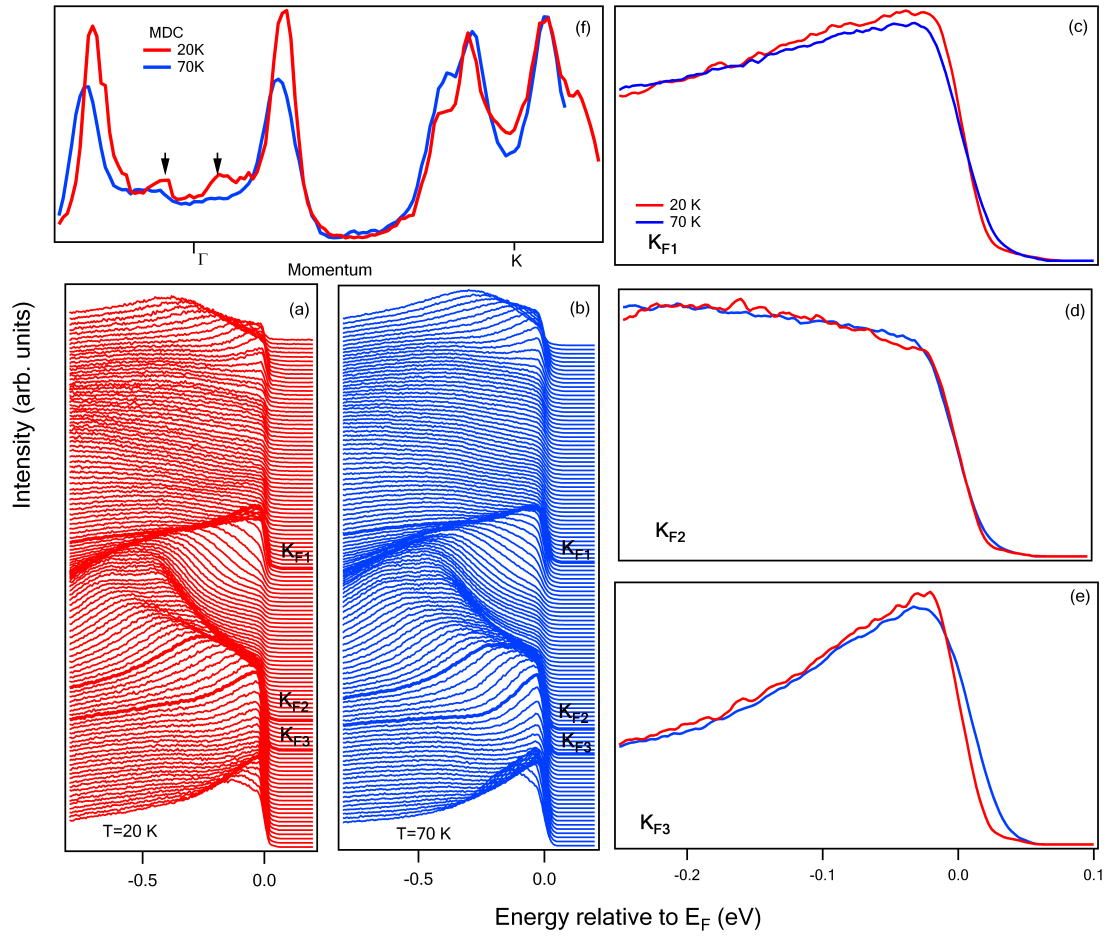


Figure 4.25: (color online) EDCs and MDCs across the CDW transitions. (a) and (b) EDCs measured along the ΓK high symmetry direction at low ($T=20$ K) and high ($T=70$ K) across T_{CDW} . The thick spectra marked k_{F1} , k_{F2} and k_{F3} , indicate the three Fermi crossings, corresponding to the Γ pocket and the K pockets, respectively. (c)–(e) Temperature-dependent EDCs across T_{CDW} , measured at k_{F1} , k_{F2} and k_{F3} . (f) Temperature-dependent MDCs across T_{CDW} measured at the Fermi energy from Γ to K .

of the self energy, which is related the QP line width. This is indeed the case. Figure 4.26 (b) illustrates the binding energy dependence of the full width at half maximum (FWHM) of the QP line shape for the two bands, extracted from the MDCs. The line width is independent of energy for the outer band. It shows instead two peaks at ~ 50 meV and ~ 130 meV for the inner band, corresponding to the kinks in the dispersion.

The origin of the high energy kink is not straightforward. Clearly, it cannot be assigned to the coupling with a single phonon or CDW mode, because its energy scale largely exceeds the maximum energy of phonons (~ 38 meV) [105] and CDW modes (~ 10 meV) [106]. The simulations of electron-phonon coupling with both Debye and Einstein models by Hengsberger *et*

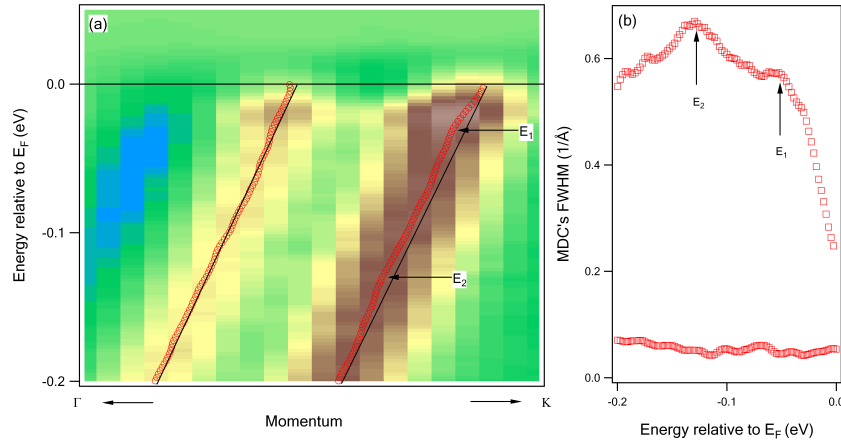


Figure 4.26: (color online) (a) Energy vs. momentum ARPES intensity map of 2H-Sn_xTaS₂ measured at T=20 K along the ΓK direction. Open circles are band energies extracted from the MDCs by a two-peak Lorentzian fitting. The two solid lines between the Fermi energy and -0.2 eV represent the bare bands. (b) The corresponding MDC widths (FWHM) for the outer band (bottom) and inner band (top) as a function of binding energy.

at. [107] excludes this scenario. Indeed, coupling to a bosonic mode at energy $\hbar\omega_0$ can affect the electron self-energy at energies above $\hbar\omega_0$, but cannot produce new distinct features. A coupling to multiple phonons is possible, but its effects are expected to be much weaker [108]. The energy of the anomaly in the self energy is influenced by the opening of a CDW gap. The low energy kink in the normal state is expected to be shifted to higher binding energy when the system enter into the CDW state. However, the maximum CDW gap size is only ~ 10 meV, and the ~ 50 meV kink should be shifted accordingly to ~ 60 meV, still quite far from the observed 130 meV. As an alternative interpretation, the high energy kink could be associated to the hybridization with a backfolded band in the CDW phase, similar to the case of 2H-TaSe₂ [96], where a two band hybridization model reproduces the high energy kink. Further work is necessary to explore this anomaly. In this respect, further synchrotron radiation measurements, where the photon energy can be tuned to an optimum value to enhance the visibility of specific band features, are required for a careful mapping of the superlattice bands.

CDW mechanism. Weak-coupling models of CDW formation predict that gaps form at locations of the FS that are coupled by the CDW vector. Previous ARPES study on 2H-TMDs and related metal intercalated compounds [45, 93, 94, 95, 96, 97, 100, 104, 109] showed that they all have similar FSs, with two double-walled hole pockets centered at Γ and K . There are several interpretations for the CDW mechanism in these materials. One is the traditional FS nesting scenario, which considers the opening of CDW gap at the K centered pockets of the FS connected by the CDW vector q_{CDW} [96, 103]. The possibility of self-nesting of parallel parts of the sheets centered at Γ is excluded, since it would require a different q_{CDW} , and the

opening of gaps which are not observed [45, 96]. A different scenario, suggested by Rice and Scott [49], focuses on the high DOS and related instability associated with saddle points close to the Fermi level. However, ARPES data indicate that the saddle points positions would lead to a 2×2 superstructure, inconsistent with the observed 3×3 CDW superstructure [45, 58, 95]. Recently, a new mechanism proposes that a CDW gap opens over the so-called “Fermi patch” around the M point of the BZ [97]. This scenario does not seem able to explain the observed temperature dependence of the ARPES spectra of Fig. 4.25.

Our ARPES data confirm the opening of a gap on the inner K -pocket FS sheet, which is related to the onset of the CDW transition shown in the resistivity data. Both ARPES and optical data indicate that the Γ pocket is unaffected by the CDW [95, 110]. Valla *et al.* [99] proposed that the Γ pocket dominates the transport properties, while the K pocket is in charge of the formation of a CDW gap. In turn, the gap would reduce electron scattering, and enhance the metallic behavior, in good agreement with the quick drop of resistivity of $2H$ -TaS₂ and Sn_{*x*}TaS₂ samples. Sn intercalation reduces the CDW transition by two possible mechanisms, either by a common disorder-induced reduction of the spectral weight at E_F , or because slight changes of the FS lead to a worsening of the nesting condition [110]. This, in turn, has an effect on the SC transition. Recent very high resolution ARPES data have revealed that superconducting gaps open at both the inner and outer K pockets of the sister compound $2H$ -NbSe₂ [94, 111]. A suppressed CDW in the Sn-intercalated material will leave larger ungapped regions of the inner FS, yielding a larger DOS than in the pristine compound. This provides a rationale for the increased SC T_c s.

In summary, we studied the electronic band structure and properties of Sn intercalated $2H$ -TaS₂ by ARPES. A CDW gap opens at the inner K pocket FS sheet, but not on the main FS sheet around the Γ point. The ARPES results further indicate that weak FS nesting only matches the inner K pocket and drives the 3×3 CDW. Besides a commonly observed low energy kink at ~ 50 meV, a high energy kink is interpreted as the result of hybridization with folded superlattices bands in the CDW state. The ARPES data confirm that the FS nesting scenario provides a framework to describe the competition of CDW and superconductivity in this material.

Chapter 5

Electronic structure and properties of Bi-family (BSCCO) cuprates

The discovery by Bednorz and Müller [14] in 1986 of high temperature superconductivity (HTSC) in cuprates materials has revolutionized many aspects of condensed matter physics. Still, despite extensive work in the past two decades, which have led to considerable experimental and theoretical advances, many important questions remain unanswered. A central issue in the HTSC is the role of the coupling between the two-dimensional CuO_2 planes which are believed to play a crucial role in superconductivity (SC). It has been experimentally established that the superconducting phase transition temperature (T_c) increases with the number (n) of copper-oxygen layers for $n \leq 3$, then decreases again [112, 113]. For example, in the Bi-based (BSCCO) family, the highest T_c is approximately 34 K, 95 K and 110 K for the optimally-doped one- (Bi2201), two- (Bi2212) and three-layer (Bi2223) materials, respectively. It is obviously of great importance to study the evolution of the electronic structure, in the normal as well as in the superconducting state, across the family. The Bi-based materials are actually the HTSCs compounds most studied by ARPES. The availability of large high quality single crystals and the presence of a natural cleavage plane between the BiO layers, are especially favorable for ARPES measurements. In the past, the one- and two- layer BSCCO compounds were well characterized. The three-layer compound is much less studied due to the difficulty to grow single crystals of sufficient quality and size. In this Chapter, I report the results of an ARPES investigation of the electronic properties of Bi2223. This experiment is the result of a collaboration involving the University of Geneva (Prof. D. van der Marel), the Paul Scherre Institut (Prof. J. Mesot, Dr. A. Bendounan), and the Swiss Light Source (Dr. M. Shi). The high quality samples used here were grown by Dr. E. Giannini (DPMC-Geneva).

5.1 Crystal structure of the layered Bi-based cuprates

5.1.1 Basic BSCCO structure

The crystal structures of the bismuth-based cuprate family for the one-, two- and three-layer compounds are shown in Fig. 5.1.

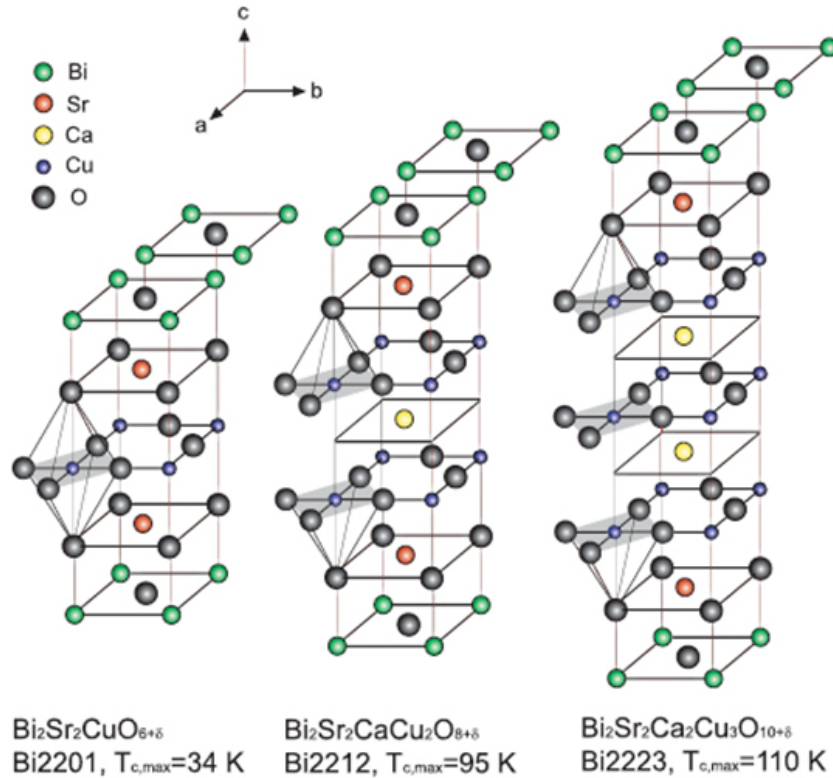


Figure 5.1: Crystal structures of BSCCO families of high temperature superconductors. The copper-oxygen planes are marked by the gray shadow.

For example, the unit cell Bi2223 of the average structure is pseudo-tetragonal with $a=5.4210$, $b=5.4133$ and $c=37.010\text{ \AA}$ [114]. This family of compounds, the first HTSCs not containing a rare earth element, were discovered in 1988 by several groups [113, 115, 116, 117]. These compounds usually grow as thin and small single crystals. They exhibit an easy cleavage plane between two BiO layers weakly bonded by Van-der-Waals forces, and therefore are almost ideal HTSC samples for STM and ARPES measurements. In particular, cleavage exposes a relatively inert surface, which preserves the underlying copper-oxygen layers. Spectroscopic data on freshly cleaved surfaces are therefore believed to reflect the bulk properties of the crystal [29].

5.1.2 The phase diagram of Bi family cuprates

Many electronic properties of cuprates superconductors depend on electron or hole doping. The parent compounds of cuprates at zero doping are antiferromagnetic (AFM) Mott insulators. The generic T_c vs. doping level is schematically shown in Fig. 5.2. Here and in the following I will only consider hole doping. As holes are added into the CuO_2 planes, the system enters an anomalous metal region, and then, above x_u , the so called underdoped SC regime. In this regime T_c rapidly increases with the hole concentration, and reaches a maximum at $x = x_{op}$ (optimal doping). Increasing the hole concentration above x_{op} – in the overdoped regime – yields a more metallic normal metal state. At the same time T_c decrease to zero at x_o , where the compounds undergo a transition from a superconductor to a normal metal at $T=0$. Although the schematic doping phase diagram appears symmetric relative to x_{op} , actually, the behaviors in the underdoped and overdoped regimes are quite different. A series of unusual properties, including a pseudogap (PG) above T_c , non-Fermi liquid behavior, and an unusual superconducting state usually appear in underdoped compounds.

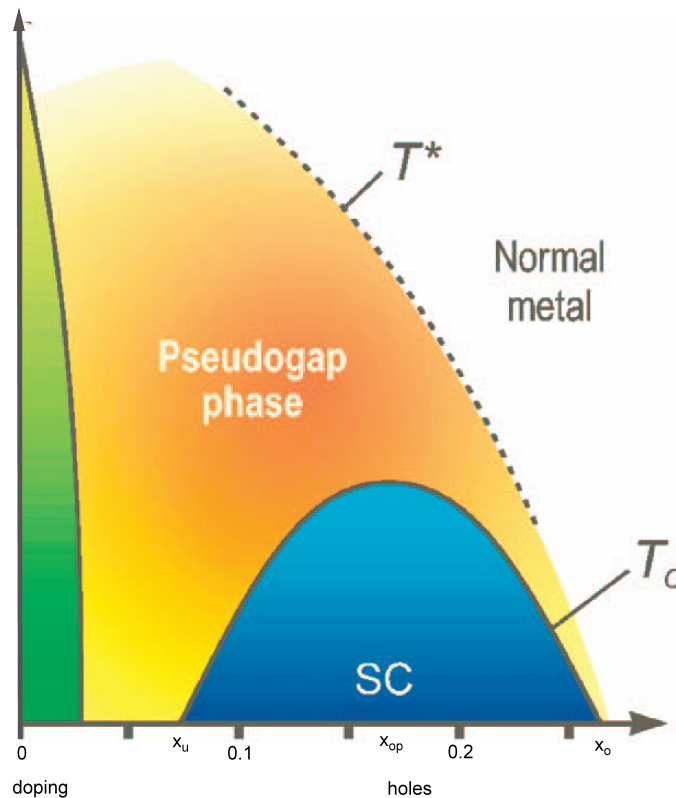


Figure 5.2: Schematic phase diagram of hole-doped high- T_c superconductors [118].

5.2 Structure and physical properties of Bi2223

5.2.1 AC magnetic susceptibility and scanning tunneling spectroscopy (STS) of Bi2223

The Bi2223 single crystals used in the ARPES experiments were grown by the group of E. Giannini at the DCMP of the University of Geneva by the traveling solvent floating zone method, followed by a post-annealing at 500 °C under oxygen pressure of 20 bar for 50 hours. The details of the growth process is described in Ref. [114]. The samples were rectangular, with a typical size of $0.5 \times 1 \text{ mm}^2$. The superconducting transition T_c was characterized by magnetic susceptibility measurements, as shown in Fig. 5.3 for an optimally doped (OPT) Bi2223 single crystal. T_c was 110.2 K, and the transition width was as narrow as 1-2 K, indicating the high quality of the crystal. Figure 5.4 shows STS spectra of OPT Bi2223, which exhibit an extremely high homogeneity over a range of at least 50 nm [119].

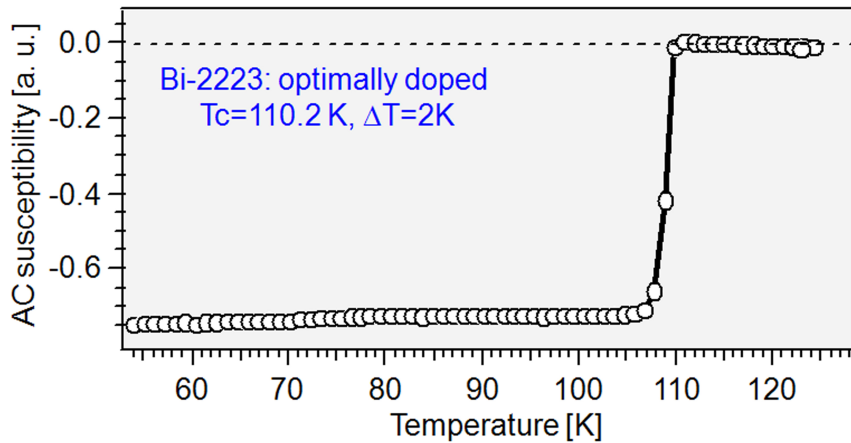


Figure 5.3: Magnetic susceptibility across the superconducting transition of an optimally doped Bi2223 single crystal with $T_c = 110 \text{ K}$ ($\Delta T_c = 1\text{-}2 \text{ K}$).

5.3 Electronic properties of Bi2223

5.3.1 Electronic band structure of Bi2223

Before discussing the electronic properties of Bi2223, let us first briefly review the complicated Fermi surface (FS) of BSCCO. Figure 5.5 (a) is the FS of Bi2212 determined by ARPES, from Ref. [120]. The (0,0) to (π, π) and $(\pi, 0)$ to (π, π) directions are dubbed ‘nodal’ and ‘antinodal’ respectively, with reference to the angular dependence of the SC gap on the FS (see below). The thick solid lines correspond to the main FS, and the dashed lines to the ‘umklapp FS’,

obtained by shifting the main FS by $Q = (\pm 0.21\pi, \pm 0.21\pi)$ (Fig. 5.5 (b)). Q is the characteristic vector of a ‘pseudo 5×1 ’ superlattice modulation within the BiO planes. The umklapp

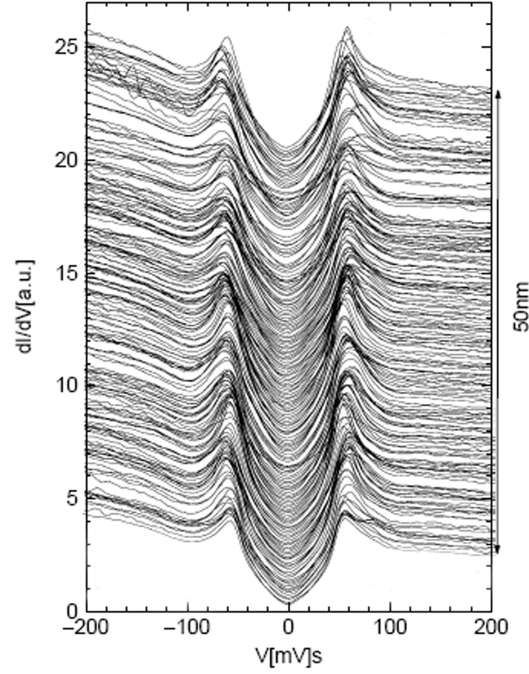


Figure 5.4: Scanning tunneling spectra of Bi2223 taken along a line of 50 nm on a high quality OPT single crystal at $T=1.8$ K [119].

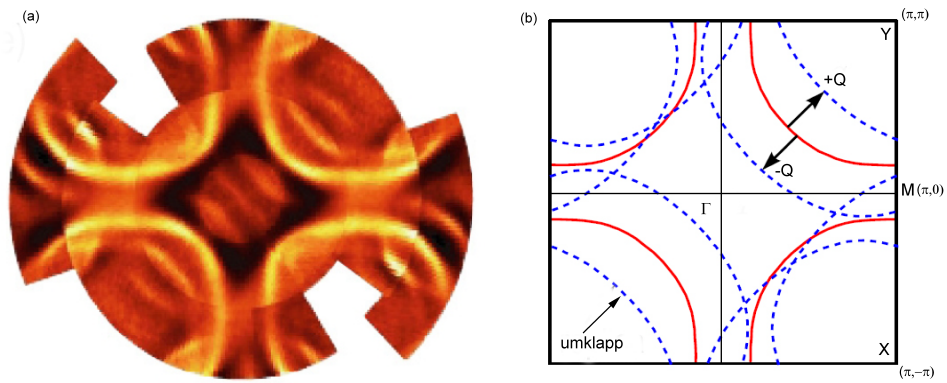


Figure 5.5: (a) Experimental ARPES intensity map at the Fermi surface of Bi2212, after Ref. [120]. (b) Schematics of the main FS and of the superstructure replicas (umklapp). The red lines are obtained by a tight binding fit to the dispersion data of the main band. The dashed lines correspond to $(0.21\pi, 0.21\pi)$ umklapps of the main band.

bands are due either to the effect of the Bi-O plane distortion on the CuO_2 plane, or simply to the diffraction of the escaping photoelectrons from the Bi-O plane [121]. Evidently, these umklapps present an additional obstacle for the data analysis. To reduce their effect, BSCCO can be doped by Pb which partially replaces the Bi atoms in the lattice and removes the modulation. However, doping with Pb is only efficient in one- and two-layer BSCCO. It is quite difficult to achieve Pb-doping in Bi2223, and this adds to the complexity of the analysis of the ARPES data.

As mentioned already, the change in the number of layers (n) in the unit cell affects the superconductor system in many different ways. Firstly, the chemical environment around the CuO_2 planes is different depending on n . For example, the Cu ions in the outer CuO_2 layers of Bi2223 have the same chemical environment (pyramidal coordination) as the two copper-oxygen planes in Bi2212, while the inner CuO_2 layer of Bi2223 has no apical oxygens [122]. Secondly, the different environment and coupling between neighboring CuO_2 layers alter the band dispersion and therefore the shape of the Fermi surface. ARPES studies of the bilayer Bi2212 [123, 124, 125], tri-layer Bi2223 [126] and four layer $\text{Ba}_2\text{Ca}_3\text{Cu}_4\text{O}_8\text{F}_2$ (F0234) [127] compounds have revealed the splitting of the conduction band and FSs. For example, in overdoped (OD) Bi2212, the hybridization between the two CuO_2 layers causes the splitting into bonding and anti-bonding bands [123, 124]. The Bi2223 data give evidence for two different gaps, associated with the outer and inner CuO_2 planes [126]. The ARPES results from the four-layer compound F0234 revealed two FS sheets corresponding to different hole concentrations in the outer and inner CuO_2 planes [127].

In order to investigate the role of multiple CuO_2 planes and of interlayer coupling on the electronic structure of the cuprates, and their influence on superconductivity, we have studied by ARPES the three-layer compound Bi2223. From a comparison of the present results on Bi2223 with the ARPES data on single- and double-layer BSCCO, several issues are addressed in this section, namely:

- (1) the appearance of the coherent peak in the nodal and anti-nodal directions,
- (2) the shape of the FS in overdoped samples,
- (3) the superconducting gap magnitude and symmetry.

The ARPES measurements were performed at beamline SIS of the Swiss Light Source (SLS). We used a GAMMADATA SCIENTA SES-2002 spectrometer, with an angular resolution of better than 0.15° . The energy resolution was respectively 17 meV and 12 meV for the high-intensity and high-resolution measurements. The Fermi energy was determined by recording the photoemission spectra from a polycrystalline copper sample. The clean surface for ARPES measurements was obtained by *in situ* cleavage in an ultrahigh vacuum of 5×10^{-11} mbar.

Figure 5.6 presents a summary of the ARPES data for the superconducting state ($T = 12$ K) of an OPT Bi2223 sample, along the nodal and antinodal high-symmetry directions in the first

Brillouin zone (BZ). The observed quasiparticle (QP) line shape is similar to those of the one- and two-layer compounds [128]. The rather flat QP band near $(\pi,0)$ (cut2 along MY) reflects the presence of a van-Hove like singularity in the band structure below E_F . By contrast, a sharp QP peak exhibits a rapid dispersion along the $(0,0)$ to (π,π) direction (cut1 along ΓY), defining a clear Fermi level crossing. The same figure shows an umklapp band from the superstructure in the Bi-O layers, shifted by $\pm(0.21\pi, 0.21\pi)$ with respect to the main bands. A comparison of the ARPES spectra at the nodal and antinodal points of the FS is illustrated in Fig. 5.6 (e). In the former case the line shape reveals a resolution-limited cut-off at E_F , consistent with no gap. At the antinodal point, on the other hand, the QP peak is well removed from E_F , indicating the opening of a superconducting gap.

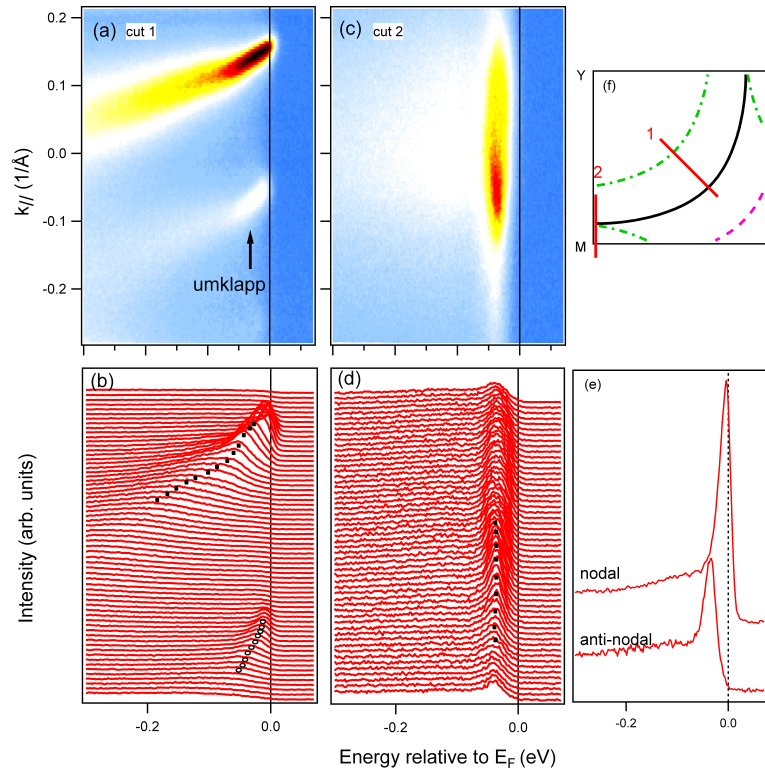


Figure 5.6: ARPES spectra of the superconducting state of Bi2223 along high-symmetric directions at $T=12$ K. (a) ARPES intensity maps along $(0,0)$ to (π,π) . (b) The energy distribution curves (EDCs) corresponding to (a). (c) Intensity map along $(\pi,0)$ to (π,π) , and (d) the corresponding EDCs. Main (umklapp) bands are marked with bars (open circles). (e) Comparison of EDCs at nodal and antinodal regions. Clearly, no gap opens in the nodal direction, but an evident gap occurs in the anti-nodal region. The corresponding cuts 1 and 2 are indicated in (f).

As a result of the interaction between the CuO_2 planes along the c -axis mentioned above, a clear splitting of the conduction band in bonding and antibonding bands, and of the FS, has been observed in the bilayer systems Bi2212 and YBCO [123, 124, 125, 129]. Figure 5.7

(a) presents the normal state data from a $T_c=65$ K overdoped Bi2212 sample [123]. Two Fermi surfaces – a bonding (BB) and an anti-bonding (AB) one – are observed for the main band as well as for the umklapp bands (BB' and AB'). These split FS sheets correspond to four well-resolved quasi-particle peaks (Fig. 5.7 (b)). Since Bi2223 has three CuO_2 planes, a tri-layer splitting – i.e. the splitting into 3 bands: bonding, non-bonding and anti-bonding – can be anticipated in this system. A threefold splitting has also been predicted by a $t'-t''-J$ model calculation [130].

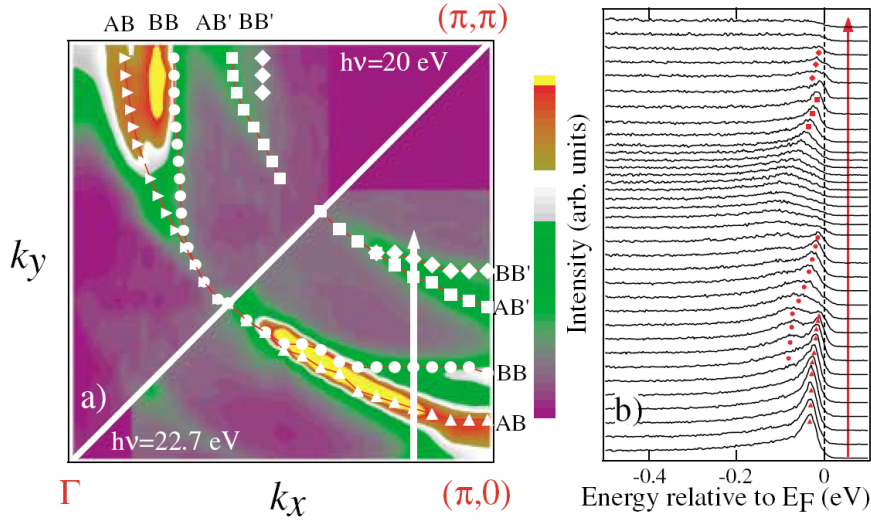


Figure 5.7: Bilayer splitting in overdoped Bi2212 ($T_c=65$ K): (a) Fermi surface ARPES intensity map. White symbols are the FS crossing estimated directly from the dispersion of the peaks. BB and AB refer to main bonding and anti-bonding bands, and BB' and AB' to the corresponding umklapp bands. (b) ARPES spectra along the cut indicated by the white arrow in panel (a). (From Ref. [123])

Feng *et al.* [122] compared the normal state at $(\pi,0)$ spectra on OPT Bi2201, Bi2212 and Bi2223 using different photon energies, as shown in Fig. 5.8. The line shape of Bi2201, without multi-band structure, is independent on the photon energy, while that of Bi2212 is modulated due to the different photon energy dependence of the photoemission matrix elements for the bonding and antibonding bands. The same figure shows that the band splitting in Bi2223 is absent or at least much weaker than in Bi2212. Such unexpectedly weak tri-layer splitting was ascribed to the difference on chemical environment among the three CuO_2 planes. According to the theory of M. Mori [130], the inner and outer layers of Bi2223 would have different hole concentrations: the inner-layer hole concentration being 15% to 25% smaller than that of the outer-layers. Therefore, the inner-layer is underdoped, so that electronic correlations are strong and will severely reduce the effective hopping between the outer and inner layers (see Ref. [122] and references therein). In other words, the inner-layer would act as a separator between the two outer-layers, and the tri-layer splitting would

then be strongly reduced. However, despite this theoretical suggestion, more data on different samples are required before the issue can be considered to be definitely solved.

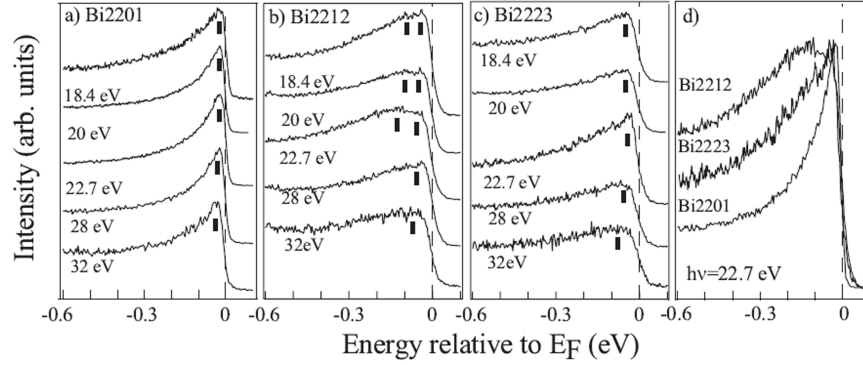


Figure 5.8: Photon energy dependence of the normal state ($\pi,0$) ARPES spectra for optimally doped: (a) Bi2201 at 40 K ($T_c=33$ K); (b) Bi2212 at 110 K ($T_c=90$ K); (c) Bi2223 at 125 K ($T_c=108$ K). (d) Direct comparison of the ($\pi,0$) ARPES spectra taken with 22.7 eV photons from panels a-c. (From Ref. [122])

Figure 5.9 (a) shows that the conduction band is split into two in the region between node and antinode in the superconducting state ($T=12$ K). The splitting gives rise to separate Fermi surface sheets, indicated by black and red solid lines. It is also well resolved in the super-lattice band. This observation does not confirm the expected threefold splitting for a three layer system. It supports the hypothesis of inequivalently doped outer and inner CuO_2 layers, with a weak coupling between the two outer layers. In this case, the nearly degenerate bonding and anti-bonding bands are not resolved [126], and give rise to the same outer layer (OL) Fermi surface. On the other hand, the band derived from the inner layer (IL) is distinct because of the lower doping level, and it gives rise to a separate IL Fermi surface. Circumstantial evidence for this scenario is provided by an analysis of the width of the features in the momentum distribution curve (MDC) (shown in Fig. 5.9 (b)). The full width at half maximum (FWHM) for the OL bands at the Fermi crossing, ~ 0.058 (\AA^{-1}), is significantly larger than that of the IL band, ~ 0.036 (\AA^{-1}), strongly suggesting the presence of two unresolved bands in the former.

Remarkably, an intensity map measured near the antinode region (Fig. 5.10) shows three parallel dispersive structures near the Fermi level, indicated also by dashed lines overlaid on the EDCs in Fig. 5.10 (b). Figure 5.10 (c) illustrates the MDC at the Fermi level, which clearly exhibits three peaks, possibly corresponding to anti-bonding, bonding and non-bonding bands. A fit of the MDC with three Lorentzian functions yields a splitting of 0.059 \AA^{-1} between the bonding and anti-bonding OL bands. The line widths of the split bands are 0.064 and 0.084 \AA^{-1} , and 0.042 \AA^{-1} for the IL band. The FWHM of the two split OL bands is nearly the same as that of the Bi2212 bands, ~ 0.08 \AA^{-1} in the superconducting state [131]. A complication in

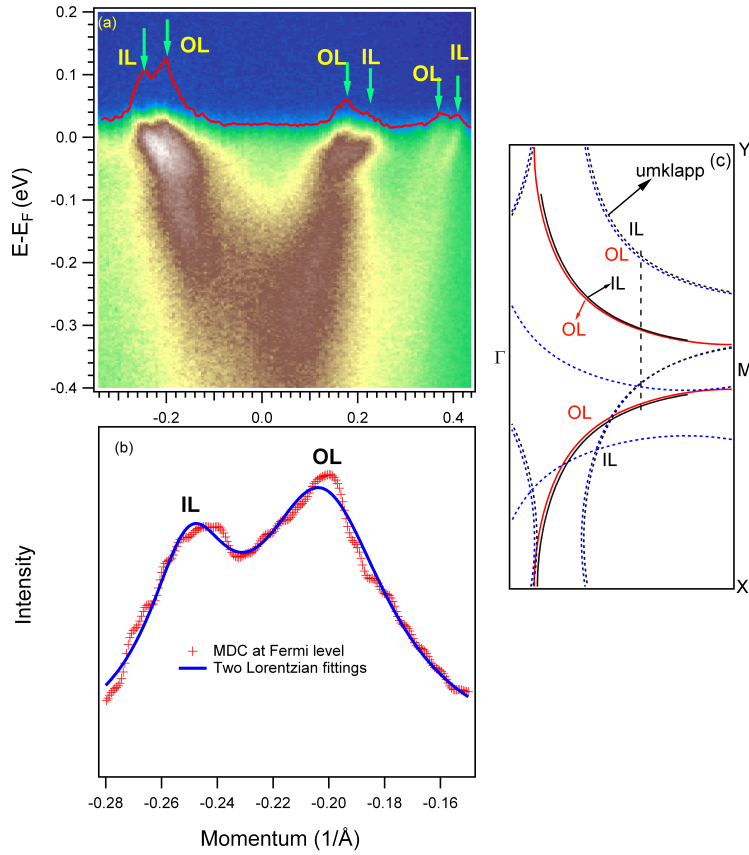


Figure 5.9: (a) ARPES intensity map of OPT ($T_c=110$ K) Bi2223, measured at $T=12$ K ($h\nu=55$ eV) along a cut close to the node location on the FS, shows a clear interlayer splitting. The splitting is also seen in the superlattice band. The curve on the top is an MDC at the Fermi energy. The arrows indicate a splitting into two separate dispersing features. (b) Enlarged MDC from (a). The blue solid line is a fit of the MDC with two Lorentzian functions. (c) Schematics of the BZ with the measured cut (black dashed line). Two Fermi surfaces of the main band (solid lines) are observed corresponding to non-resolved OL bands (red lines) and to an IL band (black lines). The same structure is found in the umklapps (dotted lines).

the analysis is the possible interference from the umklapp bands, which could be mistaken for a split component of the main band. However, if one of the split bands were to be assigned to umklapp1 (see Fig. 5.10 (d)), its dispersion should have opposite curvature to that of the main band. If, on the other hand, the split band was actually umklapp2, it would indeed be parallel to the main band, but shifted $\sim 0.21\pi/a$ away from it (as found the umklapps in Fig. 5.9). Thus we tend to believe the observed close and parallel dispersive bands indeed reflect the trilayer splitting into bonding, anti-bonding and non-bonding bands. Closer to the antinodal region the splitting cannot be fully resolved anymore in our data (not shown).

Further experiment with variable photon energy and polarization could help resolve the split structures, or set upper limits to the splitting, over the whole Fermi surface.

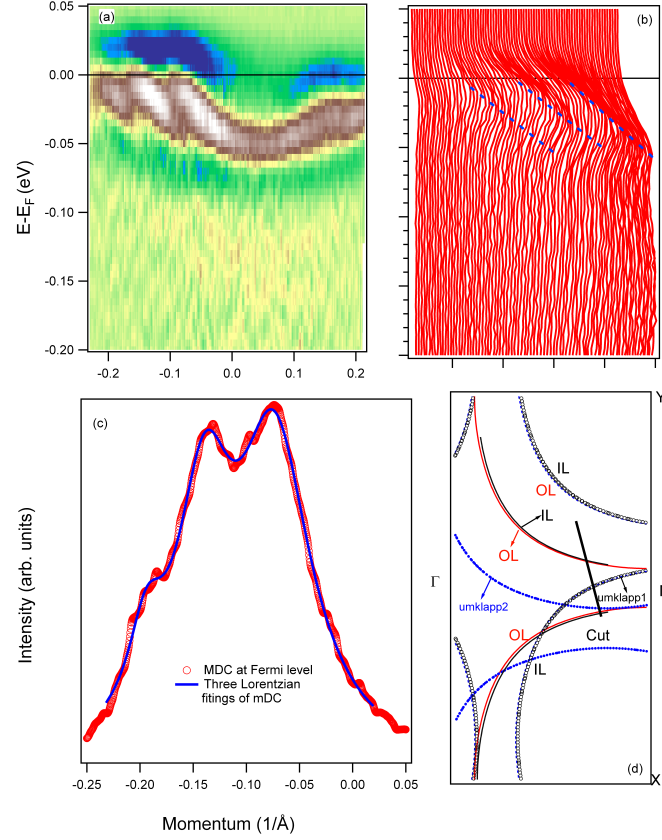


Figure 5.10: (a) ARPES intensity map measured near the anti-node region. It shows three separate dispersive bands. (b) The corresponding EDCs. The three dashed lines highlight the three split bands. (c) The MDC (red open circles) obtained at the Fermi level. The solid blue line is a fit with three Lorentzian functions. (d) Schematics of the BZ with the measured cut.

5.4 The superconducting energy gap

5.4.1 Two kinds of wave symmetries

The question of the symmetry of the superconducting gap is a crucial topic in high T_c cuprates research, and a key point to understand the nature of superconductivity [132, 133, 134]. On the one hand, in the simple BCS theory, as mentioned in **Chap.2**, Cooper pairs are described by a single wave function with spherical symmetry, or s-wave symmetry, for conventional superconductors. Therefore, Cooper pairing is called s-wave pairing. More complex symmetries are possible. Strong Coulomb interactions among the charge carriers and anti-ferromagnetic spin fluctuations favor a d-wave symmetry of the gap in superconducting state. In a nutshell,

the d-wave symmetry allows the two paired electrons to keep clear from each other, reducing their Coulomb repulsion [134].

The different nature of the s-wave and d-wave gap symmetries are illustrated schematically in Fig. 5.11. The s-wave gap function has zero angular momentum and spherical symmetry, i.e. the gap is the same everywhere on the Fermi surface. The d-wave gap function has a cloverleaf shape, with four leaves directed along the a and b axes within the CuO_2 plane. The d-wave gap has a fourfold symmetry, with maxima along the Cu-O bond directions, and zeroes at 45° in between, i.e. when $|k_x| = |k_y|$. The d-wave order parameter is actually complex, and it changes sign across the zeroes. This aspect can be probed by experiments that are sensitive to the phase of the order parameter, like tunneling, but not by ARPES, which only reveals its absolute value. Though there are still hot debates on the detailed behavior of the gap function in the HTSC cuprates, it is now well established that it has a predominantly $d_{x^2-y^2}$ symmetry: $\Delta(k) = \Delta_0 |\cos k_x - \cos k_y|$ [134, 135, 136].

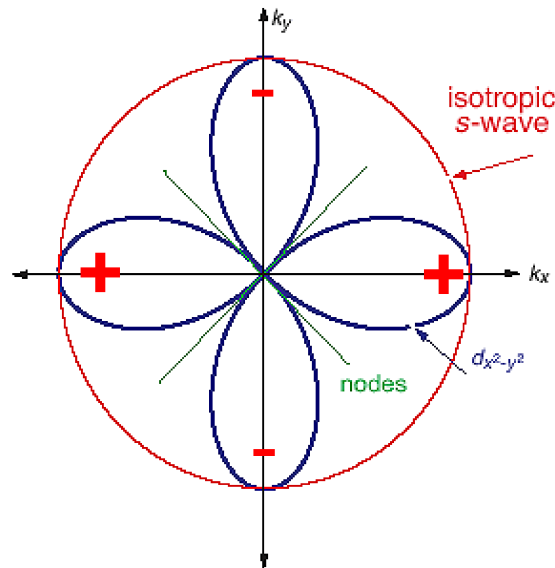


Figure 5.11: Isotropic s-wave (out circle, red), d-wave (four leaves, blue lines). The "+" and "-" denote the sign of the order parameter.

5.4.2 Superconducting gap from ARPES data in Bi2223

d-wave symmetry gap

Before proceeding with the ARPES results, it is important to comment on the procedures which can be used to estimate the gap size from the ARPES data. One common procedure is

to define the leading edge gap (LEG) which is determined as the lowest binding energy of the middle point of the spectral leading edge [137, 138, 139]. The advantage of this approach is that one can directly compare the superconducting gap and a possible normal state gap. An alternative method is the symmetrization procedure proposed by Norman *et al.* [140]. The ARPES spectra are cut off by the temperature-dependent Fermi function at the Fermi level. In order to investigate the intrinsic temperature evolution of the gap value it is necessary to remove the temperature broadening from the spectra. It can be removed by a symmetrization of the spectra around E_F :

$$I^*(k_F; E) = I(k_F; E) + I(k_F; -E) = c * A(k_F; E) f(E) + c * A(k_F; -E) f(-E), \quad (5.1)$$

where c is a constant. Since for the Fermi function $f(E, T) = (1 - f(-E, T))$, and electron-hole symmetry requires $A(k_F; E) = A(k_F; -E)$, equation 5.1 reduces to $I^*(k_F; E) = c * A(k_F; E)$. Therefore, the symmetrized spectra – e.g. those at the node and antinode locations shown in Fig. 5.12 – can be considered to be proportional to the spectral function $A(k_F; E)$. A single peak is observed in the nodal symmetrized EDC indicating that no energy gap opens there. By contrast, the symmetrized spectrum at the antinodal location shows two peaks, which reflect the superconducting gap opening.

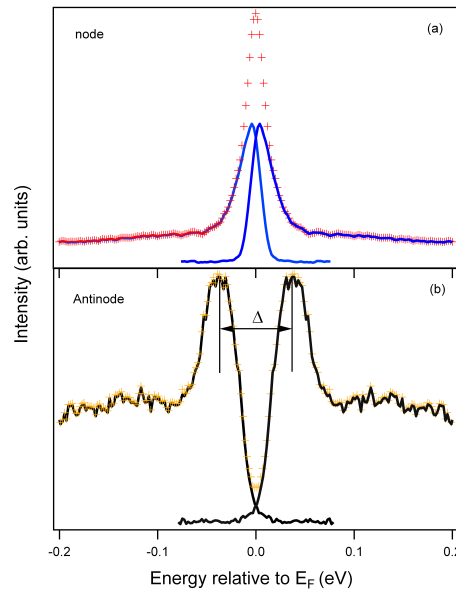


Figure 5.12: Symmetrization of the ARPES spectra at the node (a) and antinode (b) location, following the method suggested by Norman *et al.* [140]. Solid lines are the ARPES spectra, and the “+” symbols show the spectra after symmetrization. Both spectra were measured below T_c .

By symmetrizing the EDCs as a function of momentum and temperature, one can identify a superconducting gap ($\Delta(k)$) consistent with a *d*-wave symmetry. Figure 5.13 shows that at the

nodal point the symmetrized EDC exhibits a sharp quasiparticle peak, indicating the absence of any gap. On the other hand, in the antinodal region the symmetrized EDC shows two peaks on both sides of the Fermi level, corresponding to a maximum gap amplitude Δ_0 of 32 ± 2 meV¹ for the optimally doped Bi2223 sample, in good agreement with STS experiments [118, 119] and previous ARPES reports [141, 142, 143]. Notice that the maximum gap size of Bi2223 is larger than that of optimally doped Bi2212 (~ 20 meV). Feng *et al.* and Sato *et al.* [141, 144] suggested that in the cuprates the maximum T_c is determined by the pairing strength (maximum gap amplitude Δ_0) and the superfluid density ρ_s or condensate fraction (see Ref [141] and references therein). For optimally doped Bi2223 both of these two ingredients of superconductivity are larger than Bi2212 and Bi2201. Feng *et al.* [141] found that the superconducting peak ratio (SPR)– defined as the ratio between the integrated intensity of the SC peak and that of the whole spectrum – linearly increases with the number of CuO_2 layers n ($n \leq 3$). This is qualitatively consistent with muon spin resonance (μSR) results, which show that ρ_s is larger for the optimally doped cuprates with more CuO_2 layers ($n \leq 3$), and scales with T_c in approximately a linear fashion as in the celebrated “Uemura plot” [145].

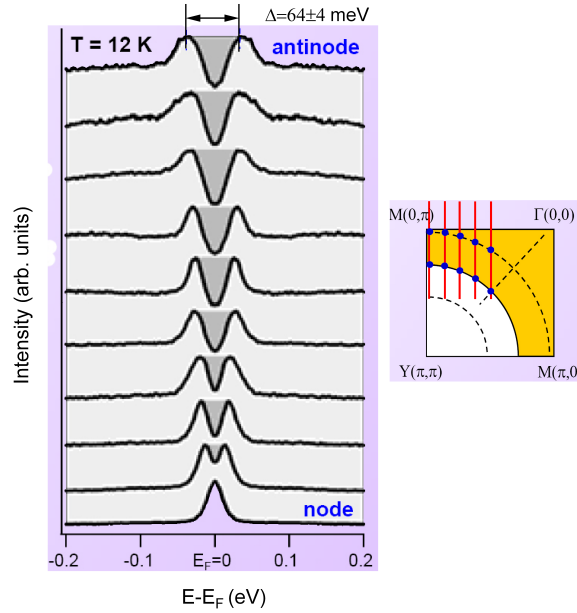


Figure 5.13: Symmetrized EDCs of OPT Bi2223 measured at $T=12$ K along the FS show an anisotropic superconducting gap, with the largest gap at the antinode. The inset shows the actual cuts in the BZ probed by ARPES.

The momentum dependence of the superconducting gap along the FS is shown in Fig-

¹Here I consider $\Delta_0(T = 0K) \simeq \Delta(T = 12K)$, because the superconducting gap of Bi2223 approximately follows a BCS temperature dependence.

ure 5.14. The superconducting gap can be fitted by a d -wave functional form $\Delta = \Delta_0 |\cos k_x - \cos k_y|$, where Δ_0 is the superconducting gap amplitude. This d -wave symmetry is consistent with the previous work on Bi2223 [141, 143, 144], and also similar with Bi2212 [140].

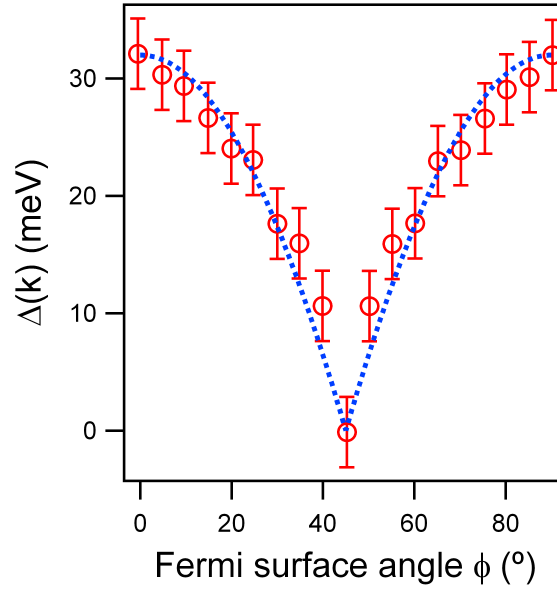


Figure 5.14: The superconducting gap size of OPT Bi2223 ($T=12$ K) follows a characteristic d -wave symmetry and can be modeled as a function $\Delta(k) = \Delta_0 |\cos k_x - \cos k_y|$ (blue dotted line).

Gap evolution with the temperature in different regions along the FS

It is well accepted that the nature of conventional superconductors can be well understood by the BCS theory. Within the framework of BCS model, the superconducting gap $\Delta(T)$ is weakly temperature dependent at low temperature, and rapidly drops to zero approaching T_c . While there is no generally accepted microscopic theory for the HTSCs, it is worth to see if the BCS theory is able, under certain conditions, to describe aspects of the physics of high T_c cuprates. For underdoped (UD) and optimally doped (OPT) cuprates, a pseudogap (PG) appears near the antinodal region and may compete with the superconducting gap on the Fermi surface [17]. Overdoped (OD) copper oxides, on the other hand, have a much weaker PG effect and therefore provide a good opportunity to investigate the superconducting gap. Figure 5.15 illustrates the temperature dependence of the SC gap at three different locations of the Fermi surface for an OD ($T_c=108$ K) Bi2223 sample. The symmetrized spectra in Fig 5.15 (a)-(c) suggest a collapse of the superconducting gap when the temperature approaches T_c . In order to perform a more quantitative analysis of the gap size, I fitted our data by a phenomenological

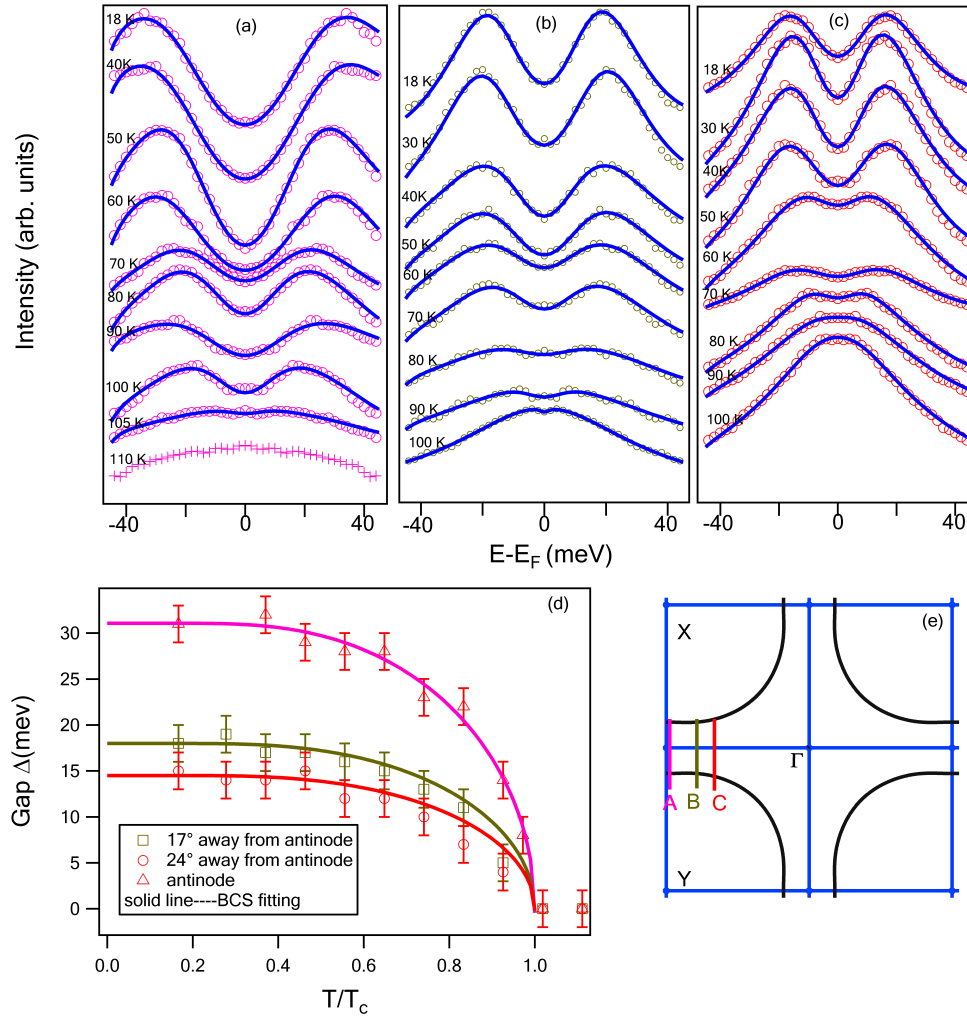


Figure 5.15: Detailed temperature evolution of the superconducting gap for three different cuts in the first BZ of OD Bi2223 ($T_c=108$ K). All of the spectra were measured along cuts parallel to the $(\pi,0)$ - (π,π) direction, using $h\nu=27$ eV photons. (a)-(c) Temperature dependence of symmetrized EDCs at the Fermi crossing points A (antinode), B (between node and antinode) and C (close to the node). (d) Temperature dependence of the fitted gap size at the Fermi crossing points at the three different positions, as indicated in (e). The solid lines are the temperature dependence of the superconducting gap according to the BCS theory and a guide to the eye.

model which has been shown to be successful in modeling ARPES data [146, 147, 148]. The electron self-energy at the Fermi crossing point in the superconducting state can be expressed as $\Sigma(k_F, \omega) = -i\Gamma_1 + \frac{\Delta^2}{\omega + i\Gamma_0}$, where Γ_1 is the single particle scattering rate, Γ_0 is related to the inverse pair lifetime, and Δ represents the gap at the Fermi crossing point. The spectral function is then calculated as $A(k_F, \omega) = \frac{1}{\pi} \frac{\text{Im}\Sigma}{(\omega - \text{Re}\Sigma)^2 + (\text{Im}\Sigma)^2}$. $A(k_F, \omega)$ is then convoluted with a Gaussian function representing the instrumental resolution and fitted to the symmetrized EDCs. The fitted curves are plotted as solid lines in Fig 5.15 (a)-(c). The best fit was achieved

at the antinode where the separation of the two side peaks is the largest, with $\Delta = 31 \pm 2$ meV, $\Gamma_1 = 49 \pm 3$ meV, and negligibly small (less than 1 meV) Γ_0 . Near the node, the fit yields $\Delta \sim 16$ meV and $\Gamma_1 \sim 20$ meV. The very small value of Γ_0 indicates that the gap at the antinode is associated with pairs which have an extremely long lifetime in the superconducting state. Figure 5.15 (d) shows the temperature dependence of the superconducting gap. It shows that the gap size gradually shrinks as the temperature near T_c for all of the three FS cuts. The experimental temperature dependence is rather well reproduced by a BCS function. This aspect is in good agreement with the previous estimates, which led to the suggestion that the superconducting pairing strength in the OPT and OD regions is close to a weak-coupling regime [149]. However, it should be noted that the ratio $2\Delta_0/k_B T_c \sim 7$ is considerably larger than the BCS weak-coupling value 3.5.

5.4.3 Band renormalization effects from ARPES data in Bi2223

Electron phonon coupling

This section briefly reviews the consequences of electron-phonon coupling on the electronic structure and spectral properties. Since the coupling to the other bosons - e.g. of magnetic origin - gives similar effects, here I just discuss a coupled electron-phonon system.

In an isotropic system, the electron-phonon part of the self-energy can be well approximated by averaging the electron-phonon coupling function over the Fermi surface. The phonon function then can be modeled by the Eliashberg coupling function $\alpha^2 F(\omega)$, approximated here as a product of a coupling strength α^2 and phonon DOS. A 2D Debye model ($\omega = vq, \omega < \omega_m$) yields $F(\omega) \sim \omega$. The coupling strength is a smooth function of energy and here it is taken as a constant. The often used dimensionless coupling parameter λ , which appears e.g. in the electrical resistivity, is defined as

$$\lambda = 2 \int_0^{\omega_m} \frac{\alpha^2 F(\omega')}{\omega'} d\omega'. \quad (5.2)$$

The experimental value of λ is obtained from photoemission data either as the renormalization factor of the band dispersion at the Fermi energy or, equivalently, from the temperature dependence of the spectral linewidth at the FS. Equation 5.2 can be further evaluated as $\alpha^2 F(\omega') = \lambda \omega' / (2\omega_m)$ for $\omega < \omega_m$ and zero otherwise.

The self energy of a 2D Debye model is displayed in Fig. 5.16 [107]. In the limit $\omega \rightarrow 0$, the real part shows a linear dependence with slope $-\lambda$ and vanishes at the Fermi level. At energies higher than the Debye energy, the real part decreases to zero, while the imaginary part remains constant. In the limit $\omega \rightarrow 0$ the imaginary part of the self-energy is proportional to ω^2 , i.e. it has the same functional dependence as the Coulomb term in a Fermi liquid. The strongest influence of the electron-phonon coupling on the structure of the spectral function is

then confined to a small energy region of the order of ω_m around the Fermi energy. At $T > 0$ K, the real part of the self-energy is flattened and the imaginary part of the self-energy at $\omega = 0$ has term increasing with energy (Fig. 5.17).

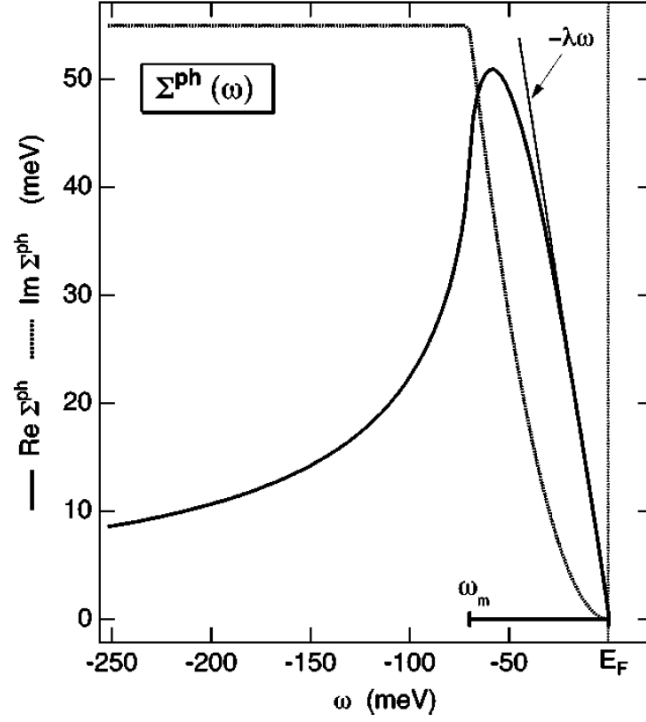


Figure 5.16: Self-energy of the coupled electron-phonon system using a Debye model. Real and imaginary parts are plotted as solid and dashed thick lines, respectively. The real part can be linearized close to $\omega=0$ with slope $-\lambda\omega$, as indicated by the thin line. The phonon band width ω_{max} is indicated. This figure is from Ref.[107].

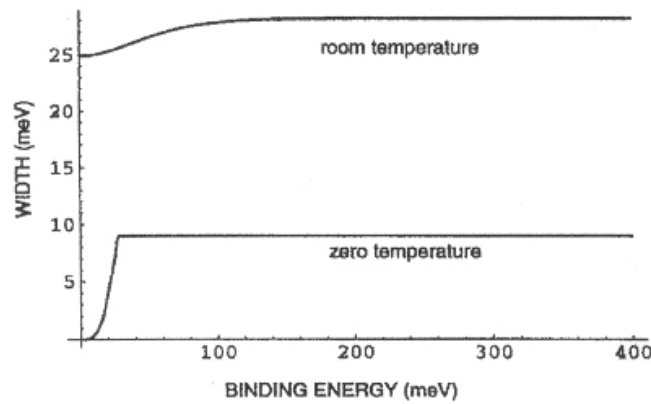


Figure 5.17: The Debye model prediction for the imaginary part of the self-energy at $T > 0$ K. (From [7])

Figure 5.18 (a) shows the quasiparticle dispersion of a Be(0001) surface state for the ΓM and ΓK directions in the BZ [150]. The thin solid line is the calculated dispersion $E(k)$ in the absence of electron-electron interaction. The thick solid line near k_F is the calculated quasiparticle dispersion renormalized by electron-phonon coupling. It is obvious that for $E \leq \hbar\omega_m$ the slope of the band dispersion is reduced, as compared to that of $E \geq \hbar\omega_m$. This slope variation in the dispersion at ω_m is the famous "kink" [151], which has been extensively discussed in the context of HTSC as a key feature for the understanding of the coupling mechanism in these compounds [152, 153, 154]. Figure 5.18 (b) shows a typical kink in Bi2223 along the nodal direction.

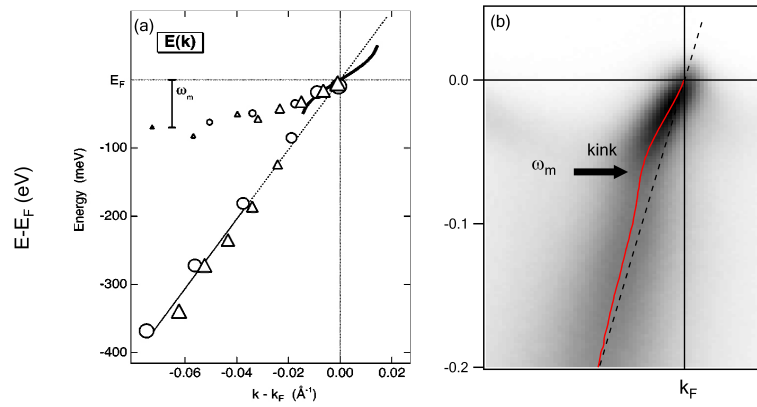


Figure 5.18: Renormalization of the band dispersion from a Be(0001) surface state. (a) Experimental band dispersion of the peak maxima along ΓM (circles) and ΓK (triangles) (from Ref. [150]). (b) ARPES intensity map of OPT Bi2223 measured at $T=12$ K along the nodal direction. The red solid line is obtained from a Lorentzian fitting of the MDCs. The black dashed line is the bare band dispersion. The arrow indicates the maximum phonon energy, or the Debye energy.

The low energy kink

As discussed above the spectral function measured by ARPES also contains, besides the electron dispersion, information of the electron self energy, $\Sigma(k, \omega) = \text{Re} \Sigma(k, \omega) + i \text{Im} \Sigma(k, \omega)$. Its real and imaginary parts are related, respectively, to the energy renormalization with respect to the bare band energy, and the finite life time of the QPs in the interacting system. This information is clearly extremely important to understand the properties of a many-body system. In Chap. 3 I have presented the procedure used to extract the real and imaginary parts of the self-energy from the ARPES data.

The observation of the kink behavior by ARPES [152, 153, 154, 155] has drawn a lot of attention from the high T_c cuprates community. Some of the work concentrated on the kink along the nodal direction $(0,0)-(\pi,\pi)$, where the d -wave superconducting gap is zero. This

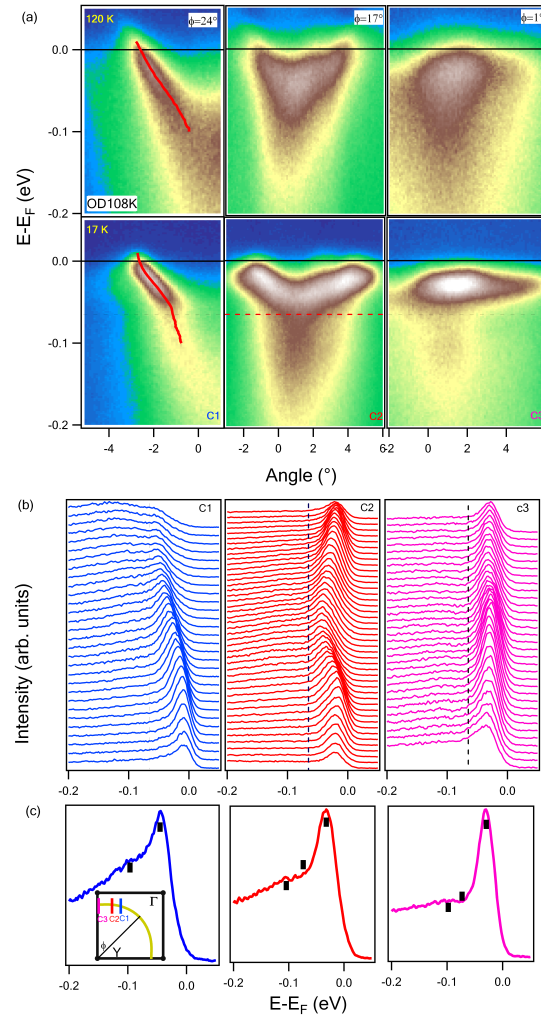


Figure 5.19: (a) ARPES intensity plots of the normal (120 K) and superconducting state (17 K) from cut1 (24° away from antinode) to cut3 (antinode). The solid lines are the Lorentzian fitting from MDC dispersion. (b) Corresponding EDCs in the superconducting states with the dashed lines indicating the kink position. (c) The enlarged EDCs in the superconducting state ($T=17$ K) shown in (b) in order to highlight the typical structure at the kink position. The inset schematic the measured positions in FS.

feature is present in various hole doped cuprates, including Bi2201, Bi2212, Bi2223, LSCO, and it occurs at a similar energy scale (in the range of 50-70 meV). In addition this kink is present both below and above T_c and over the entire doping range [155]. Recently, a kink was found at ~ 40 meV in the antinodal region $-(\pi, 0)$, where the d -wave gap has a maximum. This feature could be identified in Bi2212 [156, 157, 158] in high resolution data which could clearly resolve the bi-layer splitting. The nature of the boson at the origin of the kink is still hotly debated, with two camps favoring either a phonon [152] or a magnon [153, 154]. So far, most of the studies on kinks concentrated on single- and double-layer BSCCO. Few results have been reported on the tri-layer compounds Bi2223 [144, 159, 160]. Some of them [144, 160]

argue that the antinodal kink in the superconducting state is due to a magnetic resonance mode, distinct from that of the nodal kink. Lee *et al.* [159] has proposed the coupling to multiple bosonic modes, instead of just one single mode. Evidence in favor of this proposal has come from data on Bi2212 [161], where new kink energy scales are found around 115 meV and 150 meV.

Gap and kink in the SC and normal state

The ARPES intensity maps of an OD Bi2223 sample measured along cut1 (24° away from antinode) to cut3 (antinode) in the BZ are shown in Fig. 5.19. They reveal noticeable differences between the normal (120 K) and the superconducting (17 K) state. In cut1 a kink around 62 meV in the band dispersion derived from the MDC analysis is observed in both the normal and the superconducting states. Note that the kink is more prominent in the superconducting state. Around the kink energy scale the EDCs in the superconducting state evolve into a two-peak line shape (Fig. 5.19 (c) left), consistent with the coupling with a bosonic mode scenario. In addition, the EDCs in the antinode region show a typical peak-dip-hump structure in the superconducting state (Fig. 5.19 (c) right). The kink is not observed in the normal state in the antinodal region, where the band dispersion is smooth. The momentum and temperature dependence of the kink feature is quite similar to that found in Bi2212 [152]. Further evidence for an electron-boson coupling is found in an OPT 110K sample. This sample exhibits the same kink energy scale from the near nodal to near antinodal region (Fig. 5.20), but the

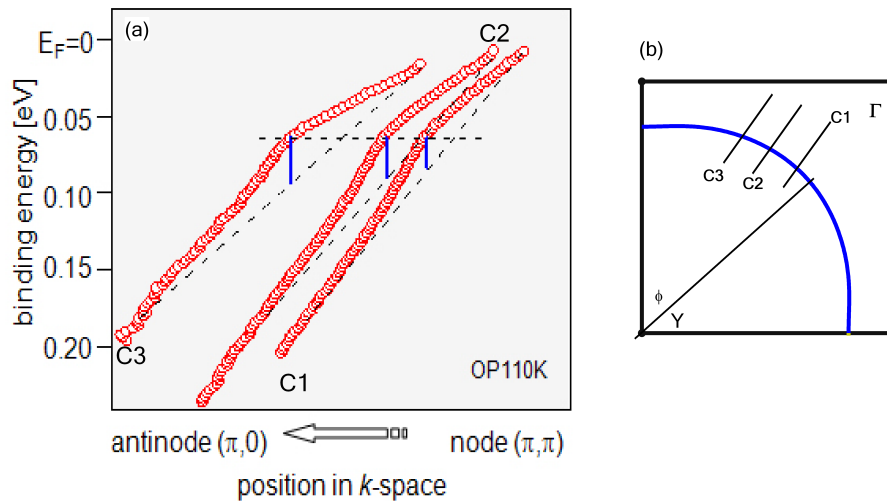


Figure 5.20: (a) Kink of OPT 110K sample from near nodal to antinodal region. (b) The corresponding measured cut position C1, C2 and C3 in the first BZ.

kink appears stronger at the near antinode region than that at the node. Furthermore, in the superconducting state the dip energy scale in the peak-dip-hump structure near the antinodal region (cut3) is at roughly the same position as the kink position in cut1 and cut2, which is all around 70 meV in good agreement with previous ARPES studies on Bi2223 [143, 159]. In a strong-coupling BCS scenario, the kink is expected to appear at an energy $\Omega + \Delta$, where Ω is the energy of the boson mode responsible for pairing and Δ is the maximum of the d -way symmetry gap [162, 163]. The ARPES data therefore suggest that the band renormalization in Bi2223 in the superconducting state is induced – at least primarily – by the same mode over the whole Fermi surface.

The high energy kink in Bi2223

Besides the well-known low energy kink at ~ 50 – 70 meV discussed above, recently another high energy anomaly has been identified in the dispersion of HTSC cuprate materials at a considerably larger energy of 300–400 meV. Understanding the role of different energy scales in the cuprates is probably the key to understand their physical properties. It is therefore a challenge to clarify the origin of this high energy kink. At the present stage, it is still unclear whether it can be attributed to a specific many-body effect [161, 164, 165, 166, 167, 168]. Possible proposed interpretations include a 1D-like spinon and holon separation [165], a coherence-incoherence crossover [167], itinerant spin fluctuations [164], strong local spin correlations [166], a new form of electron coupling [161], but also more mundane matrix elements effects [168]. Interestingly, no such high energy band renormalization effect has been reported so far in the tri-layer compound Bi2223.

Figure 5.21 (a)–(c) shows an ARPES intensity map for a slightly OD Bi2223 superconductor ($T_c = 108$ K), measured parallel to the $\Gamma(0,0)$ – $Y(\pi,\pi)$ direction (see inset) at a temperature of 105 K. The corresponding QP energies extracted from lorentzian fits of the MDCs are shown in Fig. 5.21(d). One obvious kink in the dispersion is observed at ~ 70 meV. This is the low energy kink discussed before. The real part of the electron self-energy can be extracted from the experimentally observed and the bare band dispersion. The latter is by definition unknown. It can be guessed in various ways, all of them somewhat arbitrary [169, 170]. In order to determine the – energy, momentum, and temperature dependent – features of the real part of the self-energy, a smooth bare band dispersion must be defined, within a small energy window near the Fermi energy. A simple linear dispersion, parabolic dispersion or the results of a tight-binding calculation have been used [169]. The fine structure features then manifest themselves either as peaks or slope changes in the difference between the experimental and the bare dispersion [170]. As shown in Fig. 5.21(d), I chose a straight line (the red solid line) as a empirical bare band, connecting the Fermi level crossing with the band at -0.4 eV, as was done in the case of Bi2212 [161]. The corresponding effective real part of the self-energy,

which represents the band renormalization, is shown in Fig. 5.22.

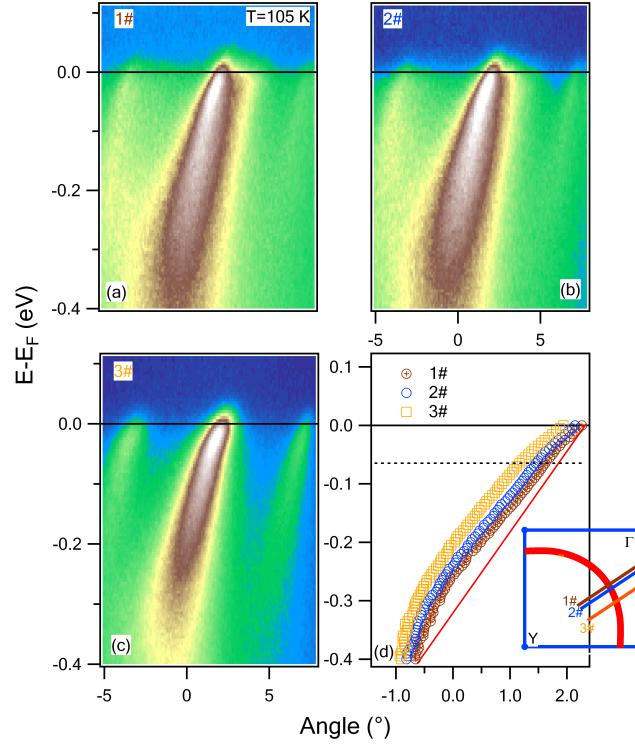


Figure 5.21: (a)-(c) Raw ARPES intensity maps of an OD Bi2223 sample along cuts parallel to the $\Gamma(0,0)$ - $Y(\pi,\pi)$ direction (inset shows the position of each cut in the BZ) at 105 K. (d) Nodal dispersion extracted from (a) by Lorentzian fits of the MDCs. The solid line connecting from Fermi energy to -0.4 eV is the bare band used to determine the real part of the self-energy.

There are several curvature changes in the real part of the effective self-energy and in the corresponding MDC line widths. The most pronounced feature is a peak at ~ 250 meV, at an energy which coincides with the energy of previously reported high energy kinks [164, 165, 166, 167, 168]. Another prominent feature is seen at ~ 70 meV, the common kink energy scale in the dispersion in the high T_c cuprates. In addition, two new weaker features can be identified, at ~ 35 meV and at ~ 110 meV. The lower energy structure at ~ 35 meV, considered as a “subkink”, has also been identified in the normal state OP Bi2223 [159]. This subkink would not exist if the electrons coupled only to a single mode near 70 meV, indicating the renormalization effects in Bi2223 system involve several bosonic modes. The high energy feature at ~ 110 meV can be caused neither by the coupling with a single phonon (maximum phonon energy ~ 90 meV) [171] nor with the magnetic resonance mode (42 meV) [172].

At least two interpretations can be proposed for the lower and higher energy features in the electron self energy. One is the electron coupling to multiple phonons. Recently, renor-

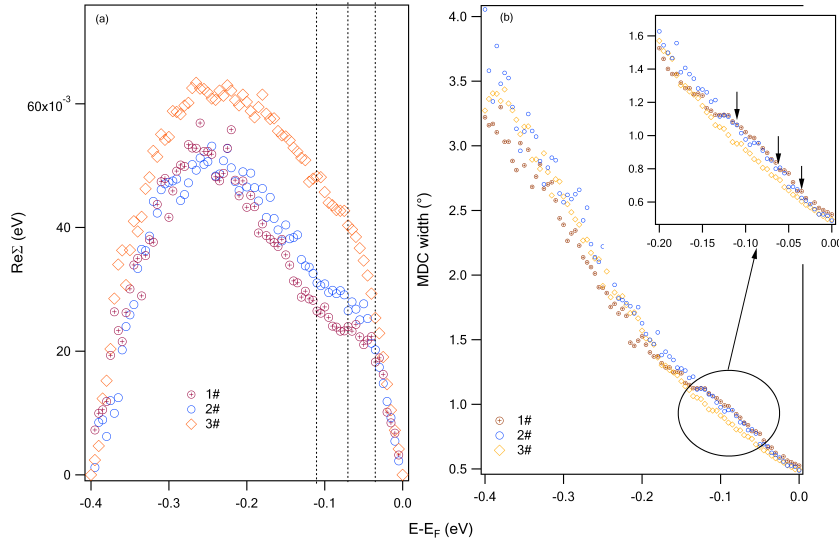


Figure 5.22: Real part of the electron self-energy obtained by subtracting a linear dispersion from the experimental ARPES dispersion. The three dotted lines in (a) indicate the three kink energies at ~ 35 meV, 70 meV and 110 meV. (b) The corresponding three MDCs line widths in (a). The three arrows marks the same fine structures as in (a). The inset is an enlarged view of the low energy region.

malization features induced by the multiple mode coupling have been found in Bi2201 [173], Bi2212 [174], Bi2223 [159] and LSCO [170]. The second considers the opening of the superconducting gap. The low energy structure in the normal state is expected to be moved to higher energy position when the system enters into the superconducting state. In the slightly OD Bi2223, the maximum d -wave superconducting gap is ~ 31 meV. It does happen that the energy lower kink 35 meV plus the gap size is almost equal to the kink energy at ~ 70 meV. Similarly, the ~ 70 meV mode would shift to an even higher energy ~ 110 meV. Lee *et al.* [159] found the same shift from 35 meV to 70 meV in Bi2223 while missing the high energy mode, and Zhang *et al.* [161] revealed a shift from 70 meV to 110 meV but could not explain another high energy structure at 150 meV. Further data on the temperature evolution of the kink structure would be necessary to finally clarify this important spectral feature in Bi2223.

5.5 ARPES on thin film $\text{Bi}_2\text{Sr}_{2-x}\text{La}_x\text{CuO}_6$

Novel materials are not always available as single crystals and in the large sizes required by ARPES experiments. Often, preparing atomically clean stoichiometric surfaces of a bulk single crystal may also be difficult or even impossible. Thin film samples may offer a solution to these difficulties, since phases that are not stable, or that are difficult to prepare as bulk materials, may be grown by epitaxy on an appropriate substrate. An *in-situ* preparation also yields pristine surfaces which do not require further special preparation (e.g. cleaving). Thin film

samples also offer the interesting possibility of introducing strain in the structure, which may have a dramatic influence on the electronic properties of TM oxides [175]. Our ARPES apparatus was specifically designed to allow docking of a pulsed-laser-deposition (PLD) thin film growth facility (operated by D. Ariosia, D. Pavuna, IPMC-EPFL). The films can be transferred without breaking the vacuum immediately after growth, or after an appropriate annealing in oxygen atmosphere, to the ARPES preparation chamber, and from there to the high-resolution spectrometer. During my thesis I have been able to measure Bi2210 thin film samples grown by this facility.

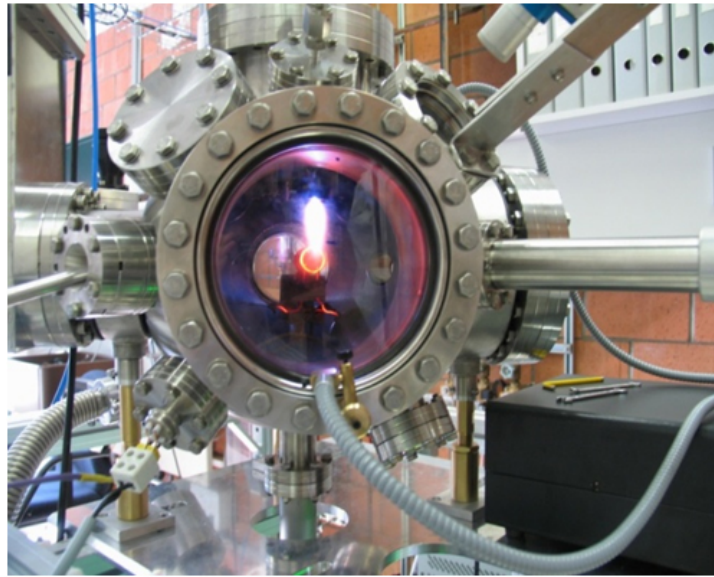


Figure 5.23: Laser plume during the interaction between laser and target.

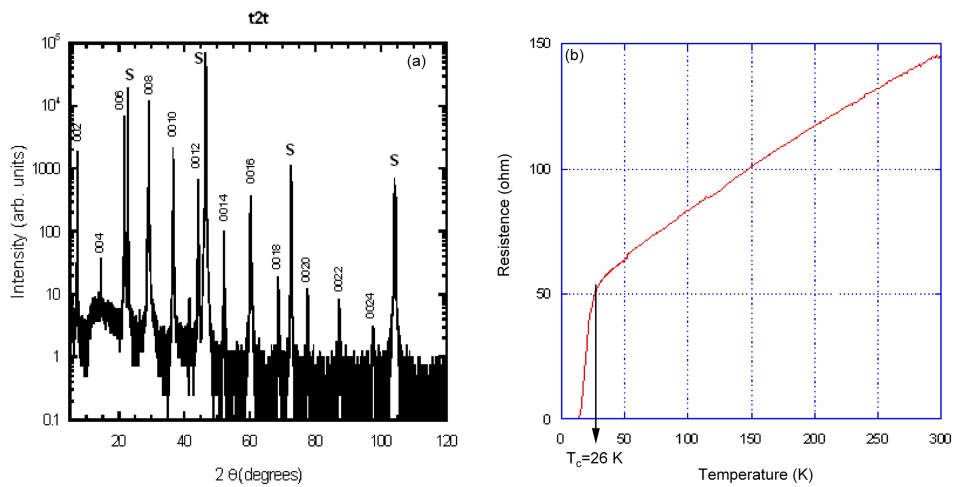


Figure 5.24: (a) XRD and (b) resistivity of Bi2201 thin films.

Before performing the photoemission measurement, it is quite important to optimize the growth condition to get pure single-phase La doped Bi-2201 thin films. The stoichiometric $\text{Bi}_2\text{Sr}_{2-x}\text{La}_x\text{CuO}_6$ ($x=0.3$) thin films were grown by PLD (Fig. 5.23) on oriented (100) SrTiO_3 substrates with a pulsed yttrium aluminum garnet laser at 266 nm, 100 mJ pulses, and 2 Hz repetition rate. The films were annealed *in situ* at 700 °C for 1 hour in 1 atm of O_2 . The thickness of the thin films was about 100 nm. X-Ray diffraction (XRD) (Fig. 5.24 (a)) showed that the films only contained the Bi-2201 phase. From resistivity vs. temperature measurement the critical temperature $T_c=26$ K was determined (Fig. 5.24 (b)), corresponding to slightly underdoped samples.

In order to prevent the contamination during the transfer, the PLD growth chamber is directly connected to the UHV ARPES apparatus, as illustrated in Fig. 5.25. The as-grown samples are directly transferred into the photoemission chamber where the spectroscopic measurements are performed. We have succeeded in measuring the band dispersions of Bi2201 thin films along the high symmetric directions ΓM (from (0,0) to $(\pi,0)$) and ΓY (from (0,0) to (π,π)), respectively. It is important to mention that the life-time of one sample in the photoemission chamber varied from 30 to 45 minutes. However, the surface quality could be recovered by reannealing the thin films at 700 °C in 1 atm of O_2 for 1 hour.

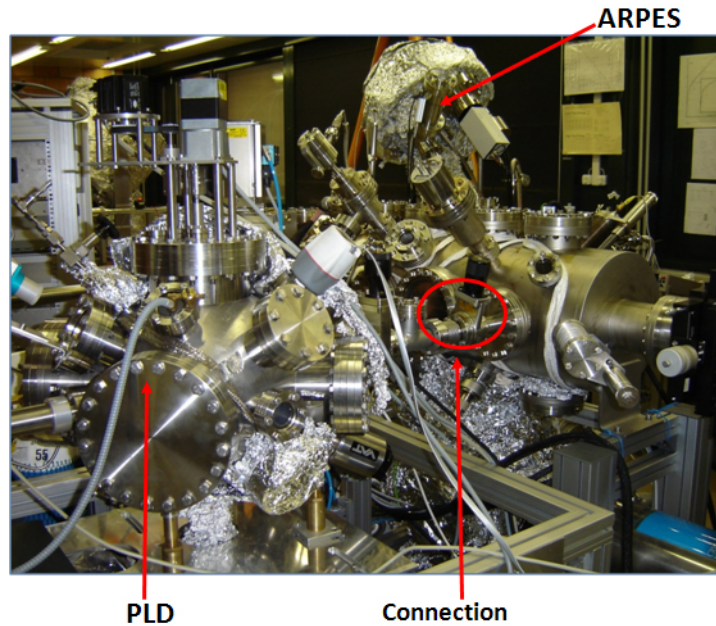


Figure 5.25: PLD chamber connected with the ARPES chamber in order to measure the Bi2201 thin films *in situ*.

Before the photoemission measurement, the orientation of the sample was measured by low-energy electron diffraction (LEED). Figure 5.26 shows a typical LEED pattern, corresponding to a well-ordered (001) surface. The extra spots are due to the 5×1 modulation [176, 177]

along the a axis, and to the presence of two domains at 90° . Unfortunately, twinning cannot be removed. This is a major complication for the determination of the band structure and especially of the Fermi surface, due to the umklapp structures. A partial substitution of Bi by Pb atoms should remove the modulation, and solve the problem, since the 90° twinning by itself has a negligible effect on the ARPES spectra. Unfortunately, this was not possible during my thesis.

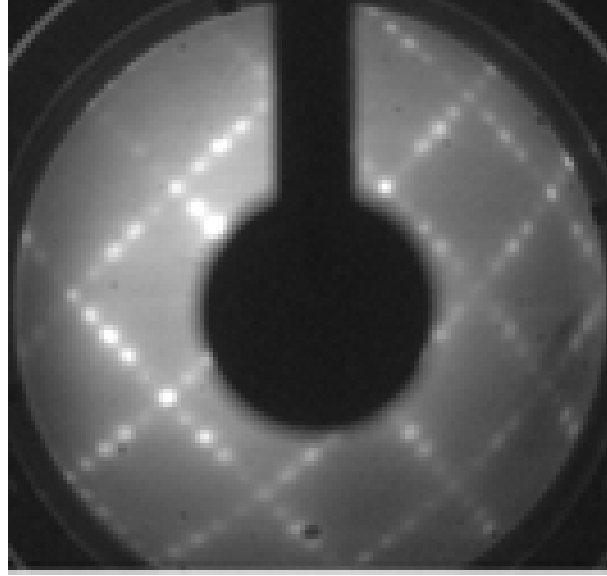


Figure 5.26: LEED image of the La doped Bi2201 thin film grown on a STO (100) substrate, presenting a 5×1 twin domains.

As shown in Fig. 5.27, the ARPES data measured in parallel cuts perpendicular to the antinodal $(0,0)$ to $(\pi,0)$ direction clearly illustrate the evolution of the hybrid Cu-O conduction band, with a shallow minimum around the M $(\pi,0)$ point. The corresponding spectra along the $(0,0)$ to $(\pi,0)$ direction reveal a well resolved dispersing quasiparticle peak. Fig. 5.27 (c) shows the Fermi surface contour along ΓM . The solid lines are from a 2D tight-binding (TB) model:

$$E(k) = t_0 - 2t_1(\cos k_x + \cos k_y) + 4t_2 \cos k_x \cos k_y. \quad (5.3)$$

which can well represent the main band. The dashed lines represent the umklapp bands which are obtained by shifting the main band by the superlattice vector $Q = (\pm 0.21\pi, \pm 0.21\pi)$. All these thin films data are comparable to synchrotron data from cleaved single crystal surfaces of the same material. They confirm the good quality of the films, and the viability of the in-situ preparation.

Future work will be focused on eliminating the superstructure and/or the in-plane twinning, which unnecessarily complicates the ARPES analysis. When that milestone is achieved, changes in the band dispersion and in the spectral line shape in strained samples, and in sam-

ples with varying doping levels, will be investigated. Subsequently, thin films of the Bi-2212 and Bi-2223 phases, characterized by two and respectively three CuO planes in the structure, will be explored, and compared with ARPES results from bulk samples.

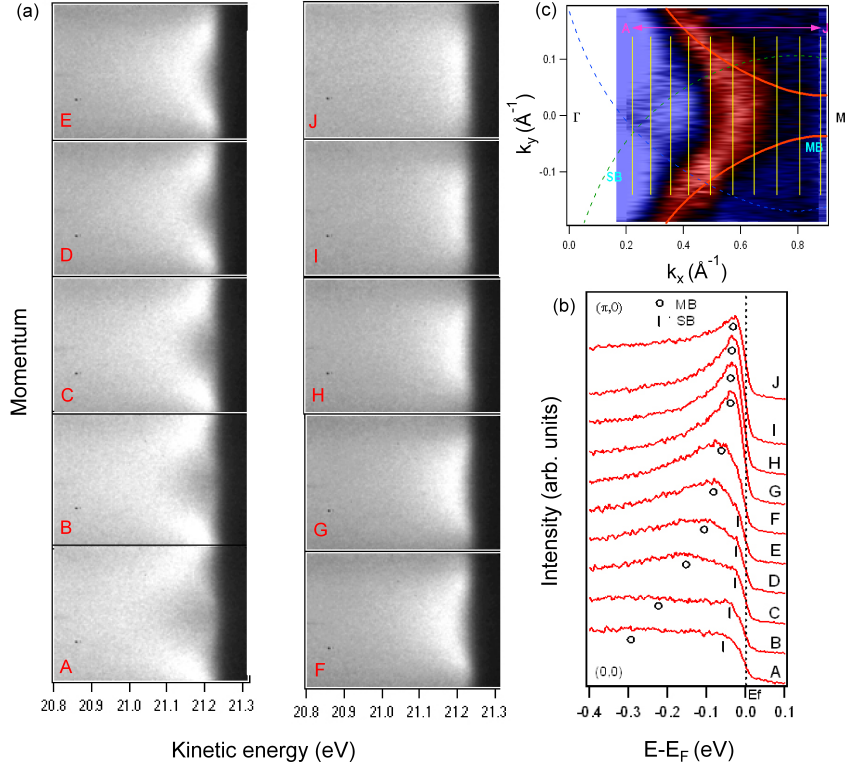


Figure 5.27: (a) ARPES intensity maps from Γ to M point at $T=70$ K. The lines A-J correspond to cuts in (c). (b) The corresponding EDCs extracted from the ARPES map in (a). (c) The corresponding Fermi surface.

Chapter 6

RIXS experiment on insulating and superconducting cuprates

6.1 General information on RIXS

ARPES has been used throughout this work because it provides a very direct and selective view of the electronic structure, namely of the one-electron *quasiparticles* excitations (the hole spectral function). Nevertheless, complementary information on the electronic states can be gained from other spectroscopic techniques. In this section I present the results of resonant inelastic x-ray scattering (RIXS) experiments on cuprates which I have been involved in during the course of my thesis. Thanks to the high resolution obtainable at a recently developed experimental set-up, these results shed new light on the electronic structure of these materials.

RIXS is a novel spectroscopic technique and – by contrast with ARPES – a bulk sensitive probe of neutral electronic and magnetic excitations in strongly correlated electron systems, in particular in the high T_c superconductors. The resonant nature of the RIXS process is schematically illustrated in Fig. 6.1. An incident photon, with energy $h\nu_{in}$ tuned to a specific absorption threshold, excites an electron from a core level into the valence shell. This intermediate state is identical to the final state of an x-ray absorption (XAS) experiment. The excited state can then decay radiatively by emitting a photon with energy $h\nu_{out}$. The final state of the RIXS process can be the same ground state, or one of the neutral excited states of the system. In the former case, the energy of the emitted photon coincides with that of the incident photon: the process is elastic. In the latter, part of the energy of the incident photon is left in the system, and the scattering process is inelastic. The energy loss – the difference between the energies of the incoming and emitted photon – directly yields the energy of the excited states. At resonance, the separation into two subsequent steps is actually arbitrary, and the whole process should be

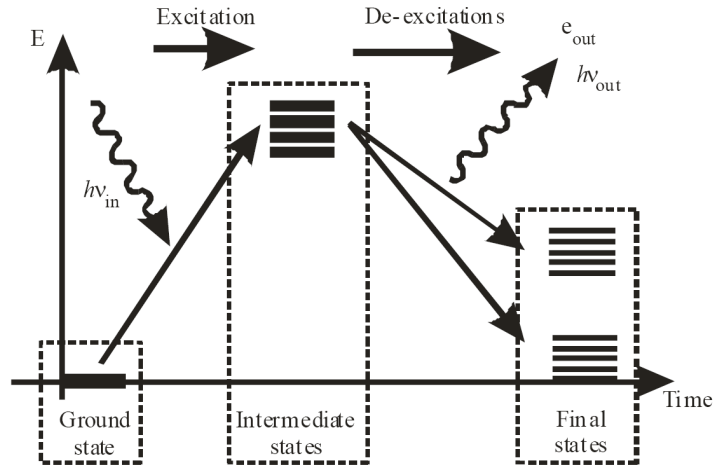


Figure 6.1: Schematic illustration of a RIXS process for a Cu^{2+} (d^9) ion, in a total energy picture. The absorption of the incident photon causes the transition from the ground state to the intermediate state. A consequent transition from the intermediate state to the final state occurs with the emission of a photon. (From [178])

described as a coherent second-order (two photons are involved) optical transition from the initial to the final state, with distinct selection rules. Its differential cross section is therefore distinct, and in some way richer, than that of first-order processes like XAS or photoemission. RIXS is the x-ray and resonant analog of conventional Raman spectroscopy, with important peculiarities which result from the presence of the core hole in the intermediate state. Indeed the core hole guarantees chemical but also orbital selectivity, via the dipole selection rules in both absorption and emission steps [179, 180]. However, since the final state has no core hole, the RIXS spectral function is not affected by the large lifetime broadening which affects other core hole spectroscopies. Being a photon in – photon out technique RIXS has also some interesting advantages over photoemission: i) its probing depth is orders of magnitude larger, and therefore RIXS is rather insensitive to surface conditions; ii) RIXS is not affected by charging effects, and it is therefore an ideal probe of insulators, which are hard to measure by ARPES.

For all its advantages, it should nevertheless be clear that RIXS cannot entirely replace ARPES. RIXS yields information on neutral – electron-hole or collective – excitations, i.e. on a more complex two-particle spectral function than the one-particle ARPES spectral function. It is therefore closer to optical spectroscopy although, unlike optics (or Raman), it is not limited to zero-momentum excitations. From a more technical point of view, the efficiency of the RIXS process is weaker than that of ARPES by many orders of magnitude. RIXS therefore requires the extremely high brilliance of undulator sources at 3rd-generation synchrotrons. The intrinsically lower signal, and the much larger photon energies of RIXS, sets practical limits on the ultimate experimental resolution. The world-best soft x-ray RIXS instrument is the SAXES

spectrometer of the Swiss Light Source (SLS) (Fig. 6.2), designed and built in the framework of an international collaboration between the SLS, the spectroscopy group of Politecnico di Milano, and our laboratory at ICMP-EPFL. The state-of-the-art resolution of SAXES is $\Delta E = 120$ meV at a photon energy of 930 eV, corresponding to the Cu L_3 ($2p \rightarrow 3d$) edge. This is still more than one order of magnitude worse than the energy resolution of the best ARPES instruments. Nevertheless, the large improvement in the resolving power (5-10 times) offered by SAXES over previous instruments has already revolutionized the technique, and revealed new important aspects of the electronic structure of TM materials [181, 182, 183, 184]. ARPES-like high-resolution spectroscopy, namely gap spectroscopy in the superconductors, is not a realistic option for RIXS at present, but it may become possible in the future if new spectrometers which are now in the design stage finally succeed in pushing the resolution to the 20-30 meV level.

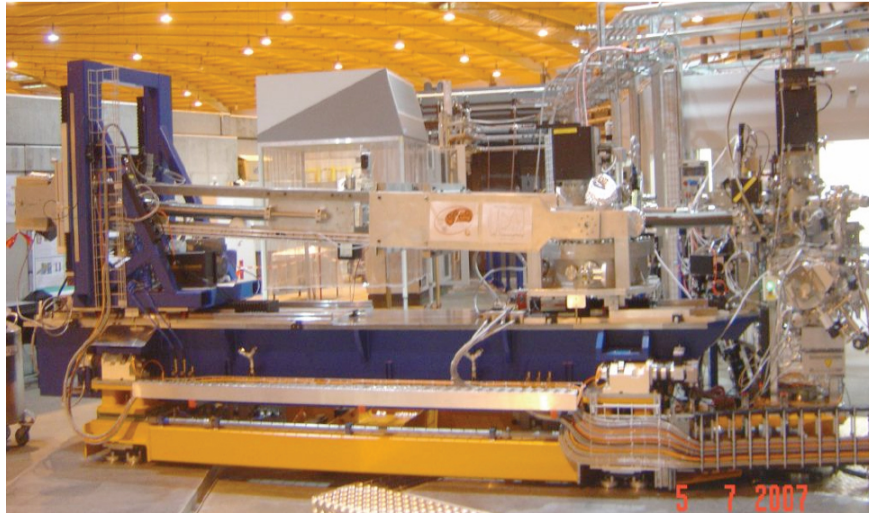


Figure 6.2: The high-resolution RIXS Super Advanced X-ray Emission Spectrometer (SAXES) end station, and its rotating platform for momentum-dependent measurements, at the ADRESS beamline of the Swiss Light Source.

RIXS is an effective probe of elementary electron-hole excitations, such as dd (crystal field) excitations in TM compounds. This is shown schematically in Fig. 6.3. These excitations are not accessible as such by optical experiments because $\Delta l = 0$ transitions are dipole forbidden (they become weakly optically allowed when a phonon is also involved). However RIXS is a two-photon process and the more general $\Delta l = 0, \pm 1, \pm 2$ selection rules apply. Besides probing final states that do not change the number of $3d$ electrons in transition metal (TM) compounds, RIXS can also detect the charge fluctuations that define the transport and many other properties of TM oxides. In cuprates materials these final states have $d^{10}\underline{L}$ character (\underline{L} is a hole in the oxygen $2p$ band) and represent the $d^n \rightarrow d^{n+1}\underline{L}$ transitions which define

the fundamental charge-transfer (CT) energy gap [185, 186, 187]. More recently it has been recognized that RIXS is also a powerful technique for probing collective magnetic excitations – magnons – in magnetic ordered systems [188]. In this sense RIXS is complementary to inelastic neutron scattering (INS), the traditional technique to probe spin waves, but with much less stringent requirement on the size of the sample.

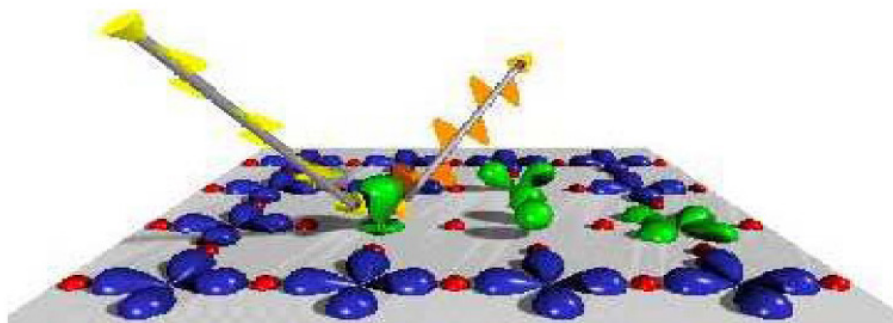


Figure 6.3: Artist's view of a dd excitation in the CuO_2 plane of a cuprate. The hole is scattered from the $x^2 - y^2$ to the $3z^2 - r^2$ state in a RIXS process.

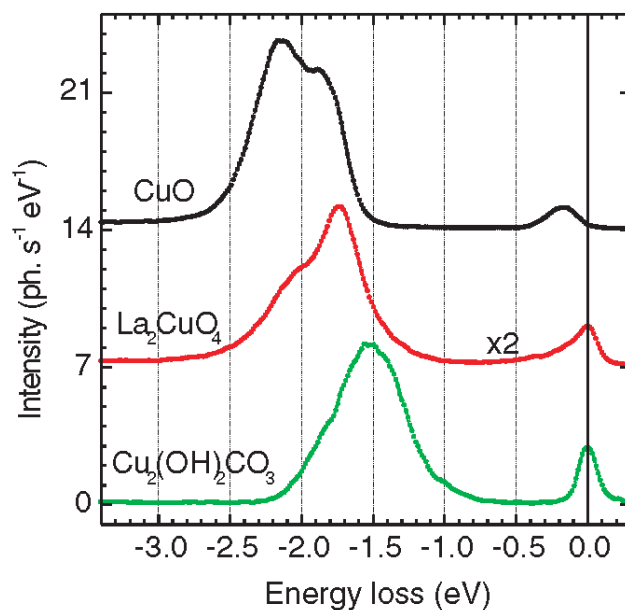


Figure 6.4: Cu L_3 RIXS spectra of three different Cu^{2+} compounds. The dd excitations are different, reflecting different local symmetries and crystal field parameters [189].

In summary, RIXS can provide information on the local configuration of a TM ion and on the hybridization between the TM ion and the oxygen ligands in TM oxides, namely in the superconducting cuprates, which could not be gained by any other conventional spectroscopy. The sensitivity of RIXS to the local environment of a Cu^{2+} ion to the symmetry of its local

environment, and to the strength of the crystal (or ligand) field, is well illustrated by the SAXES data from three different Cu oxide samples, in Fig. 6.4. This sensitivity, and the ability of RIXS to measure the momentum dependence of collective magnetic excitations, are exploited in the original measurements presented below. They concern the typical 2D AFM insulating cuprate $\text{Sr}_2\text{CuO}_2\text{Cl}_2$, and optimally doped samples of the Bi-2212 and Bi-2223 superconductors.

6.2 RIXS on $\text{Sr}_2\text{CuO}_2\text{Cl}_2$

In this section I present some recent RIXS data on $\text{Sr}_2\text{CuO}_2\text{Cl}_2$ (SCOC). A more detailed account can be found in Ref. [190].

SCOC is an antiferromagnetic (AFM) Mott-insulator single-layer parent compound of the high- T_c superconducting (SC) materials. It orders below the Néel temperature $T_N=256$ K, with reduced Cu moments of $0.34 \mu_B$ lying within the CuO_2 planes and aligned along the (110) direction, at 45° from the Cu–O–Cu bond direction. SCOC is isostructural to the high-temperature tetragonal phase of La_2CuO_4 (LCO), with La replaced by Sr and the apical oxygen ions of the CuO_6 octahedra replaced by Cl. The structure is illustrated in Figure 6.5 where the CuO_2 planes and the apical atoms co-ordination are depicted. Unlike LCO, SCOC shows no orthorhombic distortion and keeps its trigonal structure down to at least 10 K. The distance between adjacent CuO_2 planes is considerably larger (18 %) than for LCO. Thus, SCOC has been considered an almost ideal realization of an $S=1/2$ 2D square-lattice Heisenberg AFM.

Magnetic excitations in SCOC have been studied by optical conductivity, Raman spectroscopy, and by inelastic neutrons scattering (INS). Both optics and Raman data show a strong spectral feature at ~ 0.35 eV [191] which is interpreted as a two-magnon (Raman) or a two-magnon plus phonon (optics) excitation [192]. Both techniques are limited to zero momentum transfer ($Q=0$) and the spectroscopic information essentially reflects the two-magnon DOS at the magnetic zone boundary. The observed features have an energy, renormalized by magnon-magnon interaction, of ~ 2.7 times the AFM exchange energy J , as predicted by theory. Both Raman and optics are blind to single magnon excitations, which are optically forbidden spin-flip ($\Delta S = 1$) excitations. INS is the default technique to measure the magnon dispersion. In the case of cuprates, however, the large energy scale set by J , and the difficulty of obtaining large single crystals represent major experimental obstacles. Only recently it has been possible to map the full magnon dispersion in a cuprate, namely in LCO [193]. A remarkable aspect of those data is the 20 meV difference between the energies of the magnon at the $(\pi, 0)$ and $(\pi/2, \pi/2)$ points of k space. That observation has raised considerable interest, because the simple Heisenberg model with nearest-neighbor exchange does not predict a dispersion along the boundary of the AFM Brillouin zone (BZ). Therefore the neutron data suggest that further-neighbor magnetic interactions cannot be neglected. For the reasons mentioned above, SCOC

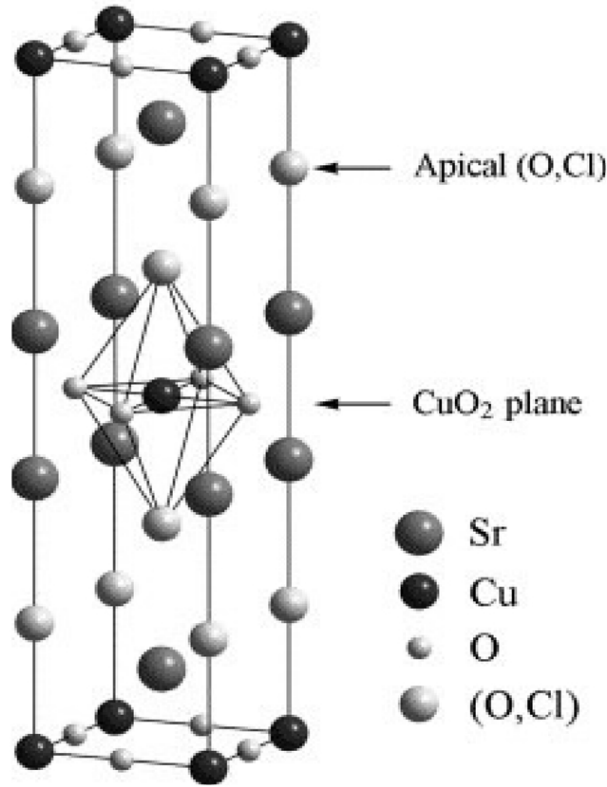


Figure 6.5: Schematic view of the crystal structure of SCOC.

is a "cleaner" system to study the magnon dispersion, but INS measurements of SCOC have so far been limited to low energies, therefore covering only small Q around the ordering vector [194]. It is not possible to conclude from the existing data if long-range magnetic interactions are also important in this paradigmatic material. A positive answer to this question would set new constraints on theoretical models of the electronic structure of cuprates. It is therefore highly desirable to map the magnon dispersion over the whole BZ.

We have performed high resolution Cu L_3 -edge RIXS measurement on SCOC at the SAXES end station of the ADRESS beam line of the SLS. Typical results are presented in Fig. 6.6. Data were collected at an incident photon energy corresponding to the maximum of the Cu L_3 XAS lineshape (inset). The scattering angle was fixed at 130° , but the the projection Q_{\parallel} of the constant scattering vector \mathbf{Q} on the ab plane could be varied by varying the angle between the incident beam and the samples's c -axis. We performed measurements in both σ - and π -geometry (referred to the sample surface) (Fig. 6.6 (a)) by varying the polarization – from linear vertical to linear horizontal – of the incident soft x-ray beam from the undulator source. Fig. 6.6 (b) is an overview of the data measured for π -polarization by varying Q_{\parallel} along the (100) direction. The main spectral feature is the manifold of optically forbidden dd electron-hole excitations at 1.5–2 eV. In an ionic picture they correspond to a Cu d^9 final state where

the hole is in an orbital other than $d_{x^2-y^2}$ [195, 196]. These excitations do not disperse with in the in-plane vector, consistent with their excitonic nature. The lineshape on the other hand varies with the incidence angle, and spectral intensity is progressively transferred between the lowest-lying excitation of $3z^2 - r^2$ character at ~ 1.5 eV to the higher-lying xy , xz , and yz final states. This characteristic angular dependence can be reproduced by a cluster calculation [M. Moretti, preprint].

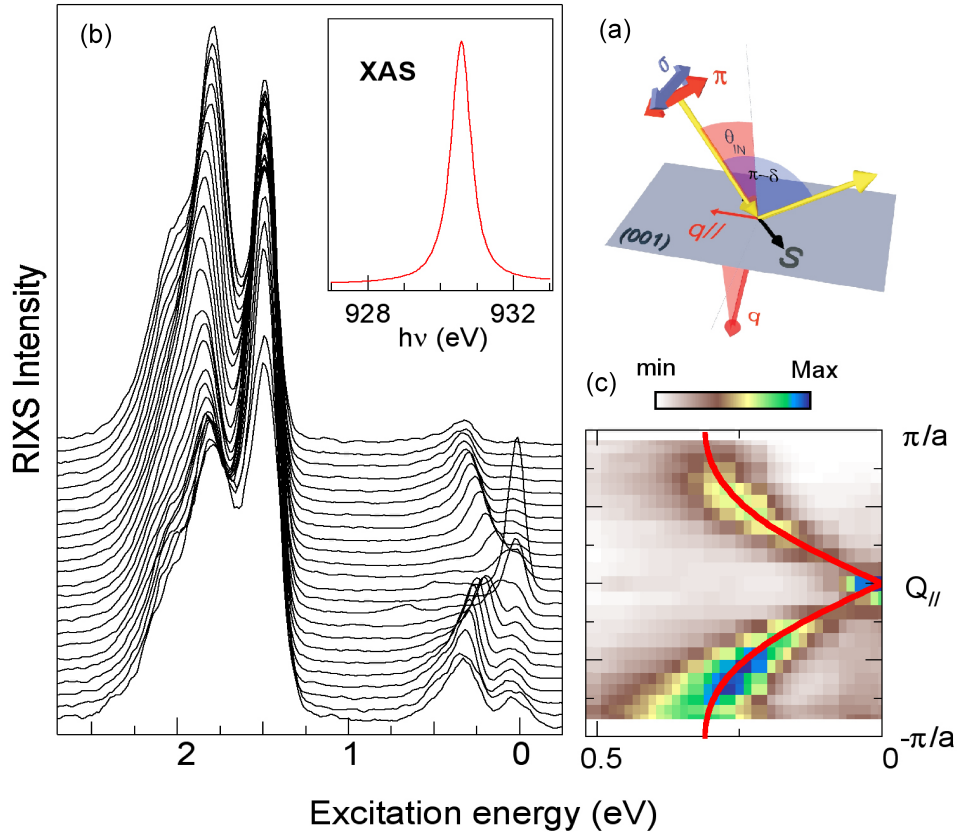


Figure 6.6: (a) Schematics of the scattering geometry. (b) Cu L_3 RIXS spectra of SCOC measured at 15 K along the $(-\pi, 0)$ to $(\pi, 0)$ direction. The incident energy is set at the maximum of the XAS line shape (inset). (c) Intensity map extracted from panel (b). The red line is the calculated spin-wave dispersion for the NN Heisenberg model and $J=130$ meV.

In the 0-1.5 eV energy range, where no electronic excitations are expected, the spectra exhibit a clear loss feature, which disperses symmetrically upwards from $Q_{\parallel}=0$ (Fig. 6.6 (c)). Near the zone boundary spectral weight extends beyond 300 meV, well above the energy of the highest phonon mode in SCOC ($\hbar\omega=70$ meV) [19]. The Q dependence of the maximum of the spectral intensity follows the red line, which is the calculated spin-wave dispersion for the NN Heisenberg model for $J=130$ meV with a uniform (18 %) renormalization by quantum

corrections. This strongly suggests a magnetic origin of this dispersing feature. Interestingly, however, quite some spectral weight is found above the red curve, at energies as high as 0.4–0.5 eV. This signal is associated with the two-magnon continuum, i.e. with final states where two magnons share the transferred momentum and energy.

The single magnon dispersion extracted from the RIXS data is illustrated in Fig. 6.7. The remarkable aspect of this result is the large difference (~ 70 meV) between the magnon energies at the $(\pi, 0)$ and $(\pi/2, \pi/2)$ points on the AFM zone boundary. As for the case of LCO [193] it shows that exchange interactions beyond NN are important for SCOC, and actually larger than in LCO. The data can be satisfactorily reproduced by an extended Heisenberg model with $J=142$ meV, and a ‘ring exchange’ term, which involves 4 Cu spins on a square plaquette, $J_R=89$ meV, considerably larger than $J_R=38$ meV for LCO[193].

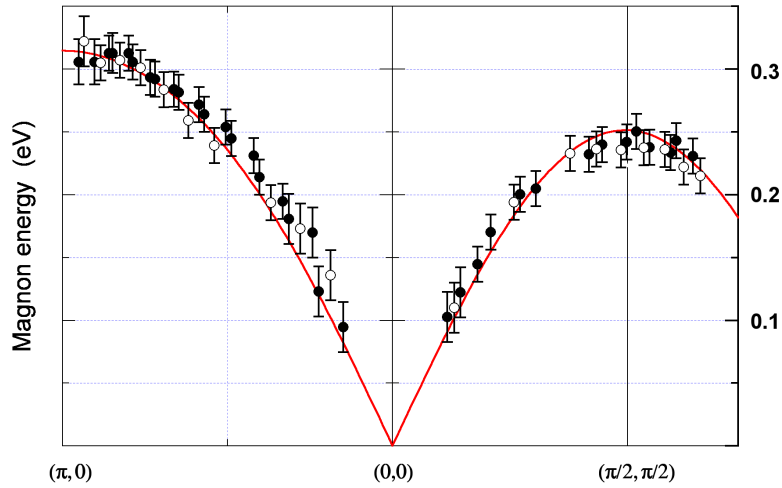


Figure 6.7: Magnon dispersion extracted from the RIXS data.

An interesting and still unexplored aspect of RIXS is the possibility to separate single- and multiple-magnon contributions – with variable $Q \neq 0$ unlike in Raman – by exploiting their different polarization dependent cross sections, or by comparing data from different edges. This is illustrated by Fig. 6.8, where striking difference of the spectral lineshape are found when the incident polarization is changed, for the same transferred momentum. The top panel shows data for the same $Q_{\parallel}=0.58 \text{ \AA}^{-1}$ along the (100) direction, normalized to the same intensity in the two-magnon region for ease of comparison. The π -polarization spectrum shows a strong single-magnon peak, which is strongly reduced in the σ -polarization spectrum, where the single-magnon and the two-magnon contributions are of comparable intensities. The bottom panel compares Cu L_3 edge and O K ($1s \rightarrow 2p$) edge (1s, 530 eV) data, for the same Q_{\parallel} (0.19 \AA^{-1}). The creation of a single magnon ($\Delta S = 1$) is forbidden at the O K edge by

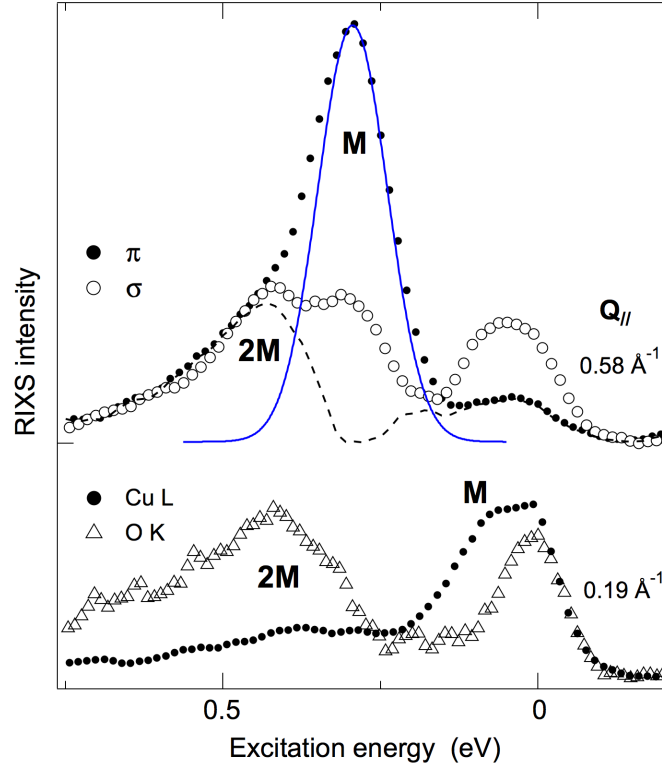


Figure 6.8: (Top) Comparison of Cu L_3 spectra measured for σ and π polarization at the same $Q_{\parallel}=0.58 \text{ \AA}^{-1}$. (Bottom) Comparison of Cu L_3 and O K spectra at the same $Q_{\parallel}=0.19 \text{ \AA}^{-1}$.

angular momentum conservation because, unlike the L_3 edge case, the intermediate $1s$ core-hole state has no spin-orbit interaction, and the spin must be strictly conserved. Therefore the O K RIXS spectrum can only contain two magnons ($\Delta S = 0$) response contains only the two-magnon continuum, which was already suggested by a previous experiment [197], and is now clearly resolved around 0.4 eV for this Q_{\parallel} . By contrast, the L_3 line shape is dominated by the single magnon loss at ~ 0.1 eV. These data indicate that incident polarization can be used to tune the ratio between single- and multi-magnon weight in the measured spectrum.

6.3 RIXS on optimally doped Bi2212 and Bi2223

Spectroscopic data on insulating parent compounds, like those for SCOC discussed above, represent important background knowledge in view of a general theory of cuprate materials. A further crucial step is to understand how the electronic structure of the insulator is modified by doping the CuO_2 planes with holes. In particular, the question to which extent, and in which form, the magnetic excitations survive in the SC part of the phase diagram, is of great relevance for theoretical scenarios which associate the occurrence of SC in the cuprates with persisting magnetic interactions. In this respect, hole-doped SCOC would provide the ‘cleanest’

comparison. Unfortunately, it is very hard to dope holes into SCOC. A partial replacement of divalent Sr by monovalent Na can be achieved in a high-pressure synthesis, but the resulting crystals are very hygroscopic, and it is difficult to select specimens of sufficient size and of sufficiently high crystalline quality for a RIXS experiment. Our attempts in this direction have not been successful so far. In parallel, our group has started a systematic investigation by RIXS of samples of the BSCCO family, which can be grown over a broad range of doping levels, spanning the AFM insulator and the SC phase, from UD to OD. The ultimate goal of this study is to determine the evolution of the local Cu environment – through the changes in the dd excitations – and of the spin dynamics. I present here some preliminary data for optimally doped samples of Bi2212 and Bi2223. All the data shown here were measured at a temperature $T=46$ K, well into their respective SC phases.

Figure 6.9 shows Cu L_3 XAS spectra of an optimally-doped (OPT) Bi2212 sample, measured in total electron yield (TEY) mode for two linear polarizations: σ and π (referred to the sample surface) or, equivalently, vertical (V) and horizontal (H) referred to the horizontal scattering plane. Both spectra are dominated by a sharp excitonic 'white line' which corresponds to a $2p^5 3d^{10}$ final state, i.e. a transition from the $2p$ core level into the empty $x^2 - y^2$ orbital. In the geometry of the figure (20° grazing incidence) the transition is considerably stronger for σ polarization, when the electric field of the incoming photon beam lies in the ab plane. By contrast, in the spectrum measured with π polarization (i.e. with the electric field mainly along the c axis) the intensity of the white line is comparable to that of higher-energy transitions into extended states of s or d character, which are almost invisible for σ polarization.

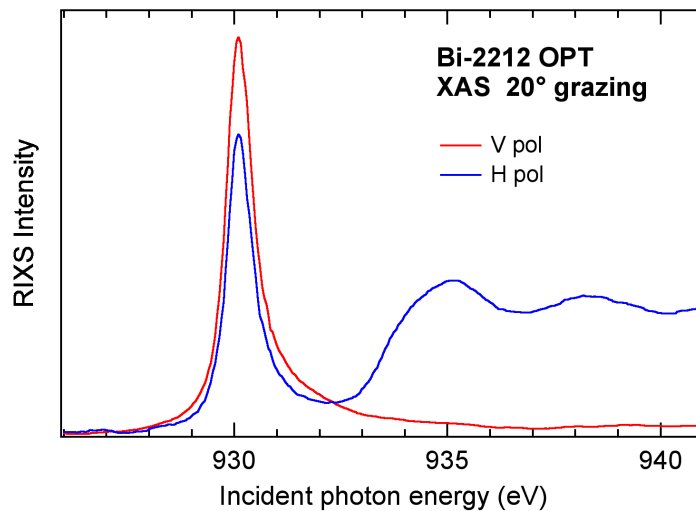


Figure 6.9: Total electron yield Cu L_3 absorption spectra of OPT Bi2212 for two linear polarizations: σ or vertical (V) and π or horizontal (H).

Figure 6.10 shows an L_3 spectrum of OPT Bi2212 and, for comparison, a spectrum of

SCOC, measured in the same conditions. The Bi2212 spectrum exhibits the same typical features, namely a prominent *dd* structure and – remarkably – a low-energy ‘magnetic’ loss. There are nevertheless some distinct differences. Firstly, the manifold of *dd* excitations is broader, extending from -1.2 to \sim -3 eV. This is clearly an indication of larger interactions between the Cu 3*d* and the ligand (oxygen 2*p*) orbitals. A larger interaction is indeed expected on two accounts: i) the shorter Cu–ligand distance in Bi2212, and ii) the larger spatial extension of the O 2*p* orbital of the apical oxygen with respect to the 3*p* orbital of the apical chlorine atoms in SCOC. Secondly, the sublevels of the same *dd* manifold are less well defined in the SC material. This could be due to the lower symmetry of the Cu ion – square pyramidal instead of tetragonal – which lifts the degeneracy of the *xz* and *yz* states. A further contribution to the line width could be the result of metallic screening, which reduces the strongly excitonic character of these electron-hole excitations, similarly to observations in optical spectra. Cluster calculations are under way to clarify these observations. Finally, the low-energy ‘magnetic’ feature is weaker and broader than in SCOC. Bi2212 is obviously not an AFM, and a naive interpretation of this loss in terms of magnons is not possible. Low-energy electron-hole excitations, which are forbidden in an insulator, are possible within the partially occupied Zhang-Rice band of metallic Bi2212, and build up the quasielastic response. These excitations are not likely to be simple as in a free-electron metal. In fact, the clear correspondence with the SCOC lineshape suggests that they involve short-range magnetic fluctuations.

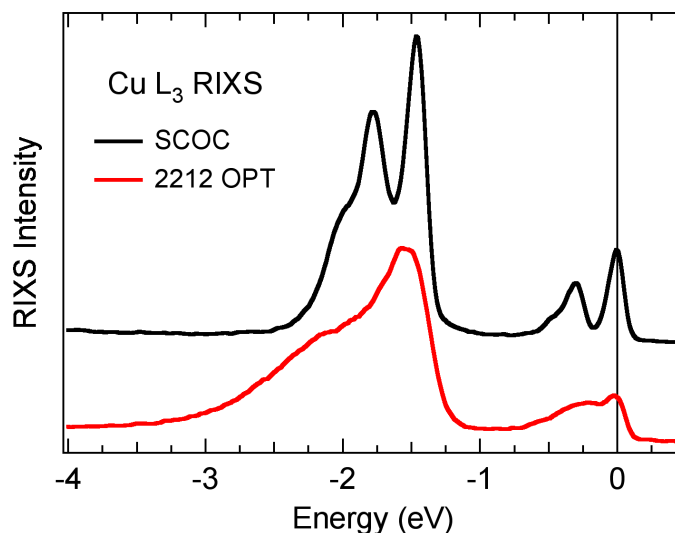


Figure 6.10: L_3 RIXS spectra of SCOC and of an optimally doped Bi-2212 sample.

Further insight can be gained by probing the local electronic structure around the O sites. Figure 6.11 shows the TEY O K edge ($1s \rightarrow 2p$) XAS spectrum. The leading lorentzian peak

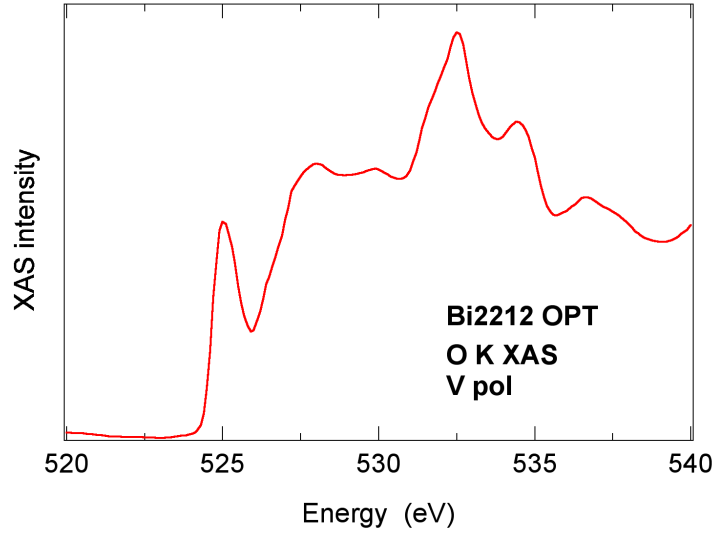


Figure 6.11: TEY O $1s$ XAS of OPT Bi2212.

corresponds a $1s^1 3d^{10}$ final state, i.e. to transitions from an O $1s$ core state to a hybrid empty state of mixed Cu $3d$ and O $2p$ character. This is the same orbital of $x^2 - y^2$ symmetry involved in the Cu L_3 XAS, but this time probed from the O site. The rich higher-energy structures correspond to extended conduction states of O p character. Figure 6.12 shows O $1s$ RIXS spectra measured at three incident energies – labelled A, B and C – over a photon energy of 1 eV around the maximum of the $1s^1 3d^{10}$ XAS peak. The spectrum measured at the lowest incident energy (A) exhibits the characteristic manifold of dd losses around ~ 2 eV, and a strong feature extending to ~ 8 eV which reflects charge-transfer excitations. At the maximum of the XAS pre-peak (B) the dd and CT features have shifted to larger excitation energies, as expected for an above-threshold fluorescence (at constant emitted energy) component. This suggests that the actual threshold for the XAS transitions is close to “A”. At the same time a ‘mid-infrared’ loss appears around ~ 0.5 eV. At higher excitation energy (C) there is a further drift of the dd and CT features, and also of the low-energy loss, which broadens and loses intensity.

The Cu L_3 and O K edge RIXS spectra are compared in Figure 6.13. The comparison further makes clear that the same final states are probed at the two edges, but with different efficiencies. Moreover, the ‘one magnon’ loss Cu at ~ 0.3 eV is visible in the L_3 spectrum, but it is forbidden in the O K one by angular momentum conservation. It would be natural to associate the rather strong feature at ~ 0.5 eV in the O K spectrum to a two-magnon loss. However, as discussed before, things are more complex in a metallic material. This is also confirmed by the observation of an associated fluorescence-like signal in the higher-energy spectrum ‘C’, which is unexpected for a pure spin excitation, but is compatible with a band

excitation. The important issue will remain open until a comprehensive theory – now lacking – is developed for RIXS in the doped cuprates.

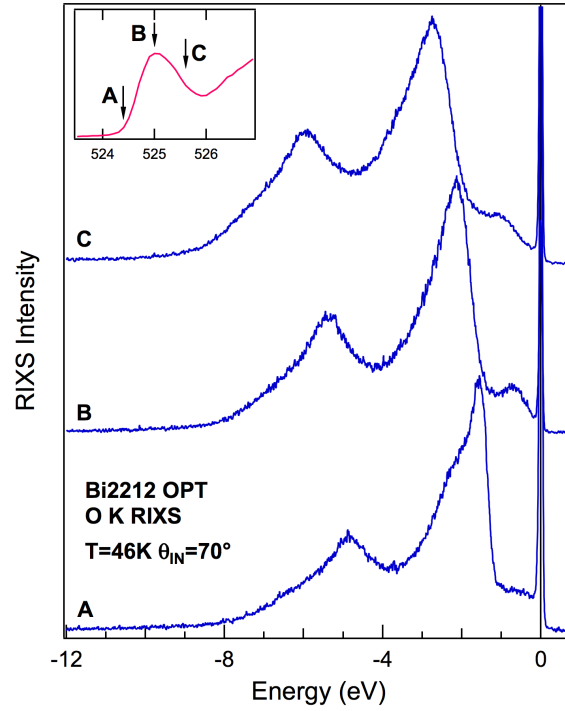


Figure 6.12: O $1s$ RIXS spectra of OPT Bi2212 measured at three incident energies – labelled A, B and C – around the $1s^{13}d^{10}$ XAS peak (inset).

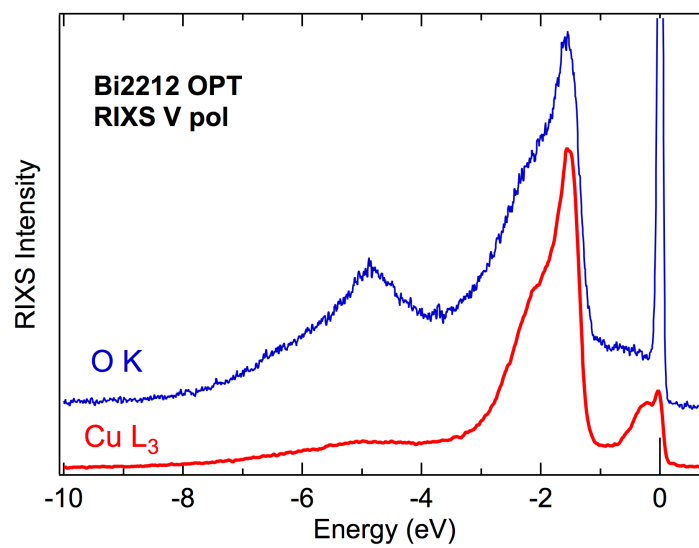


Figure 6.13: Comparison of the Cu L_3 and O K (spectrum 'A' from Figure 6.12).

In the final part of this Chapter, I will show selected RIXS data for an optimally doped Bi2223 sample. Figure 6.14 shows the L_3 TEY XAS spectra for the two polarizations. Both of them show a somewhat larger intensity at ~ 932.5 with respect to the XAS spectra of Bi2212, in a region which reflects transitions from $3d^9 \underline{L}$ initial states, i.e. from the doped Cu sites. Again we observe a transfer of spectral weight between the white line and the band features at higher energy as a function of polarization. Here the effect is weaker because the incidence angle of the photon beam was a less grazing 45° , rather than 20° as in Fig. 6.9.

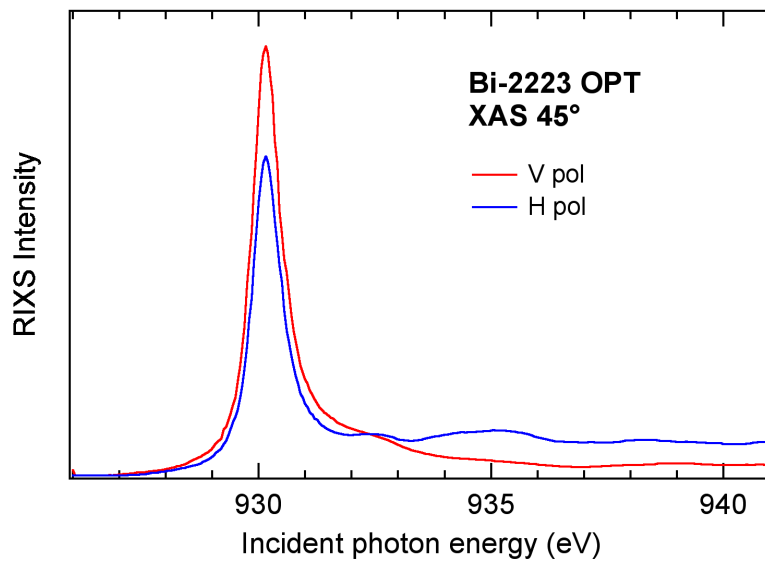


Figure 6.14: TEY L_3 XAS of an optimally doped Bi2223 sample, for two linear polarizations and a 45° incidence angle.

Figure 6.15 presents the Cu L_3 RIXS spectra of OPT Bi2223 for H (π) polarization and three different incidence angles (20° , 45° and 70°) at the fixed scattering angle of 90° . The incidence angle θ_{in} is the angle between the incoming beam and the sample normal (the c axis), which lies in the horizontal scattering plane. The 45° (specular reflection) spectrum exhibits the prominent dd feature, and little intensity up to the elastic peak, which is slightly asymmetric due to a tail of electron-hole and phonon losses. The 20° (20° grazing emission) and the 70° (20° grazing incidence) spectra are taken at symmetric angular positions ($\pm 25^\circ$, same $|Q_{||}|$) with respect to the specular reflection condition. As predicted by theory [181] their lineshape is not identical, though. The weight distribution within the dd manifold explicitly depends on θ_{in} . The lower S/N ratio at $\theta_{in}=70^\circ$ is a direct consequence of the larger projection of the electric field on the ab plane at this angle, yielding a lower absorption. On the other hand, the magnetic signal is rather similar at the two angles, and similar to that of

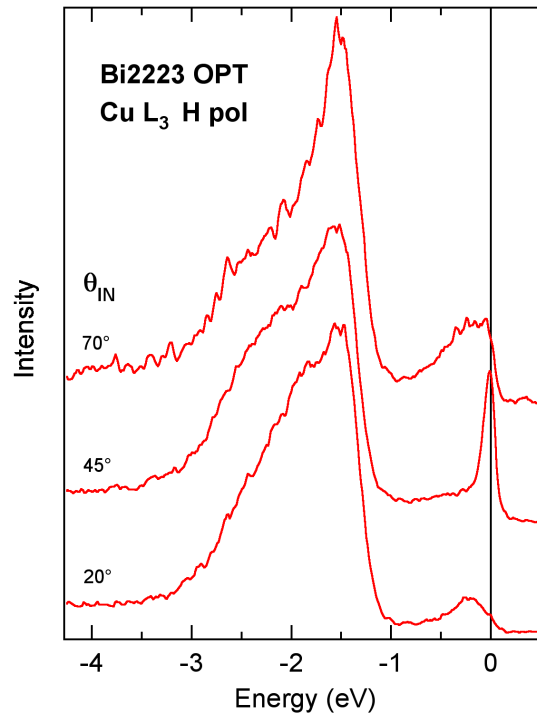


Figure 6.15: Cu L₃ RIXS spectra of OPT Bi2223 for H (π) polarization and three different incidence angles. The fixed scattering angle was 90°.

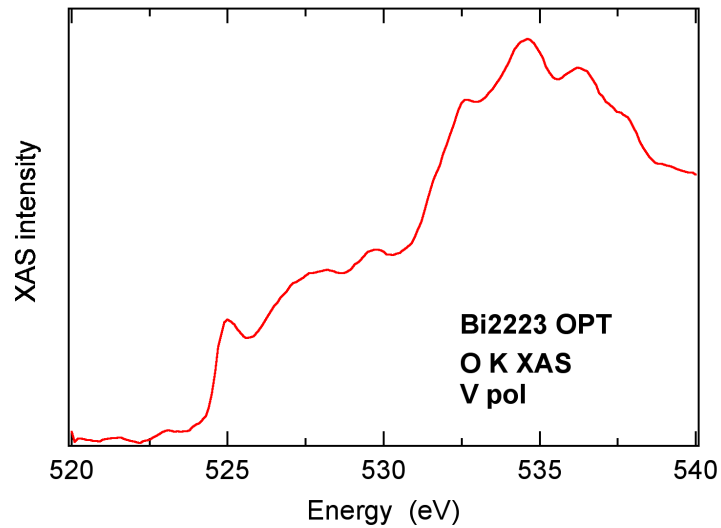


Figure 6.16: O 1s TEY XAS spectrum of OPT Bi2223.

Bi2212. The elastic peak appears larger at 70°, because of the larger relative weight of diffuse (non resonant) scattering, and also because the elastic peak is more strongly self-absorbed

(absorbed on the ‘way out’) at more grazing emission ($\theta_{in}=20^\circ$).

Figure 6.16 illustrates the O K XAS of OPT Bi2223. Once again the spectrum exhibits a $1s3d^{10}$ pre-peak, and a rather complex higher energy lineshape. O K-edge RIXS spectra measured across the maximum of the pre-peak are shown in Fig. 6.17. These data confirm the results for OPT Bi2212. There is an energy shift between spectra ‘A’ and ‘B’, with the onset of a fluorescent signal. The ‘mid infrared’ loss is largest at ‘B’, which stresses again the role played by the Cu $3d$ hole at the origin of this feature. This feature also exhibits a very strong polarization dependence, as shown by the comparison of the spectra for σ and π polarization at ‘B’. Interestingly, this loss is totally absent in the latter (shown for clarity after subtraction of a resolution-limited elastic peak). These observations are not of immediate interpretation, but set strict constraints on a future theory of RIXS in the metallic cuprates, and more generally on a theory of the magnetic excitations in these compounds.

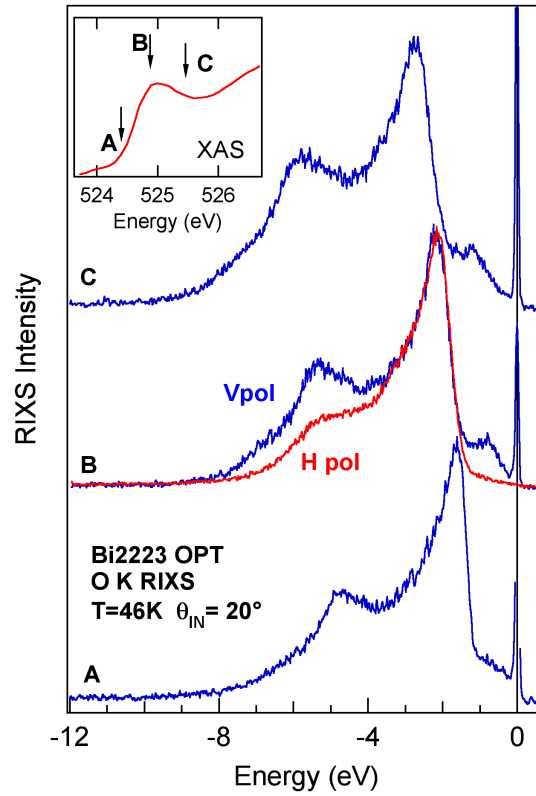


Figure 6.17: O $1s$ RIXS spectra of OPT Bi2223 measured at three incident energies – labelled A, B and C – around the $1s^13d^{10}$ XAS peak (inset) with V (σ) polarization. The red curve ‘B’ is for H (π) polarization, after subtraction of the elastic peak.

In summary, these preliminary RIXS experiments demonstrate that resonant dispersive ‘mid infrared’ losses of likely magnetic origin survive from the AFM insulator well into the SC phase

of the phase diagram. They exhibit a clear dependence on the excitation mechanism. Namely, they are quite different at the Cu L_3 and O K thresholds, in line with the predicted properties of one- and two-magnon excitations. They also exhibit a remarkable polarization dependence, consistent with a strong implication of the $x^2 - y^2$ hole state in the creation of the collective excitation. These losses cannot be simply described as ‘magnons’, but they do indicate the persistence of (antiferro)magnetic interactions in the SC state. A somewhat surprising aspect of the RIXS results is the similarity of the spectra of the OPT Bi2212 and OPT Bi2223 spectra. It is quite possible that the relevant differences between the two compounds are in subtle details which cannot be appreciated by the data presented here. Further experiments now underway will probe the doping dependence of the ‘magnon’ dispersion in both compounds, as well as possible changes across the SC transition.

Chapter 7

Conclusions and outlook

In this thesis I have investigated the electronic structure of selected important low-dimensional systems, namely charge-density-wave (CDW) transition metal dichalcogenides (TMD) and high-temperature superconducting cuprate materials. For this experimental study I have mainly exploited high-resolution angle-resolved photoemission spectroscopy (ARPES), one of the most direct and powerful probe of the electronic states in solids. I have also performed exploratory experiments by resonant x-ray scattering spectroscopy (RIXS), an emergent synchrotron radiation technique.

ARPES data reveal many new interesting features of the band structure and spectral properties of these materials. The results presented here extend, and in some instances clarify, previous observations. For the 2D CDW compound 1T-TaS₂, I have found that disorder destroys long-range phase coherence and inhibits the characteristic Mott metal-insulator (MI) transition. Rather surprisingly, at very low-temperature (~ 2.1 K) disordered TaS₂ shows superconductivity in the presence of a strong CDW. The ARPES, core-level, and LEED measurements show that the normal state is a nearly-commensurate CDW phase, and that the system remains quite close to a metal-insulator instability. The data demonstrate that CDW-pinning disorder is another mechanism to suppress the MI transition and favor SC, besides external pressure, as was recently shown in a remarkable experiment by Sipos *et.al.* [36]. Our result also establishes a connection to recently published observations of the occurrence of superconductivity in 1T-polytype CDW TMDs. Those data, namely on Cu intercalated 1T-TiSe₂, had pointed out the interplay of superconductivity and CDW, two electronic instabilities which indeed compete for the same Fermi surface. The competition clearly manifests itself in opposite trends for the SC and CDW transition temperatures.

Another 1T-polytype TMD compound I have studied is 1T-TiS₂ which, besides its interesting electronic properties, has potential interest for possible application in advanced batteries. Pristine 1T-TiS₂ is a narrow band gap degenerated (by self-doping) semiconductor. Upon Nb doping, it undergoes a metal-to-semiconductor transition. I was able to characterize this tran-

sition by ARPES, and to follow the rigid-band-like filling of the Ti $3d$ conduction band, but also the development of an energy gap at the Fermi level.

I have also investigated the connection between SC and CDW in a member of a different class of materials, the 2H-polytype TMDs. Sn-intercalation of 2H-TaS₂ shows superconductivity with suppressed T_{CDW} as revealed by the resistivity data. ARPES data shows that a CDW gap partially opens on the Fermi surface pocket around the K point, while the Γ pocket is unaffected. Besides a normal-state low-energy kink in the dispersion, I also observed a high energy kink due to the hybridization between the original band and the folded bands in the CDW periodic potential. Again, my work is linked to similar recent results by other groups on the related Na-intercalated 2H-TaS₂, which has shown a similar competition and coexistence between SC and CDW [90, 97].

In the second part of my thesis, I have investigated the low-energy spectroscopic features of the three-layer compound Bi2223, the high- T_c superconductor of the Bi-family with the highest T_c . By analogy with the bilayer splitting in the two-layer cuprates Bi2212, the high-quality ARPES data measured at the SLS give some evidence for the expected, but never experimentally confirmed, tri-layer splitting of the conduction band into bonding, antibonding and nonbonding subbands. The ARPES results well illustrate the d -wave symmetry of the SC gap, and the BCS-like temperature dependence, at various locations of the Fermi surface. From the analysis of the electron self-energy, I found several high energy features in the normal state which could represent electron coupling with several phonon modes. Further experimental work should be performed on the superconducting state to complete the work on Bi2223. Nevertheless, the present data extend the data base on the SC cuprates, and confirm some general features of these materials. In the search for the underlying mechanism of high- T_c SC, a comparison with a totally different class of materials, most prominently the newly discovered pnictides and chalcogenides, would at this point be of the highest interest. Our group is also involved in this challenging work.

The last part of this thesis illustrated the measurement by high resolution RIXS on the momentum dependence of magnetic excitations in the paradigmatic spin-1/2 2D antiferromagnetic insulator Sr₂CuO₂Cl₂ (SCOC). By measuring the full spin-wave spectrum, we found a large dispersion along the AFM Brillouin zone, which reveals magnetic interactions beyond nearest-neighbor in this parent compound, and suggests that similar interactions may play an important role in other cuprates. Preliminary results on optimally-doped Bi2212 and Bi2223 samples show that magnetic interactions survive in the SC part of the phase diagram.

In summary, in this thesis I investigated by means of high resolution ARPES selected low-dimensional systems characterized by two different competing electronic instabilities: CDW and SC. This is by no means the end of the work, and many questions remain open, which call for new measurements. Some of the specific, and of the more general questions have been

highlighted in the text. The present results give confidence that further developments in the experimental capabilities – namely, ever improved energy and momentum resolution – and the constant availability of high-quality samples, will give a real chance for these questions to be answered.

Bibliography

- [1] R.E. Peierls. *Quantum theory of solids*. Clarendon, Oxford, 1955.
- [2] H. Frohlich. On the theory of superconductivity: the one-dimensional case. *Proceedings of the Royal Society of London. Series A. Mathematical and Physical Sciences*, 223(1154):296, 1954.
- [3] G. Grüner. *Density Waves in solids*. Addison-Wesley, Reading, Massachusetts, 1994.
- [4] S. Hüfner. *Very high resolution photoelectron spectroscopy*. Springer, 2007.
- [5] W. Kohn. Image of the Fermi Surface in the Vibration Spectrum of a Metal. *Phys. Rev. Lett.*, 2(9):393–394, 1959.
- [6] F. Zwick. *Angle resolved photoelectron spectroscopy on strongly correlated electron-phonon systems*. PhD thesis, EPFL, Lausanne, 1999.
- [7] M. Grioni. Electronic properties of solids and superconductivity. *Lectures in EPFL*, 2009.
- [8] F. Gebhard. *The mott metal-insulator transition: models and methods*. Springer Verlag, 1997.
- [9] L. Perfetti, A. Georges, S. Florens, S. Biermann, S. Mitrovic, H. Berger, Y. Tomm, H. Höchst, and M. Grioni. Spectroscopic Signatures of a Bandwidth-Controlled Mott Transition at the Surface of 1T-TaSe₂. *Phys. Rev. Lett.*, 90(16):166401, 2003.
- [10] F. London and H. London. . *Proceedings of the Royal Society of London*, A149:71, 1935.
- [11] J. Bardeen, L.N. Cooper, and J.R. Schrieffer. Theory of Superconductivity. *Phys. Rev.*, 108(5):1175–1204, 1957.
- [12] J.W. Rohlfs. *Modern Physics from α to Z₀*. Wiley, 1994.
- [13] F.J. Blatt. *Modern Physics*. McGraw-Hill, 1992.
- [14] J.G. Bednorz and K.A. Müller. *Z. Physik B*, 64:189, 1986.

- [15] M.K. Wu, J.R. Ashburn, C.J. Torng, P.H. Hor, R.L. Meng, L. Gao, Z.J. Huang, Y.Q. Wang, and C.W. Chu. Superconductivity at 93 K in a new mixed-phase YBaCuO compound system at ambient pressure. *Phys. Rev. Lett.*, 58(9):908–910.
- [16] C.W. Chu, L. Gao, F. Chen, Z.J. Huang, R.L. Meng, and Y.Y. Xue. Superconductivity above 150-K in $\text{HgBa}_2\text{Ca}_2\text{Cu}_3\text{O}_{8+\delta}$ at high-pressures. *Nature*, 365(6444):323–325, 1993.
- [17] A. Damascelli, Z. Hussain, and Z.X. Shen. Angle-resolved photoemission studies of the cuprate superconductors. *Rev. Mod. Phys.*, 75(2):473–541, 2003.
- [18] N.M. Plakida. *High-temperature superconductivity*. Springer-Verlag, Berlin, 1995.
- [19] K. Tanaka. *Photoemission study of Bi-cuprate high- T_c superconductors in the lightly-doped to underdoped regions*. PhD thesis, University of Tokyo, 2004.
- [20] S. Uchida, T. Ido, H. Takagi, T. Arima, Y. Tokura, and S. Tajima. Optical spectra of $\text{La}_{2-x}\text{Sr}_x\text{CuO}_4$: Effect of carrier doping on the electronic structure of the CuO_2 plane. *Phys. Rev. B*, 43(10):7942–7954, 1991.
- [21] F.C. Zhang and T.M. Rice. Effective Hamiltonian for the superconducting Cu oxides. *Phys. Rev. B*, 37(7):3759–3761, 1988.
- [22] H. Eskes and G.A. Sawatzky. Single-, triple-, or multiple-band Hubbard models. *Phys. Rev. B*, 44(17):9656–9666, 1991.
- [23] P.W. Anderson. The resonating valence bond state in La_2CuO_4 and superconduction. *Science*, 235:1196–1198, 1987.
- [24] H. R. Hertz. *Ann. Der Physik*, 267:983, 1887.
- [25] A. Einstein. *Ann. Der Physik*, 325:199, 1906.
- [26] S. Hufner. *Photoelectron Spectroscopy*. Springer-Verlag, Berlin Heidelberg, 1995.
- [27] X.J. Zhou, T. Cuk, T. Devereaux, N. Nagaosa, and Z.X. Shen. Angle-resolved photoemission spectroscopy on electronic structure and electron-phonon coupling in cuprate superconductors. *Handbook of high-temperature superconductivity: theory and experiment*, pages 87–144, 2007.
- [28] C.N. Berglund and W.E. Spicer. Photoemission studies of copper + silver - theory. *Phys. Rev. A-General Physics*, 136(4A):1030–&, 1964.

- [29] D.S. Inosov. *Angle-resolved photoelectron spectroscopy studies of the many-body effects in the electronic structure of high- T_c cuprates*. PhD thesis, Der Technische universität, Dresden, 2008.
- [30] G.A Sawatzky. Testing Fermi-liquid models. *Nature*, 342:480–481, 1989.
- [31] G.D. Mahan. *Many-particle physics*. Plenum Pub Corp, 2000.
- [32] M. Grioni. *Neutron and x-ray spectroscopy*. Springer Verlag, 2006.
- [33] L. Perfetti. *Angle resolved photoelectron spectroscopy on strongly correlated electron-phonon systems*. PhD thesis, EPFL, Lausanne, 2002.
- [34] A.A. Kordyuk and S.V. Borisenko. Details of the photoemission spectra analysis. *Arxiv preprint cond-mat/0510421*, 2005.
- [35] J.A. Wilson, F.J. Disalvo, and S. Mahajan. Charge-Density waves and superlattices in metallic layered transition-metal dichalcogenides. *Ada. Phys.*, 24(2):117–201, 1975.
- [36] B. Sipos, A.F. Kusmartseva, A. Akrap, H. Berger, L. Forró, and E. Tutiš. From Mott state to superconductivity in 1T-TaS₂. *Nature Materials*, 7(12):960–965, 2008.
- [37] R.E. Thomson, B. Burk, A. Zettl, and J. Clarke. Scanning tunneling microscopy of the charge-density-wave structure in 1T-TaS₂. *Phys. Rev. B*, 49(24):16899–16916, Jun 1994.
- [38] X.L. Wu and C.M. Lieber. Direct observation of growth and melting of the hexagonal-domain charge-density-wave phase in 1T-TaS₂ by scanning tunneling microscopy. *Phys. Rev. Lett.*, 64(10):1150–1153, 1990.
- [39] B. Dardel, M. Grioni, D. Malterre, P. Weibel, Y. Baer, and F. Lévy. Spectroscopic signatures of phase transitions in a charge-density-wave system: 1T-TaS₂. *Phys. Rev. B*, 46(12):7407–7412, 1992.
- [40] B. Dardel, M. Grioni, D. Malterre, P. Weibel, Y. Baer, and F. Lévy. Temperature-dependent pseudogap and electron localization in 1T-TaS₂. *Phys. Rev. B*, 45(3):1462–1465, 1992.
- [41] M. Grioni, L. Perfetti, and H. Berger. Strong electron-electron and electron-phonon interactions in one- and two-dimensional solids. *Journal of electron spectroscopy and related phenomena*, 137(Sp. Iss. SI):417–423, 2004. 9th International Conference on Electronic Spectroscopy and Structure, Uppsala, Sweden, JUN 30-JUL 04, 2003.

- [42] H.P. Hughes and R.A. Pollak. Charge-density waves in layered metals observed by x-ray photoemission. *Philosophical Magazine*, 34(6):1025–1046, 1976.
- [43] H.J. Crawack and C. Pettenkofer. Calculation and XPS measurements of the Ta4f CDW splitting in Cu, Cs and Li intercalation phases of 1T-TaX₂ (X= S, Se). *Solid State Commun.*, 118(7):325–332, 2001.
- [44] E. Morosan, H.W. Zandbergen, B.S. Dennis, J.W.G. Bos, Y. Onose, T. Klimczuk, A.P. Ramirez, N.P. Ong, and R.J. Cava. Superconductivity in Cu_xTiSe₂. *Nature Physics*, 2(8):544–550, 2006.
- [45] T. Straub, T. Finteis, R. Claessen, P. Steiner, S. H fner, P. Blaha, C.S. Oglesby, and E. Bucher. Charge-Density-Wave Mechanism in 2H-NbSe₂: Photoemission Results. *Phys. Rev. Lett.*, 82(22):4504–4507, May 1999.
- [46] T. Yokoya, T. Kiss, A. Chainani, S. Shin, M. Nohara, and H. Takagi. Fermi surface sheet-dependent superconductivity in 2H-NbSe₂. *Science*, 294(5551):2518, 2001.
- [47] S. V. Borisenko, A. A. Kordyuk, A. N. Yaresko, V. B. Zabolotnyy, D. S. Inosov, R. Schuster, B. B chner, R. Weber, R. Follath, L. Patthey, and H. Berger. Pseudogap and Charge Density Waves in Two Dimensions. *Phys. Rev. Lett.*, 100(19):196402, May 2008.
- [48] D. W. Shen, Y. Zhang, L. X. Yang, J. Wei, H. W. Ou, J. K. Dong, B. P. Xie, C. He, J. F. Zhao, B. Zhou, M. Arita, K. Shimada, H. Namatame, M. Taniguchi, J. Shi, and D. L. Feng. Primary Role of the Barely Occupied States in the Charge Density Wave Formation of NbSe₂. *Phys. Rev. Lett.*, 101(22):226406, 2008.
- [49] T. M. Rice and G. K. Scott. New Mechanism for a Charge-Density-Wave Instability. *Phys. Rev. Lett.*, 35(2):120–123, Jul 1975.
- [50] A. H. Castro Neto. Charge Density Wave, Superconductivity, and Anomalous Metallic Behavior in 2D Transition Metal Dichalcogenides. *Phys. Rev. Lett.*, 86(19):4382–4385, May 2001.
- [51] P. Fazekas and E. Tosatti. *Philos. Mag. B*, 39:229, 1979.
- [52] F. J. Di Salvo, J. A. Wilson, B. G. Bagley, and J. V. Waszczak. Effects of doping on charge-density waves in layer compounds. *Phys. Rev. B*, 12(6):2220–2235, 1975.
- [53] H. Mutka, L. Zuppiroli, P. Molini , and J.C. Bourgoin. Charge-density waves and localization in electron-irradiated 1T-TaS₂. *Phys. Rev. B*, 23(10):5030–5037, 1981.

- [54] F. Zwick, H. Berger, I. Vobornik, G. Margaritondo, L. Forró, C. Beeli, M. Onellion, G. Panaccione, A. Taleb-Ibrahimi, and M. Grioni. Spectral Consequences of Broken Phase Coherence in 1T-TaS₂. *Phys. Rev. Lett.*, 81(5):1058–1061, 1998.
- [55] R.A. Pollak, D.E. Eastman, F.J. Himpsel, P. Heimann, and B. Reihl. 1T-TaS₂ charge-density-wave metal-insulator transition and Fermi-surface modification observed by photoemission. *Phys. Rev. B*, 24(12):7435–7438, 1981.
- [56] H.P. Hughes and J.A. Scarfe. Site Specific Photohole Screening in a Charge Density Wave. *Phys. Rev. Lett.*, 74(15):3069–3072, 1995.
- [57] K. Rossnagel and N.V. Smith. Spin-orbit coupling in the band structure of reconstructed 1T-TaS₂. *Phys. Rev. B*, 73(7):073106, 2006.
- [58] N.V. Smith, S.D. Kevan, and F.J. DiSalvo. Band structures of the layer compounds 1T-TaS₂ and 2H-TaSe₂ in the presence of commensurate charge-density waves. *J. Phys. C: Solid State Phys.*, 18:3175–3189, 1985.
- [59] R. Manzke, T. Buslaps, B. Pfalzgraf, M. Skibowski, and O. Anderson. On the Phase Transitions in 1T-TaS₂. *EPL (Europhysics Letters)*, 8:195–200, 1989.
- [60] R. Claessen, B. Burandt, H. Carstensen, and M. Skibowski. Conduction-band structure and charge-density waves in 1T-TaS₂. *Phys. Rev. B*, 41(12):8270–8277, 1990.
- [61] Y. Aiura, I. Hase, K. Yagi-Watanabe, H. Bando, K. Ozawa, K. Tanaka, R. Kitagawa, S. Maruyama, T. Iwase, Y. Nishihara, K. Horiba, O. Shiino, M. Oshima, M. Nakatake, M. Kubota, and K. Ono. Increase in charge-density-wave potential of 1T-TaS_xSe_{2-x}. *Phys. Rev. B*, 69(24):245123, 2004.
- [62] A. Georges, G. Kotliar, W. Krauth, and M.J. Rozenberg. Dynamical mean-field theory of strongly correlated fermion systems and the limit of infinite dimensions. *Rev. Mod. Phys.*, 68(1):13, 1996.
- [63] L. Perfetti, T. A. Gloor, F. Mila, H. Berger, and M. Grioni. Unexpected periodicity in the quasi-two-dimensional Mott insulator 1T-TaS₂ revealed by angle-resolved photoemission. *Phys. Rev. B*, 71(15):153101, 2005.
- [64] L. Perfetti, C. Rojas, A. Reginelli, L. Gavioli, H. Berger, G. Margaritondo, M. Grioni, R. Gaal, L. Forró, and F. Rullier-Albenque. High-resolution angle-resolved photoemission investigation of the quasiparticle scattering processes in a model Fermi liquid: 1T – TiTe₂. *Phys. Rev. B*, 64:115102, 2001.

- [65] J.A. Wilson and A.D. Yoffe. Transition metal dichalcogenides discussion and interpretation of observed optical, electrical and structural properties. *Adv. Phys.*, 18(73):193, 1969.
- [66] C.H. Chen, W. Fabian, F.C. Brown, K.C. Woo, B. Davies, B. DeLong, and A.H. Thompson. Angle-resolved photoemission studies of the band structure of TiSe_2 and TiS_2 . *Phys. Rev. B*, 21(2):615–624, Jan 1980.
- [67] J.J. Barry and H.P. Hughes. Angle-resolved photoemission-study of some of the 1st-row transition-metal dichalcogenides of NbS_2 and TaS_2 . *J. Phys. C Solid State Phys.*, 16(27):5393–5407, 1983.
- [68] H.I. Starnberg, H.E. Brauer, and H.P. Hughes. Photoemission studies of the conduction band filling in $\text{Ti}_{1.05}\text{S}_2$ and Cs-intercalated TiS_2 and ZrSe_2 . *J. Phys.-Condens. Mat.*, 8(9):1229–1234, 1996.
- [69] T. Matsushita, S. Suga, A. Kimura, H. Negishi, and M. Inoue. Angle-resolved photoemission study of Ni-intercalated 1T- TiS_2 . *Phys. Rev. B*, 60(3):1678–1686, 1999.
- [70] S. Nohara, H. Namatame, H. Matsubara, M. Fujisawa, M. Naitou, S. Tanaka, H. Negishi, M. Inoue, H. Sakamoto, A. Misu, and S. Suga. Angle-resolved inverse photoemission spectra of layered 1T-VSe₂, 1T-TiS₂, 1T-TaS₂, 2H-NbSe₂ AND 2H-TaSe₂. *J. Phys. Soc. Japan*, 60(11):3882–3892, 1991.
- [71] D.L. Greenaway and R. Nitsche. Preparation and optical properties of group 4-62 chalcogenides having CDI_2 structure. *J. Phys. Chem. Solids*, 26(9):1445–&, 1965.
- [72] D.R. Allan, A.A. Kelsey, S.J. Clark, R.J. Angel, and G.J. Ackland. High-pressure semiconductor-semimetal transition in TiS_2 . *Phys. Rev. B*, 57(9):5106–5110, 1998.
- [73] T. Teshima, N. Suzuki, and K. Motizuki. Electronic band structures of 1T-type TiS_2 intercalated with light-3D transition-metals. *J. Phys. Soc. Japan*, 60(3):1005–1010, 1991.
- [74] P.C. Klipstein and R.H. Friend. Semiconductor to semimetal transition in TiS_2 at 40 Kbar. *J. Phys. C Solid State Phys.*, 17(15):2713–2734, 1984.
- [75] G.A. Benesh, A.M. Woolley, and C. Umrigar. The pressure dependences of TiS_2 and TiSe_2 band structures. *J. Phys. C Solid State Phys.*, 18(8):1595–1603, 1985.
- [76] A. Zunger and A.J. Freeman. Self-consistent numerical-basis-set linear-combination-of-atomic-orbitals investigation of the electronic structure and properties of TiS_2 . *Phys. Rev. B*, 16(2):906–924, 1977.

- [77] H. Starnberg, H. Brauer, and H. Hughes. *Electron Spectroscopies Applied to Low-Dimensional materials*, publisher = Kluwer Academic Publisher. 2000.
- [78] P. Xu, J.O. Piatek, P.H. Lin, B. Sipos, H. Berger, L. Forró, H.M. Rønnow, and M. Grioni. Superconducting phase in the layered dichalcogenide $1T - TaS_2$ upon inhibition of the metal-insulator transition. *Phys. Rev. B*, 81(17):172503, 2010.
- [79] D. Qian, D. Hsieh, L. Wray, E. Morosan, N.L. Wang, Y. Xia, R.J. Cava, and M.Z. Hasan. Emergence of Fermi Pockets in a New Excitonic Charge-Density-Wave Melted Superconductor. *Phys. Rev. Lett.*, 98(11):117007, 2007.
- [80] K. Suzuki, O. Nakamura, T. Kondo, and T. Enoki. Physical properties of the 3d transition metal intercalates of incommensurate misfit layer compound S. *J. Phys. Chem. Solids*, 57(6-8):1133–1136, 1996.
- [81] A. Kimura, H. Negishi, M. Inoue, T. Matsushita, Y. Saitoh, S. Imada, and S. Suga. Electronic structures of $1T-TiS_2$ and the intercalation compound $Ni_{1/3}TiS_2$ from x-ray spectroscopies: Electron correlation and hybridization effects. *Phys. Rev. B*, 76(23):235102, 2007.
- [82] X.Y. Qin, J. Zhang, D. Li, H. Z. Dong, and L. Wang. The effect of Mg substitution for Ti on transport and thermoelectric properties of TiS_2 . *J. Appl. Phys.*, 102(7):073703, 2007.
- [83] H.E. Brauer, H.I. Starnberg, L.J. Holleboom, H.P. Hughes, and V.N. Strocov. Modifying the electronic structure of TiS_2 by alkali metal intercalation. *J. Phys.-Condens. Mat.*, 11(45):8957–8973, 1999.
- [84] J.F. Zhao, H.W. Ou, G. Wu, B.P. Xie, Y. Zhang, D.W. Shen, J. Wei, L.X. Yang, J.K. Dong, M. Arita, H. Namatame, M. Taniguchi, X.H. Chen, and D.L. Feng. Evolution of the Electronic Structure of $1T-Cu_xTiSe_2$. *Phys. Rev. Lett.*, 99(14):146401, 2007.
- [85] T. Sato, H. Komatsu, T. Takahashi, M. Shimakawa, and K. Hayashi. Electronic structure of layered transition-metal dichalcogenides $Nb_{1-x}Ti_xXc_2$ ($Xc = S, Se, Te$) studied by angle-resolved photoemission spectroscopy. *J Phys.-Condens. Mat.*, 16:8599, 2004.
- [86] N.F. Mott. *Metal-Insulator Transition*. Taylor and Francis, 1990.
- [87] M. Scharli, J. Brunner, H.P. Vaterlaus, and F. Levy. The influence of V-impurities on the electronic and vibrational properties of TiS_2 single-crystals .2. angular-resolved photoemission-studies. *J. Phys. C: Solid State Phys.*, 16(8):1527–1536, 1983.

- [88] L. Perfetti, A. Georges, S. Florens, S. Biermann, S. Mitrovic, H. Berger, Y. Tamm, H. Höchst, and M. Grioni. Spectroscopic Signatures of a Bandwidth-Controlled Mott Transition at the Surface of 1T-TaSe₂. *Phys. Rev. Lett.*, 90(16):166401, 2003.
- [89] A. H. Castro Neto. Charge density wave, superconductivity, and anomalous metallic behavior in 2d transition metal dichalcogenides. *Phys. Rev. Lett.*, 86(19):4382–4385, May 2001.
- [90] L. Fang, Y. Wang, P.Y. Zou, L. Tang, Z. Xu, H. Chen, C. Dong, L. Shan, and H.H. Wen. Fabrication and superconductivity of Na_xTaS₂ crystals. *Phys. Rev. B*, 72(1):014534, Jul 2005.
- [91] K.E. Wagner, E. Morosan, Y.S. Hor, J. Tao, Y. Zhu, T. Sanders, T.M. McQueen, H.W. Zandbergen, A.J. Williams, D.V. West, and R.J. Cava. Tuning the charge density wave and superconductivity in Cu_xTaS₂. *Phys. Rev. B*, 78(10):104520, 2008.
- [92] R. Corcoran, P.Y. Onuki, P.A. Probst, M. Springford, K. Takita, H. Harima, G.Y. Guo, and B. L. Györfy. *J. Phys. Condens. Matter*, 6:4479, 1994.
- [93] R.R. Liu, C.G. Olson, W.C. Tonjes, and R.F. Frindt. Momentum Dependent Spectral Changes Induced by the Charge Density Wave in 2H-TaSe₂ and the Implication on the CDW Mechanism. *Phys. Rev. Lett.*, 80(26):5762–5765, 1998.
- [94] T. Valla, A.V. Fedorov, P.D. Johnson, P.A. Glans, C. McGuinness, K.E. Smith, E.Y. Andrei, and H. Berger. Quasiparticle Spectra, Charge-Density Waves, Superconductivity, and Electron-Phonon Coupling in 2H-NbSe₂. *Phys. Rev. Lett.*, 92(8):086401, 2004.
- [95] W.C. Tonjes, V.A. Greanya, R. Liu, C.G. Olson, and P. Molinié. Charge-density-wave mechanism in the 2H-NbSe₂ family: Angle-resolved photoemission studies. *Phys. Rev. B*, 63(23):235101, 2001.
- [96] K. Rossnagel, E. Rotenberg, H. Koh, N.V. Smith, and L. Kipp. Fermi surface, charge-density-wave gap, and kinks in 2H-TaSe₂. *Phys. Rev. B*, 72(12):121103, Sep 2005.
- [97] D.W. Shen, B.P. Xie, J.F. Zhao, L.X. Yang, L. Fang, J. Shi, R.H. He, D.H. Lu, H.H. Wen, and D.L. Feng. Novel Mechanism of a Charge Density Wave in a Transition Metal Dichalcogenide. *Phys. Rev. Lett.*, 99(21):216404, 2007.
- [98] V. Vescoli, L. Degiorgi, H. Berger, and L. Forró. Dynamics of Correlated Two-Dimensional Materials: The 2H-TaSe₂ Case. *Phys. Rev. Lett.*, 81(2):453–456, Jul 1998.
- [99] T. Valla, A.V. Fedorov, P.D. Johnson, J. Xue, K.E. Smith, and F.J. DiSalvo. Charge-Density-Wave-Induced Modifications to the Quasiparticle Self-Energy in 2H-TaSe₂. *Phys. Rev. Lett.*, 85(22):4759–4762, 2000.

- [100] S.V. Borisenko, A.A. Kordyuk, V.B. Zabolotnyy, D.S. Inosov, D. Evtushinsky, B. Büchner, A.N. Yaresko, A. Varykhalov, R. Follath, W. Eberhardt, L. Patthey, and H. Berger. Two Energy Gaps and Fermi-Surface “Arcs” in NbSe₂. *Phys. Rev. Lett.*, 102(16):166402, 2009.
- [101] A.H. Thompson, F.R. Gamble, and R.F. Koehler. Effects of Intercalation on Electron Transport in Tantalum Disulfide. *Phys. Rev. B*, 5(8):2811–2816, 1972.
- [102] G. Wexler and A.M. Woolley. Fermi surfaces and band structures of the 2H metallic transition-metal dichalcogenides. *J. Phys. C*, 9:1185–1200, 1976.
- [103] J.A. Wilson. Charge-density waves in the 2H-TaSe₂ family: Action on the Fermi surface. *Phys. Rev. B*, 15(12):5748–5757, 1977.
- [104] T. Kiss, T. Yokoya, A. Chainani, S. Shin, T. Hanaguri, M. Nohara, and H. Takagi. Charge-order-maximized momentum-dependent superconductivity. *Nature Physics*, 3(10):720–725, 2007.
- [105] G. Brusdeylins, C. Heimlich, J.G. Skofronick, J.P. Toennies, R. Vollmer, G. Benedek, and L. Miglio. He-atom scattering study of the temperature-dependent charge-density-wave surface structure and lattice dynamics of 2H-TaSe₂(001). *Phys. Rev. B*, 41(9):5707–5716, 1990.
- [106] S. Sugai. Lattice-vibrations in the charge-density-wave states of layered transition-metal dichalcogenides. *Phys. Status Solidi B*, 129(1):13–39, 1985.
- [107] M. Hengsberger. *Unusual aspects of surface electronic structure studied with photoelectron spectroscopy*. PhD thesis, Université de Neuchâtel, 2000.
- [108] S. Engelsberg and J.R. Schrieffer. Coupled Electron-Phonon System. *Phys. Rev.*, 131(3):993, 1963.
- [109] R. Liu, W.C. Tonjes, V.A. Greanya, C.G. Olson, and R.F. Frindt. Fermi surface of 2H-TaSe₂ and its relation to the charge-density wave. *Phys. Rev. B*, 61(8):5212, 2000.
- [110] W.Z. Hu, G. Li, J. Yan, H.H. Wen, G. Wu, X.H. Chen, and N.L. Wang. Optical study of the charge-density-wave mechanism in 2H-TaS₂ and Na_xTaS₂. *Phys. Rev. B*, 76(4):045103, Jul 2007.
- [111] T. Yokoya, T. Kiss, A. Chainani, S. Shin, M. Nohara, and H. Takagi. Fermi surface sheet-dependent superconductivity in 2H-NbSe₂. *Science*, 294(5551):2518, 2001.
- [112] M. Di Stasio, K.A. Müller, and L. Pietronero. Nonhomogeneous charge distribution in layered high-T_c superconductors. *Phys. Rev. Lett.*, 64(23):2827–2830, 1990.

- [113] J.M. Tarascon, W.R. McKinnon, P. Barboux, D.M. Hwang, B.G. Bagley, L.H. Greene, G.W. Hull, Y. LePage, N. Stoffel, and M. Giroud. Preparation, structure, and properties of the superconducting compound series $\text{Bi}_2\text{Sr}_2\text{Ca}_{n-1}\text{Cu}_n\text{O}_y$ with $n=1,2$, and 3. *Phys. Rev. B*, 38(13):8885–8892, 1988.
- [114] E. Giannini, R. Gladyshevskii, N. Clayton, N. Musolino, V. Garnier, A. Piriou, and R. Flükiger. Growth, structure and physical properties of single crystals of pure and Pb-doped Bi-based high T_c superconductors. *Curr. Appl. Phys.*, 8:15 – 119, 2008.
- [115] R.M. Hazen, C.T. Prewitt, R.J. Angel, N.L. Ross, L.W. Finger, C.G. Hadidiacos, D.R. Veblen, P.J. Heaney, P.H. Hor, R.L. Meng, Y.Y. Sun, Y.Q. Wang, Y.Y. Xue, Z.J. Huang, L. Gao, J. Bechtold, and C.W. Chu. Superconductivity in the high- T_c Bi-Ca-Sr-Cu-O system: Phase identification. *Phys. Rev. Lett.*, 60(12):1174–1177, 1988.
- [116] T.M. Shaw, S.A. Shivashankar, S.J. La Placa, J.J. Cuomo, T.R. McGuire, R.A. Roy, K.H. Kelleher, and D.S. Yee. Incommensurate structure in the Bi-Sr-Ca-Cu-O 80-K superconductor. *Phys. Rev. B*, 37(16):9856–9859, 1988.
- [117] S.A. Sunshine, T. Siegrist, L.F. Schneemeyer, D.W. Murphy, R.J. Cava, B. Batlogg, R.B. van Dover, R.M. Fleming, S.H. Glarum, S. Nakahara, R. Farrow, J.J. Krajewski, S.M. Zahurak, J.V. Waszczak, J.H. Marshall, P. Marsh, L.W. Rupp, and W.F. Peck. Structure and physical properties of single crystals of the 84-K superconductor $\text{Bi}_{2.2}\text{Sr}_2\text{Ca}_{0.8}\text{Cu}_2\text{O}_{8+\delta}$. *Phys. Rev. B*, 38(1):893–896, 1988.
- [118] Ø. Fischer, M. Kugler, I. Maggio-Aprile, C. Berthod, and C. Renner. Scanning tunneling spectroscopy of high-temperature superconductors. *Rev. Mod. Phys.*, 79(1):353–419, 2007.
- [119] M. Kugler, G.L. de Castro, E. Giannini, A. Piriou, A.A. Manuel, C. Hess, and O. Fischer. Scanning tunneling spectroscopy on $\text{Bi}_2\text{Sr}_2\text{Ca}_2\text{Cu}_3\text{O}_{10+\delta}$ single crystals. *J. Phys. Chem. Solids.*, 67(1-3):353–356, 2006.
- [120] S.V. Borisenko, A.A. Kordyuk, A. Koitzsch, M. Knupfer, J. Fink, H. Berger, and C.T. Lin. Time-reversal symmetry breaking? *Nature*, 431(7004), 2004.
- [121] H. Ding, A.F. Bellman, J.C. Campuzano, M. Randeria, M.R. Norman, T. Yokoya, T. Takahashi, H. Katayama-Yoshida, T. Mochiku, K. Kadowaki, G. Jennings, and G.P. Brivio. Electronic Excitations in $\text{Bi}_2\text{Sr}_2\text{CaCu}_2\text{O}_8$: Fermi Surface, Dispersion, and Absence of Bilayer Splitting. *Phys. Rev. Lett.*, 76(9):1533–1536, 1996.
- [122] D.L. Feng, H. Eisaki, K.M. Shen, A. Damascelli, C. Kim, D.H. Lu, Z.X. Shen, K. Shimizu, J.I. Shimoyama, K. Kishio, N. Motoyama, N. Kaneko, M. Greven, and G.D. Gu. Photoe-

- mission study of the intra-unit-cell coupling in a trilayer cuprate. *International Journal of Modern Physics B*, 16(11-12):1691–1696, 2002.
- [123] D.L. Feng, N.P. Armitage, D.H. Lu, A. Damascelli, J.P. Hu, P. Bogdanov, A. Lanzara, F. Ronning, K.M. Shen, H. Eisaki, C. Kim, Z.X. Shen, J.I. Shimoyama, and K. Kishio. Bilayer Splitting in the Electronic Structure of Heavily Overdoped $\text{Bi}_2\text{Sr}_2\text{CaCu}_2\text{O}_{8+\delta}$. *Phys. Rev. Lett.*, 86(24):5550–5553, 2001.
- [124] Y.D. Chuang, A.D. Gromko, A. Fedorov, Y. Aiura, K. Oka, Y. Ando, H. Eisaki, S.I. Uchida, and D.S. Dessau. Doubling of the Bands in Overdoped $\text{Bi}_2\text{Sr}_2\text{CaCu}_2\text{O}_{8+\delta}$: Evidence for *c*-Axis Bilayer Coupling. *Phys. Rev. Lett.*, 87(11):117002, 2001.
- [125] T. Yamasaki, K. Yamazaki, A. Ino, M. Arita, H. Namatame, M. Taniguchi, A. Fujimori, Z.X. Shen, M. Ishikado, and S. Uchida. Unmasking the nodal quasiparticle dynamics in cuprate superconductors using low-energy photoemission. *Phys. Rev. B*, 75(14):140513, 2007.
- [126] S. Ideta, K. Takashima, M. Hashimoto, T. Yoshida, A. Fujimori, H. Anzai, T. Fujita, Y. Nakashima, A. Ino, M. Arita, K. Ono, M. Kubota, D. H. Lu, Z.-X. Shen, K. M. Kojima, H. Namatame, M. Taniguchi, and S. Uchida. Enhanced superconducting gaps in the tri-layer high- T_c cuprate $\text{Bi}_2\text{Sr}_2\text{Ca}_2\text{Cu}_3\text{O}_{10+\delta}$. *Phys. Rev. Lett.*, 104(22):227001, 2010.
- [127] Y. Chen, A. Iyo, W. Yang, X. Zhou, D. Lu, H. Eisaki, T.P. Devereaux, Z. Hussain, and Z.X. Shen. Anomalous Fermi-Surface Dependent Pairing in a Self-Doped High- T_c Superconductor. *Phys. Rev. Lett.*, 97(23):236401, 2006.
- [128] Z.X. Shen and D.S. Dessau. Electronic-structure and photoemission-studies of late transition-metal oxides - Mott insulators and high-temperature superconductors. *Physics Reports-Review Section of Physics Letters*, 253(1-3):2–162, 1995.
- [129] S.V. Borisenko, A.A. Kordyuk, V. Zabolotnyy, J. Geck, D. Inosov, A. Koitzsch, J. Fink, M. Knupfer, B. Büchner, V. Hinkov, C.T. Lin, B. Keimer, T. Wolf, S.G. Chiuzbăian, L. Patthey, and R. Follath. Kinks, Nodal Bilayer Splitting, and Interband Scattering in $\text{YBa}_2\text{Cu}_3\text{O}_{6+x}$. *Phys. Rev. Lett.*, 96(11):117004, 2006.
- [130] M. Mori, T. Tohyama, and S. Maekawa. Electronic states and superconductivity in multilayer high- T_c cuprates. *Phys. Rev. B*, 66(6):064502, 2002.
- [131] T. Valla, A.V. Fedorov, P.D. Johnson, Q. Li, G.D. Gu, and N. Koshizuka. Temperature Dependent Scattering Rates at the Fermi Surface of Optimally Doped $\text{Bi}_2\text{Sr}_2\text{CaCu}_2\text{O}_{8+\delta}$. *Phys. Rev. Lett.*, 85(4):828–831, 2000.

- [132] J.F. Annett. Symmetry of the order parameter for high-temperature superconductivity. *Adv. Phys.*, 39:83–126, 1990.
- [133] D.J. Van Harlingen. Phase-sensitive tests of the symmetry of the pairing state in the high-temperature superconductors—Evidence for $d_{x^2-y^2}$ symmetry. *Rev. Mod. Phys.*, 67(2):515–535, 1995.
- [134] C.C. Tsuei and J.R. Kirtley. Pairing symmetry in cuprate superconductors. *Rev. Mod. Phys.*, 72(4):969, 2000.
- [135] H. Ding, M.R. Norman, J.C. Campuzano, M. Randeria, A.F. Bellman, T. Yokoya, T. Takahashi, T. Mochiku, and K. Kadowaki. Angle-resolved photoemission spectroscopy study of the superconducting gap anisotropy in $\text{Bi}_2\text{Sr}_2\text{CaCu}_2\text{O}_{8+x}$. *Phys. Rev. B*, 54(14):R9678–R9681, 1996.
- [136] Z.X. Shen, D.S. Dessau, B.O. Wells, D.M. King, W.E. Spicer, A.J. Arko, D. Marshall, L.W. Lombardo, A. Kapitulnik, P. Dickinson, S. Doniach, J. DiCarlo, T. Loeser, and C.H. Park. Anomalous large gap anisotropy in the a-b plane of $\text{Bi}_2\text{Sr}_2\text{CaCu}_2\text{O}_{8+\delta}$. *Phys. Rev. Lett.*, 70(10):1553–1556, 1993.
- [137] J.M. Harris, Z.X. Shen, P.J. White, D.S. Marshall, M.C. Schabel, J.N. Eckstein, and I. Bozovic. Anomalous superconducting state gap size versus T_c behavior in underdoped $\text{Bi}_2\text{Sr}_2\text{Ca}_{1-x}\text{Dy}_x\text{Cu}_2\text{O}_{8+\delta}$. *Phys. Rev. B*, 54(22):R15665–R15668, 1996.
- [138] J.M. Harris, P.J. White, Z.X. Shen, H. Ikeda, R. Yoshizaki, H. Eisaki, S. Uchida, W.D. Si, J.W. Xiong, Z.X. Zhao, and D.S. Dessau. Measurement of an Anisotropic Energy Gap in Single Plane $\text{Bi}_2\text{Sr}_{2-x}\text{La}_x\text{CuO}_{6+\delta}$. *Phys. Rev. Lett.*, 79(1):143–146, 1997.
- [139] A.A. Kordyuk, S.V. Borisenko, M. Knupfer, and J. Fink. Measuring the gap in angle-resolved photoemission experiments on cuprates. *Phys. Rev. B*, 67(6):064504, 2003.
- [140] M.R. Norman, H. Ding, M. Randeria, J.C. Campuzano, T. Yokoya, T. Takeuchi, T. Takahashi, T. Mochiku, K. Kadowaki, P. Guptasarma, and D.G. Hinks. Destruction of the Fermi surface underdoped high- T_c superconductors. *Nature*, 392(6672):157–160, 1998.
- [141] D. L. Feng, A. Damascelli, K. M. Shen, N. Motoyama, D. H. Lu, H. Eisaki, K. Shimizu, J.-i. Shimoyama, K. Kishio, N. Kaneko, M. Greven, G. D. Gu, X. J. Zhou, C. Kim, F. Ronning, N. P. Armitage, and Z.-X. Shen. Electronic Structure of the Trilayer Cuprate Superconductor $\text{Bi}_2\text{Sr}_2\text{Ca}_2\text{Cu}_3\text{O}_{1+\delta}$. *Phys. Rev. Lett.*, 88(10):107001, 2002.

- [142] R. Müller, C. Janowitz, M. Schneider, R. St Unger, A. Krapf, H. Dwelk, A. Muller, L. Dudy, R. Manzke, C.R. Ast, and H. Hochst. Fermi surface and superconducting gap of triple-layered $\text{Bi}_2\text{Sr}_2\text{Ca}_2\text{Cu}_3\text{O}_{10+\delta}$. *Journal of Superconductivity*, 15(2):147–152, 2002.
- [143] S. Ideta, K. Takashima, M. Hashimoto, T. Yoshida, A. Fujimori, M. Kubota, K. Ono, K. Kojima, and S. Uchida. Anisotropy of gap and kink energies in the trilayer high- T_c cuprate superconductor $\text{Bi}_2\text{Sr}_2\text{Ca}_2\text{Cu}_3\text{O}_{10+\delta}$ - art. no. 012015. In H Oyanagi and H Eisaki, editors, *International Symposium of Lattice Effects in Cuprates High Temperature Superconductors (LEHTSC2007)*, volume 108 of *Journal of Physics Conference Series*, page 12015, 2008. International Symposium on Lattice Effects in Cuprate High Temperature Superconductors, Tsukuba, JAPAN, OCT 31-NOV 03, 2007.
- [144] T. Sato, H. Matsui, S. Nishina, T. Takahashi, T. Fujii, T. Watanabe, and A. Matsuda. Low Energy Excitation and Scaling in $\text{Bi}_2\text{Sr}_2\text{Ca}_{n-1}\text{Cu}_n\text{O}_{2n+4}$ ($n = 1 - 3$): Angle-Resolved Photoemission Spectroscopy. *Phys. Rev. Lett.*, 89(6):067005, 2002.
- [145] Y.J. Uemura, A. Keren, L.P. Le, G.M. Luke, W.D. Wu, Y. Kubo, T. Manako, Y. Shimakawa, M. Subramanian, J.L. Cobb, et al. Magnetic-field penetration depth in $\text{Ti}_2\text{Ba}_2\text{CuO}_{6+\delta}$ in the overdoped regime. *Nature*, 364(6438):605–607, 1993.
- [146] M.R. Norman, M. Randeria, H. Ding, and J.C. Campuzano. Phenomenology of the low-energy spectral function in high- T_c superconductors. *Phys. Rev. B*, 57(18):R11093–R11096, 1998.
- [147] W.S. Lee, I.M. Vishik, K. Tanaka, D.H. Lu, T. Sasagawa, N. Nagaosa, T.P. Devereaux, Z. Hussain, and Z.X. Shen. Abrupt onset of a second energy gap at the superconducting transition of underdoped $\text{Bi}_2\text{212}$. *Nature*, 450(7166):81–84, 2007.
- [148] M. Shi, J. Chang, S. Pailh  s, M.R. Norman, J.C. Campuzano, M. M  nsson, T. Claesson, O. Tjernberg, A. Bendounan, L. Patthey, N. Momono, M. Oda, M. Ido, C. Mudry, and J. Mesot. Coherent d -Wave Superconducting Gap in Underdoped $\text{La}_{2-x}\text{Sr}_x\text{CuO}_4$ by Angle-Resolved Photoemission Spectroscopy. *Phys. Rev. Lett.*, 101(4):047002, 2008.
- [149] J.C. Campuzano. The High T_c Superconductors: BCS or Not BCS? <http://www.conferences.uiuc.edu/bcs50/PDF/Campuzano.pdf>.
- [150] M. Hengsberger, R. Fr  sard, D. Purdie, P. Segovia, and Y. Baer. Electron-phonon coupling in photoemission spectra. *Phys. Rev. B*, 60(15):10796–10802, 1999.
- [151] N.W. Ashcroft and N.D. Mermin. Solid State Physics (Saunders College, Philadelphia). *International edn*, 1976.

- [152] A. Lanzara, P.V. Bogdanov, X.J. Zhou, S.A. Kellar, D.L. Feng, E.D. Lu, T. Yoshida, H. Eisaki, A. Fujimori, K. Kishio, J.I. Shimoyama, T. Noda, S. Uchida, Z. Hussain, and Z.X. Shen. Evidence for ubiquitous strong electron-phonon coupling in high-temperature superconductors. *Nature*, 412(6846):510–514, 2001.
- [153] A. Kaminski, M. Randeria, J.C. Campuzano, M.R. Norman, H. Fretwell, J. Mesot, T. Sato, T. Takahashi, and K. Kadowaki. Renormalization of Spectral Line Shape and Dispersion below T_c in $\text{Bi}_2\text{Sr}_2\text{CaCu}_2\text{O}_{8+\delta}$. *Phys. Rev. Lett.*, 86(6):1070–1073, 2001.
- [154] P.D. Johnson, T. Valla, A.V. Fedorov, Z. Yusof, B.O. Wells, Q. Li, A.R. Moodenbaugh, G.D. Gu, N. Koshizuka, C. Kendziora, S. Jian, and D.G. Hinks. Doping and Temperature Dependence of the Mass Enhancement Observed in the Cuprate $\text{Bi}_2\text{Sr}_2\text{CaCu}_2\text{O}_{8+\delta}$. *Phys. Rev. Lett.*, 87(17):177007, 2001.
- [155] X.J. Zhou, T. Yoshida, A. Lanzara, P.V. Bogdanov, S.A. Kellar, K.M. Shen, W.L. Yang, F. Ronning, T. Sasagawa, T. Kakeshita, T. Noda, H. Eisaki, S. Uchida, C.T. Lin, F. Zhou, J.W. Xiong, W.X. Ti, Z.X. Zhao, A. Fujimori, Hussain Z., and Z.X. Shen. High-temperature superconductors: Universal nodal Fermi velocity. *Nature*, 423(6938):398, 2003.
- [156] A.D. Gromko, A.V. Fedorov, Y.D. Chuang, J.D. Koralek, Y. Aiura, Y. Yamaguchi, K. Oka, Y. Ando, and D.S. Dessau. Mass-renormalized electronic excitations at (π, π) in the superconducting state of $\text{Bi}_2\text{Sr}_2\text{CaCu}_2\text{O}_{8+\delta}$. *Phys. Rev. B*, 68(17):174520, 2003.
- [157] A. Kaminski, M. Randeria, J.C. Campuzano, M.R. Norman, H. Fretwell, J. Mesot, T. Sato, T. Takahashi, and K. Kadowaki. Renormalization of Spectral Line Shape and Dispersion below T_c in $\text{Bi}_2\text{Sr}_2\text{CaCu}_2\text{O}_{8+\delta}$. *Phys. Rev. Lett.*, 86(6):1070–1073, 2001.
- [158] T.K. Kim, A.A. Kordyuk, S.V. Borisenko, A. Koitzsch, M. Knupfer, H. Berger, and J. Fink. Doping Dependence of the Mass Enhancement in $(\text{Pb,Bi})_2\text{Sr}_2\text{CaCu}_2\text{O}_8$ at the Antinodal Point in the Superconducting and Normal States. *Phys. Rev. Lett.*, 91(16):167002, 2003.
- [159] W.S. Lee, T. Cuk, W. Meevasane, D.H. Lu, K.M. Shen, Z.X. Shen, W.L. Yang, X.J. Zhou, Z. Hussain, C.T. Lin, J.-I. Shimoyama, and T.P. Devereaux. *Band Renormalization Effect in $\text{Bi}_2\text{Sr}_2\text{Ca}_2\text{Cu}_3\text{O}_{10+\delta}$* . Springer, 2007.
- [160] H. Matsui, T. Sato, T. Takahashi, H. Ding, H.B. Yang, S.C. Wang, T. Fujii, T. Watanabe, A. Matsuda, T. Terashima, and K. Kadowaki. Systematics of electronic structure and interactions in $\text{Bi}_2\text{Sr}_2\text{Ca}_{n-1}\text{Cu}_n\text{O}_{2n+4}$ ($n = 1 - 3$) by angle-resolved photoemission spectroscopy. *Phys. Rev. B*, 67(6):060501, 2003.

- [161] W. Zhang, G. Liu, L. Zhao, H. Liu, J. Meng, X. Dong, W. Lu, J.S. Wen, Z.J. Xu, G.D. Gu, T. Sasagawa, G. Wang, Y. Zhu, H. Zhang, Y. Zhou, X. Wang, Z. Zhao, C. Chen, Z. Xu, and X.J. Zhou. Identification of a New Form of Electron Coupling in the $\text{Bi}_2\text{Sr}_2\text{CaCu}_2\text{O}_8$ Superconductor by Laser-Based Angle-Resolved Photoemission Spectroscopy. *Phys. Rev. Lett.*, 100(10):107002, 2008.
- [162] A.W. Sandvik, D.J. Scalapino, and N.E. Bickers. Effect of an electron-phonon interaction on the one-electron spectral weight of a d-wave superconductor. *Phys. Rev. B*, 69(9):094523, 2004.
- [163] M.R. Norman and H. Ding. Collective modes and the superconducting-state spectral function of $\text{Bi}_2\text{Sr}_2\text{CaCu}_2\text{O}_8$. *Phys. Rev. B*, 57(18):R11089–R11092, 1998.
- [164] T. Valla, T.E. Kidd, W.-G. Yin, G.D. Gu, P.D. Johnson, Z.H. Pan, and A.V. Fedorov. High-Energy Kink Observed in the Electron Dispersion of High-Temperature Cuprate Superconductors. *Phys. Rev. Lett.*, 98(16):167003, 2007.
- [165] J. Graf, G.-H. Gweon, K. McElroy, S. Y. Zhou, C. Jozwiak, E. Rotenberg, A. Bill, T. Sasagawa, H. Eisaki, S. Uchida, H. Takagi, D.-H. Lee, and A. Lanzara. Universal High Energy Anomaly in the Angle-Resolved Photoemission Spectra of High Temperature Superconductors: Possible Evidence of Spinon and Holon Branches. *Phys. Rev. Lett.*, 98(6):067004, 2007.
- [166] B. P. Xie, K. Yang, D. W. Shen, J. F. Zhao, H. W. Ou, J. Wei, S. Y. Gu, M. Arita, S. Qiao, H. Namatame, M. Taniguchi, N. Kaneko, H. Eisaki, K. D. Tsuei, C. M. Cheng, I. Vobornik, J. Fujii, G. Rossi, Z. Q. Yang, and D. L. Feng. High-Energy Scale Revival and Giant Kink in the Dispersion of a Cuprate Superconductor. *Phys. Rev. Lett.*, 98(14):147001, 2007.
- [167] J. Chang, S. Pailh  s, M. Shi, M. M  nsson, T. Claesson, O. Tjernberg, J. Voigt, V. Perez, L. Patthey, N. Momono, M. Oda, M. Ido, A. Schnyder, C. Mudry, and J. Mesot. When low- and high-energy electronic responses meet in cuprate superconductors. *Phys. Rev. B*, 75(22):224508, 2007.
- [168] D.S. Inosov, J. Fink, A.A. Kordyuk, S.V. Borisenko, V.B. Zabolotnyy, R. Schuster, M. Knupfer, B. B  chner, R. Follath, H.A. D  rr, W. Eberhardt, V. Hinkov, B. Keimer, and H. Berger. Momentum and Energy Dependence of the Anomalous High-Energy Dispersion in the Electronic Structure of High Temperature Superconductors. *Phys. Rev. Lett.*, 99(23):237002, 2007.
- [169] A.A. Kordyuk, S.V. Borisenko, A. Koitzsch, J. Fink, M. Knupfer, and H. Berger. Bare electron dispersion from experiment: Self-consistent self-energy analysis of photoemission data. *Phys. Rev. B*, 71(21):214513, 2005.

- [170] X. J. Zhou, Junren Shi, T. Yoshida, T. Cuk, W. L. Yang, V. Brouet, J. Nakamura, N. Man-
nella, Seiki Komiya, Yoichi Ando, F. Zhou, W. X. Ti, J. W. Xiong, Z. X. Zhao, T. Sasagawa,
T. Kakeshita, H. Eisaki, S. Uchida, A. Fujimori, Zhenyu Zhang, E. W. Plummer, R. B.
Laughlin, Z. Hussain, and Z.-X. Shen. Multiple Bosonic Mode Coupling in the Electron
Self-Energy of $\text{La}_{2-x}\text{Sr}_x\text{CuO}_4$. *Phys. Rev. Lett.*, 95(11):117001, 2005.
- [171] R. J. McQueeney, J. L. Sarrao, P. G. Pagliuso, P. W. Stephens, and R. Osborn. Mixed
Lattice and Electronic States in High-Temperature Superconductors. *Phys. Rev. Lett.*,
87(7):077001, 2001.
- [172] H. He, Y. Sidis, P. Bourges, G. D. Gu, A. Ivanov, N. Koshizuka, B. Liang, C. T. Lin, L. P.
Regnault, E. Schoenher, and B. Keimer. Resonant Spin Excitation in an Overdoped
High Temperature Superconductor. *Phys. Rev. Lett.*, 86(8):1610–1613, Feb 2001.
- [173] W. Meevasana, N. J. C. Ingle, D. H. Lu, J. R. Shi, F. Baumberger, K. M. Shen, W. S.
Lee, T. Cuk, H. Eisaki, T. P. Devereaux, N. Nagaosa, J. Zaanen, and Z.-X. Shen. Doping
Dependence of the Coupling of Electrons to Bosonic Modes in the Single-Layer High-
Temperature $\text{Bi}_2\text{Sr}_2\text{CuO}_6$ Superconductor. *Phys. Rev. Lett.*, 96(15):157003, 2006.
- [174] T. Cuk, F. Baumberger, D. H. Lu, N. Ingle, X. J. Zhou, H. Eisaki, N. Kaneko, Z. Hussain,
T. P. Devereaux, N. Nagaosa, and Z.-X. Shen. Coupling of the B_{1g} Phonon to the Antin-
odal Electronic States of $\text{Bi}_2\text{Sr}_2\text{Ca}_{0.92}\text{Y}_{0.08}\text{Cu}_2\text{O}_{8+\delta}$. *Phys. Rev. Lett.*, 93(11):117003,
2004.
- [175] J.P. Locquet, J. Perret, J. Fompeyrine, E. Machler, J.W. Seo, and G Van Tendeloo.
Doubling the critical temperature of $\text{La}_{1.9}\text{Sr}_{0.1}\text{CuO}_4$ using epitaxial strain. *Nature*,
394(6692):453–456, 1998.
- [176] A. Mans, I. Santoso, Y. Huang, W. K. Siu, S. Tavaddod, V. Arpiainen, M. Lindroos,
H. Berger, V. N. Strocov, M. Shi, L. Patthey, and M. S. Golden. Experimental Proof of a
Structural Origin for the Shadow Fermi Surface of $\text{Bi}_2\text{Sr}_2\text{CaCu}_2\text{O}_{8+\delta}$. *Phys. Rev. Lett.*,
96(10):107007, 2006.
- [177] S.H. Pan, E.W. Hudson, J. Ma, and J.C. Davis. Imaging and identification of atomic
planes of cleaved $\text{Bi}_2\text{Sr}_2\text{CaCu}_2\text{O}_{8+\delta}$ by high resolution scanning tunneling microscopy.
Applied Physics Letters, 73(1):58, 1998.
- [178] G. Ghiringhelli. RIXS of soft x-rays: Resolving the crystal field excitations in strongly
correlated systems. *Soft-X-Ray Photon-In and Photon-Out Spectroscopy: New Frontiers*,
ALS, Berkeley, 2005.
- [179] A. Kotani and S. Shin. Resonant inelastic x-ray scattering spectra for electrons in solids.
Rev. Mod. Phys., 73(1):203–246, Feb 2001.

- [180] A Kotani. Resonant inelastic X-ray scattering in d and f electron systems. *Eur. Phys. J. B*, 47(1):3–27, 2005.
- [181] L.J.P. Ament, G. Ghiringhelli, M.M. Sala, L. Braicovich, and J. van den Brink. Theoretical Demonstration of How the Dispersion of Magnetic Excitations in Cuprate Compounds can be Determined Using Resonant Inelastic X-Ray Scattering. *Phys. Rev. Lett.*, 103(11):117003, 2009.
- [182] L. Braicovich, J. van den Brink, V. Bisogni, M. Moretti Sala, L.J.P. Ament, N.B. Brookes, G.M. De Luca, M. Salluzzo, T. Schmitt, V.N. Strocov, and G. Ghiringhelli. Magnetic Excitations and Phase Separation in the Underdoped $La_{2-x}Sr_xCuO_4$ Superconductor Measured by Resonant Inelastic X-Ray Scattering. *Phys. Rev. Lett.*, 104(7):077002, 2010.
- [183] L. Braicovich, L.J.P. Ament, V. Bisogni, F. Forte, C. Aruta, G. Balestrino, N.B. Brookes, G.M. De Luca, P.G. Medaglia, F. Miletto Granozio, M. Radovic, M. Salluzzo, J. van den Brink, and G. Ghiringhelli. Dispersion of Magnetic Excitations in the Cuprate La_2CuO_4 and $CaCuO_2$ Compounds Measured Using Resonant X-Ray Scattering. *Phys. Rev. Lett.*, 102(16):167401, 2009.
- [184] G. Ghiringhelli, A. Piazzalunga, C. Dallera, T. Schmitt, V. N. Strocov, J. Schlappa, L. Patthey, X. Wang, H. Berger, and M. Grioni. Observation of Two Nondispersive Magnetic Excitations in NiO by Resonant Inelastic Soft-X-Ray Scattering. *Phys. Rev. Lett.*, 102(2):027401, 2009.
- [185] J. Zaanen, G.A. Sawatzky, and J.W. Allen. Band gaps and electronic structure of transition-metal compounds. *Phys. Rev. Lett.*, 55(4):418–421, 1985.
- [186] M.Z. Hasan, E.D. Isaacs, Z.X. Shen, L.L. Miller, K. Tsutsui, T. Tohyama, and S. Maekawa. Electronic structure of mott insulators studied by inelastic X-ray scattering. *Science*, 288(5472):1811, 2000.
- [187] M.Z. Hasan, P.A. Montano, E.D. Isaacs, Z.X. Shen, H. Eisaki, S.K. Sinha, Z. Islam, N. Motoyama, and S. Uchida. Momentum-Resolved Charge Excitations in a Prototype One-Dimensional Mott Insulator. *Phys. Rev. Lett.*, 88(17):177403, 2002.
- [188] F.M.F. de Groot, P. Kuiper, and G.A. Sawatzky. Local spin-flip spectral distribution obtained by resonant x-ray Raman scattering. *Phys. Rev. B*, 57(23):14584–14587, 1998.
- [189] G. Ghiringhelli, A. Piazzalunga, X. Wang, A. Bendounan, H. Berger, F. Bottegoni, N. Christensen, C. Dallera, M. Grioni, J.C. Grivel, M. Moretti Sala, L. Patthey, J. Schlappa, T. Schmitt, V. Strocov, and L. Braicovich. Crystal field and low energy excitations measured by high resolution RIXS at the L_3 edge of Cu, Ni and Mn. *European Physical Journal-Special Topics*, 169:199–205, 2009.

- [190] M. Guarise, B. Dalla Piazza, M.M. Sala, G. Ghiringhelli, L. Braicovich, H. Berger, J.N. Hancock, D. van der Marel, T. Schmitt, V.N. Strocov, L.J.P. Ament, J. van den Brink, P.H. Lin, P. Xu, H.M. Rønnow, and M. Grioni. High-energy magnon dispersion demonstrate extended interactions in the undoped cuprates. *Arxiv preprint arXiv:1004.2441*, 2010.
- [191] J.D. Perkins, R.J. Birgeneau, J.M. Graybeal, M.A. Kastner, and D.S. Kleinberg. Midinfrared optical excitations in undoped lamellar copper oxides. *Phys. Rev. B*, 58(14):9390–9401, 1998.
- [192] J. Lorenzana and G.A. Sawatzky. Phonon Assisted Multimagnon Optical Absorption and Long Lived Two-Magnon States in Undoped Lamellar Copper Oxides. *Phys. Rev. Lett.*, 74(10):1867–1870, 1995.
- [193] R. Coldea, S.M. Hayden, G. Aeppli, T.G. Perring, C.D. Frost, T.E. Mason, S.W. Cheong, and Z. Fisk. Spin Waves and Electronic Interactions in La_2CuO_4 . *Phys. Rev. Lett.*, 86(23):5377–5380, 2001.
- [194] M. Greven, R.J. Birgeneau, Y. Endoh, M.A. Kastner, M. Matsuda, and G. Shirane. Neutron-scattering study of the 2-dimensional spin $S=1/2$ square-lattice Heisenberg-antiferromagnet $\text{Sr}_2\text{CuO}_2\text{Cl}_2$. *Zeitschrift für Physik B-Condensed Matter*, 96(4):465–477, 1995.
- [195] P. Kuiper, J.H. Guo, C. Sâthe, L.C. Duda, J. Nordgren, J.J.M. Poethuizen, F.M.F. de Groot, and G.A. Sawatzky. Resonant X-Ray Raman Spectra of Cu dd Excitations in $\text{Sr}_2\text{CuO}_2\text{Cl}_2$. *Phys. Rev. Lett.*, 80(23):5204–5207, 1998.
- [196] G. Ghiringhelli, N.B. Brookes, E. Annese, H. Berger, C. Dallera, M. Grioni, L. Perfetti, A. Tagliaferri, and L. Braicovich. Low Energy Electronic Excitations in the Layered Cuprates Studied by Copper L_3 Resonant Inelastic X-Ray Scattering. *Phys. Rev. Lett.*, 92(11):117406, 2004.
- [197] Y. Harada, K. Okada, R. Eguchi, A. Kotani, H. Takagi, T. Takeuchi, and S. Shin. Unique identification of Zhang-Rice singlet excitation in $\text{Sr}_2\text{CuO}_2\text{Cl}_2$ mediated by the O $1s$ core hole: Symmetry-selective resonant soft x-ray Raman scattering study. *Phys. Rev. B*, 66(16):165104, 2002.

Curriculum Vitae

Peng Xu

Personal details:

- Date of birth: June 25, 1979
 - Place of birth: Yancheng, China
 - Nationality: China
 - Marital status: Married
-

Education:

- 1999-2003 Bachelor, Physics, Nanjing University of Information Science and Technology, Nanjing, China
 - 2003-2006 Master, Optics, Fudan University, Shanghai, China
 - since 2006 PhD candidate, Condensed matter physics, Ecole Polytechnique Fédérale de Lausanne (EPFL), Switzerland
-

Languages:

- English: fluent written and oral
- French: Basic
- Chinese: mother tongue

Software:

- Expert in Igor, Matlab, Materials studio, Mathematica, MS office, solidworks, Origin
-

Awards:

- A class in Challenging Cup-Tang creative competition, 2005
 - 3rd award in "Jiangsu undergraduates technique and innovation competition" (2002)
 - First-class and second-class awards during undergraduate period (1999-2003)
-

Schools:

- August 2007, Zuoz (Switzerland), 6th PSI Summer School on Condensed Matter Research
-

Conferences:

- Manep meeting, Les Diablerets (Switzerland), Sept. 26-28, 2007 (Photoemission investigation on triple-layered BISCCO superconductor)
- The Swiss Physical Society Annual Meeting (Geneva), Mar. 26-27, 2008 (Angle resolved photoemission investigation on La-doped Bi-2201 thin films)
- Manep meeting, Les Diablerets (Switzerland), Aug. 26-28, 2009 (Superconductivity through disorder in quasi-two-dimensional 1T-TaS₂)

Conference talks:

- **Superconducting phase in the layered dichalcogenide 1T-TaS₂ upon inhibition of the metal insulator transition** The Swiss Physical Society Annual Meeting (Basel), Jun. 21-22, 2010

Teaching:

- Physique Général I: Prof. M. Grioni
 - Physique Général II: Prof. M. Grioni
-

Publications:

- **Superconducting phase in the layered dichalcogenide 1T-TaS₂ upon inhibition of the metal insulator transition**
P. Xu, J. O. Piatek, P.-H. Lin, B. Sipos, H. Berger, L. Forró, H. M. Rønnow, and M. Grioni, Phys. Rev. B 81, 172503 (2010)
 - **Semimetal to semiconductor phase transition in 1T-TiS₂ induced by Nb doping studied by angle resolved photoemission spectroscopy**
Peng Xu, Pin-hui Lin, Miguel A. Valbuena, Balazs Sipos, Helmuth Berger, László Forró and Marco Grioni, to be submitted to Phys. Rev. B
 - **Coexistence of superconductivity and charge-density-wave in 2H-Sn_xTaS₂**
Peng Xu, Miguel A. Valbuena, Pin-hui Lin, Stevan Arsenijevic, Helmuth Berger, László Forró, and Marco Grioni, to be submitted to Phys. Rev. B
 - **Quasi-particle properties on Bi-2223: kink, gaps, and multi-layers splitting**
A. Bendounan, P. Xu, M. Shi, Y. Sassa, E. Van Heumen, L. Patthey, A. Piriou, E. Giannini, D. van der Marel, M. Grioni, J. Mesot, in preparation for Phys. Rev. B
 - **High-energy magnon dispersion demonstrate extended interactions in undoped cuprates**
M. Guarise, H. M. Ronow, M. Moretti Sala, G. Ghiringhelli, L. Braicovich, B. Dalla Piazza, H. Berger, J.N. Hancock, D. van der Marel, T. Schmitt, V. Strocov, P.-H. Lin, P. Xu, and M. Grioni, submitted to Phys. Rev. Lett. (arXiv:1004.2441v2)
-

Not related to the PhD thesis:

- **Experimental study on the bandgap narrowings of TiO₂ films calcined under N₂ or NH₃ atmosphere**
Mi L, Xu P, Wang PN, Applied Surface Science 255 (2008), 2574-2580

- **Recovery of visible-light photocatalytic efficiency of N-doped TiO₂ nanoparticulate films**
Mi L, **Xu P**, Shen H, Wang PN, Journal of Photochemistry and Photobiology A: Chemistry 193, (2008) 222-227
- **Visible-light photocatalysis of nitrogen-doped TiO₂ nanoparticulate films prepared by low-energy ion implantation**
Hong Shen, Lan Mi, **Peng Xu**, Weidian Shen and Pei-Nan Wang, Applied Surface Science Volume 253, (2007) 7024-7028 (Times Cited: 10)
- **First-principles calculation of N:H codoping effect on energy gap narrowing of TiO₂**
Lan Mi, **Peng Xu**, Hong Shen, and Pei-Nan Wang Weidian Shen, Appl. Phys. Lett. 90, 171909 (2007) (Times Cited: 10)
- **Improved optical response for N-doped anatase TiO₂ films prepared by pulsed laser deposition in N₂/NH₃/O₂ mixture**
Peng Xu, Lan Mi and Pei-Nan Wang, Journal of Crystal Growth 289, 2006, 433-439 (Times Cited: 21)
- **Temperature determination of N₂ discharge plasma by computational simulation of its emission spectra**
Mi L, **Xu P**, Wang PN, Journal of Physics of D-Applied Physics 38 3885-3888 (2005)